

Time-of-Flight Mass Spectrometry to Characterize Inorganic Coordination Complexes and Cyanobacteria

Stephen Warren Hunsucker

Dissertation submitted to the Faculty of the Virginia Polytechnic Institute and State University in partial fulfillment of the requirements for the degree of

Doctor of Philosophy
in
Chemistry

Brian M. Tissue, Chair
Mark R. Anderson
Paul A. Deck
William A. Ducker
Larry T. Taylor

April 20, 2001
Blacksburg, Virginia

Keywords: MALDI, scytonemin, polymetallic complexes, water stress protein, peptide mass fingerprint

Copyright 2001, Stephen Warren Hunsucker

Time-of-Flight Mass Spectrometry to Characterize Inorganic Coordination Complexes and Cyanobacteria

Stephen W. Hunsucker

(ABSTRACT)

Matrix assisted laser desorption/ionization time-of flight mass spectrometry (MALDI-TOFMS) is used to study several inorganic coordination complexes and a variety of compounds from cyanobacteria. Also presented is a discussion of TOFMS instrumentation and the improvements in resolution and instrument automation that have lead to widespread and diverse applications of MALDI-TOFMS in all areas of science.

The feasibility of using direct laser desorption/ionization (LDI) TOFMS to detect trace elements in a variety of glass samples using a lithium borate fusion technique for sample preparation is investigated. The result of the fusion technique is a homogeneous incorporation of the analytical sample into a glass. The fusion technique is investigated as a way to eliminate matrix effects in direct LDI-TOFMS analysis. However, the high concentration and low ionization potential of lithium suppress ionization of the elements of interest. The detection limits of elements in glass samples were not at the trace level. Therefore the technique is not as useful as well-established analytical methods like X-ray fluorescence and inductively coupled plasma mass spectrometry.

Direct laser ablation and matrix-assisted laser desorption/ionization time-of-flight mass spectrometric analysis of four inorganic coordination complexes are discussed. The compounds studied include $[\text{Ir}(\text{dpp})_2\text{Cl}_2](\text{PF}_6)$, $\{[(\text{bpy})_2\text{Ru}(\text{dpp})]_2\text{RuCl}_2\}(\text{PF}_6)_4$, $[(\text{tpy})\text{Ru}(\text{tpp})\text{Ru}(\text{tpp})\text{RhCl}_3](\text{PF}_6)_4$ and $\{[(\text{bpy})_2\text{Ru}(\text{dpp})]_2\text{IrCl}_2\}(\text{PF}_6)_5$ (dpp = 2,3-*bis*-(2'-pyridyl)-pyrazine, bpy = 2,2'-bipyridine, tpy = 2,2',6',2"-terpyradine, tpp = 2,3,5,6,-*tetrakis*-(2'-pyridyl)-pyrazine). Spectral intensities and fragmentation patterns are compared and evaluated for several instrument parameters, matrices, and matrix-to-analyte ratios. Direct ablation and MALDI mass spectra of the monometallic complex

showed the same ion peaks and differed only in the relative peak intensities. Direct ablation of the trimetallic complexes produced only low-mass fragments containing one metal atom at most. MALDI spectra of the trimetallic complexes exhibited little fragmentation in the high-mass region (>1500 Da) and less fragmentation in the low-mass region compared to direct laser ablation. Proper matrix selection for MALDI analysis was vital, as was an appropriate matrix-to-analyte ratio. The results demonstrate the applicability of MALDI-TOF mass spectrometry for the structural characterization of labile inorganic coordination complexes. A correlation is made between the gas-phase redox chemistry in the MALDI plume and the solution phase electrochemistry for this series of complexes.

MALDI-TOFMS was also used to study compounds isolated from cyanobacteria. A MALDI screening method has been developed to detect the presence of scytonemin, a UV-absorbing pigment. Detection of scytonemin is accomplished by a simple solvent extraction of cyanobacteria in the desiccated state with subsequent MALDI-TOFMS analysis. The method is rapid and semi-quantitative. Cyanobacteria is the only known organism to produce scytonemin, and it is only produced when the organism is subjected to UV stress. Laboratory-grown cultures were subjected to different amounts of UV radiation, and the screening method was used to detect the presence or absence of scytonemin. Cultures grown under ambient conditions (low UV) did not show the presence of scytonemin, while those grown under UV lamps did show the detectable scytonemin. Because scytonemin acts as a biomarker for UV stress, the MALDI screening method could find application in molecular ecology studies of cyanobacteria.

Peptide mass fingerprinting is used to monitor the isolation of the water stress protein from *N. commune*. The protein is produced by recombinant growth in *E. coli* in order to assess the role of Wsp in the desiccation tolerance of *N. commune*. The results show that SDS-PAGE and Western blot analysis are not sufficient to detect the presence of Wsp after purification using ion-exchange chromatography. Three *E. coli* proteins were identified in the same molecular weight range as Wsp and one of them cross-reacts with the series of antibodies used for the Western blot. The presence of contaminating proteins that cross-react with the immuno assay make it difficult to determine which fractions contained Wsp. Peptide mass fingerprints were obtained for a

series of fractions collected after ion-exchange chromatography to pinpoint the location of Wsp. Peptide mass fingerprinting was also used to monitor the stability of the clone and results show that the clone is modified over a six month period.

Acknowledgements

First and foremost I would like to thank my wife Julie Hunsucker for her gracious support and encouragement throughout my graduate studies. I would also like to thank my parents, Phil and Beverly Hunsucker, for all of the love and support they gave and continue to give me. I couldn't have achieved this without them. My siblings, Cindy, Todd, and Jenny have always been there for support and encouragement when I needed it most.

I would like to thank Dr. Brian Tissue for his guidance, support, and encouragement. The members of my committee deserve thanks for helpful discussions and useful advice as well as their assistance with this manuscript. Dr. Rich Helm and Dr. Malcolm Potts have given me the opportunity to broaden my horizons and I have learned so much from them. I would like to give a special thanks to Dr. Ray Dessy for all of the great conversations we've had, his support and encouragement, and all of the things he did for me that he didn't have to. Dr. Ron Estler, my invaluable undergraduate advisor, deserves thanks for his continued support and encouragement and for teaching me his love of science. I would not be the scientist or the person I am without all of these people.

Table of Contents

Abstract	ii
Acknowledgements	v
Table of Contents	vi
List of Figures	ix
List of Tables	xiv
List of Equations	xv
List of Abbreviations	xvi
Chapter 1 – Introduction	1
1.1 Principles of TOFMS.....	1
1.1.1 <i>Basic Instrumentation and Separation Mechanism</i>	1
1.1.2 <i>Advantages and Disadvantages</i>	7
1.1.3 <i>Fundamental Limitations on Resolution</i>	8
1.1.4 <i>Improving Resolution in Linear TOFMS</i>	11
1.1.5 <i>Using a Reflectron to Increase Resolution in TOFMS</i>	13
1.1.6 <i>Mass Calibration in TOFMS</i>	16
1.2 MALDI-TOFMS Instrumentation	17
1.3 TOFMS Instruments Used in This Research.....	19
1.3.1 <i>Comstock LI/RTOF 210</i>	19
1.4 MALDI-TOFMS	24
1.4.1 <i>Experimental Parameters in MALDI</i>	26
1.4.2 <i>Ionization Mechanism in MALDI</i>	29
Chapter 2 – LDI-TOFMS of Borate Glass Samples	35
2.1 Introduction	35
2.2 Lithium Borate Fusion Technique.....	35
2.2.1 <i>Advantages and Disadvantages</i>	35
2.2.2 <i>Fluxes and Additives</i>	37
2.3 Experimental Details.....	38
2.3.1 <i>Materials</i>	38

2.3.2 Glass Preparation.....	38
2.3.3 Flame Atomic Absorption Spectroscopy	39
2.3.4 LDI-TOFMS	40
2.4 Results and Discussion	42
2.4.1 Flame Atomic Absorption Spectroscopy	42
2.4.2 LDI-TOFMS of Glass Samples.....	42
2.5 Conclusions	51
Chapter 3 – Characterization of Inorganic Coordination Complexes by LDI- and MALDI-TOFMS.....	53
3.1 Introduction	53
3.2 Experimental Details	54
3.2.1 Chemicals.....	54
3.2.2 Sample Preparation.....	55
3.2.3 Mass Spectrometric Analysis	56
3.3 Results and Discussion	58
3.3.1 Acceleration Potential and Resolution	58
3.3.2 Direct Laser Desorption/Ionization	61
3.3.3 MALDI-TOFMS.....	64
3.3.4 Matrix Selection.....	68
3.3.5 Matrix-to-Analyte Ratio.....	70
3.4 Conclusions	71
Chapter 4 – Using MALDI-TOFMS to Study Cyanobacteria.....	74
4.1 Introduction	74
4.1.1 Background Information on Cyanobacteria.....	74
4.1.2 Using Mass Spectrometry to Study Organisms	77
4.2 Experimental Details.....	80
4.2.1 Scytonemin Screening	80
4.2.2 Protein Analysis.....	81
4.3 Results and Discussion	82
4.3.1 Scytonemin Screening	82
4.3.2 Whole Protein Analysis	90
4.3.3 Peptide Mass Fingerprinting.....	92
4.4 Conclusions	104
4.4.1 Scytonemin Screening	104
4.4.2 Protein Analysis and Peptide Mass Fingerprinting.....	105
4.4.3 Future Experiments	106

Chapter 5 – Summary	108
Appendix A – Soil Digestion Protocol	110
Appendix B – In-gel Digestion Protocol for MALDI-TOFMS Analysis of an SDS-PAGE Gel Separated, Coomassie-Stained Protein.....	111
References.....	115
Vita.....	122

List of Figures

Figure 1.1 Schematic of a linear time-of-flight mass spectrometer. Components are described in the text.	2
Figure 1.2 Illustrations of voltage pulsing schemes in the ion source. (a) Schematic of a dual-stage ion source. (b) Single-stage ion source with continuous ion extraction, and delayed extraction (c). (e-f) Various voltage pulsing schemes for a dual-stage ion source using delayed extraction.....	3
Figure 1.3 Schematic showing sample position within the ion source. (a) The most common sample position for MALDI experiments is in the axial position. The laser comes in at a shallow angle (typically 30 degrees from repeller plate) and plume expansion is in the direction of the flight tube. (b) Some instruments incorporate an orthogonal geometry where the laser hits the sample at ninety degrees and plume expansion is perpendicular to the flight axis.....	4
Figure 1.4 Schematic representation of ion focusing for (a) two ions formed at different times, (b) two ions formed in different positions, (c) two ions with different initial kinetic energies, and (d) ions with opposite velocity vectors. All ions have the same m/z ratio. The arrows represent direction of motion and the magnitude of kinetic energy for the ion.	11
Figure 1.5 Schematic representation of a reflectron. Isomass ions with lower initial kinetic energy ($U-U_0$) have a shorter path length through the reflectron. Ions with higher initial kinetic energy ($U+U_0$) have longer a longer path length, but catch up to other ions at the detector due to their higher velocity. The electric fields U_F and U_R vary linearly over the distances shown.....	14
Figure 1.6 Illustration of mass calibration in time-of-flight mass spectrometry. The calibration equation is used to transform a TOF spectrum into a mass spectrum. An example is given in the table, where known mass is compared to calibrated mass.	16
Figure 1.7 Optical setup when using the PTI 3300 nitrogen laser for desorption/ionization. All lens' are quartz, all mirrors are Al coated borosilicate glass. The laser beam is focused onto to the sample in the axial position. Pulse energy measurements are taken after the focusing lens.....	22
Figure 1.8 Sequence of timing events in a TOFMS experiment. The sync out signal from the laser is sent 1.0 μ s prior to the laser firing. After the appropriate delay, the DD/PG triggers the repeller plate power supply as the laser hits the surface. The repeller plate is then pulsed after a user-selected delay time.....	22
Figure 1.9 Schematic representation of the MALDI process. A small volume of solid is sublimed due to the laser pulse. The gas phase plume contains neutrals, ions and clusters of the matrix as well as analyte ions.	25
Figure 1.10 Images of DHB sample spot showing the difference in crystal size before (a) and after (b) recrystallization. The sample in (a) was redissolved in methanol and evaporated under a stream of nitrogen to produce the sample seen in (b). The spots are about 3 mm in diameter.....	27
Figure 2.1 Schematic showing how the glass beads are mounted to the sample probe and the position of the sample relative to the ion source and flight tube.	41

Figure 2.2 LDI-TOFMS of a glass bead that contains 9.2% (w/w) zinc oxide. The three major isotopes of zinc are clearly seen as well as a peak that is believed to be $^{64}\text{Zn}_2$ at 128 Da. Both spectra were recorded under identical instrument conditions..... 44

Figure 2.3 Mass spectra of a blank glass bead made using a 2:1 mixture of LiBO_2 and $\text{Li}_2\text{B}_4\text{O}_7$. The spectra were collected using a repeller delay of 17 μs (top) and 35 μs (bottom). All other instrument conditions were identical. This illustrates how longer delay times can be used to eliminate low mass matrix ion signals. 44

Figure 2.4 Mass spectrum resulting from LDI-TOFMS analysis of a pure zinc oxide pellet. The insets show the calculated isotope pattern of the Zn and Zn_2 series of ions. The respective oxides have similar isotopic distributions to the metal ion series. 45

Figure 2.5 LDI-TOFMS results from analysis of a glass bead doped with 7.1% (w/w) yttrium oxide. The low intensity of the matrix peaks is due to the low laser energy necessary to obtain the Y^+ and YO^+ signals..... 46

Figure 2.6 LDI-TOFMS results from analysis of a glass bead doped with 2.6% (w/w) yttrium oxide. The low intensity of the matrix peaks is due to the low laser energy necessary to obtain the Y^+ and YO^+ signals..... 46

Figure 2.7 LDI-TOFMS results from analysis of a glass bead doped with 300 ppm yttrium oxide. The high intensity of the matrix peaks is due to the high laser energy necessary to obtain the Y^+ and YO^+ signals. The inset shows the relatively weak analyte ion signals. This concentration is near the detection limit..... 47

Figure 2.8 LDI-TOFMS of a glass bead containing 16% (w/w) Virginia soil. The spectrum shows the presence of new peaks in the 70-95 Da range as well as the large increase in signal intensity for Na and K (23 and 39/41 Da, respectively). The upper inset is an expansion of the 70-95 Da region. See text for peak assignments. 48

Figure 2.9 LDI-TOFMS analysis of the glass bead containing 20% (w/w) SRM 2709. The upper spectrum shows the drastic increase in Na and K as well as the appearance of Mg and Al. The lower spectrum is very similar to the spectrum obtained for the Virginia soil. See text for peak assignments..... 50

Figure 3.1 2-dimensional representation of the chemical structure of the inorganic coordination complexes investigated..... 55

Figure 3.2 Schematic showing aluminum probe extension. The sample is typically held 7 mm below the flight axis. 57

Figure 3.3 MALDI mass spectra of $[\text{Ir}(\text{dpp})_2\text{Cl}_2]^+$ on two different instruments. The pseudomolecular ion is seen in both cases (731), along with peaks that show the loss of each Cl (696, 661). The top spectrum was collected using the Comstock LI/RTOF 210 with an acceleration potential of -2.3 kV. The bottom spectrum was collected on the Kratos Kompact SEQ with an acceleration potential of 24 kV. 59

Figure 3.4 Comparison of mass spectra of $\{[(\text{bpy})_2\text{Ru}(\text{dpp})]_2\text{RuCl}_2\}(\text{PF}_6)_4$ using different acceleration potentials. The top spectrum is the result of direct LDI on the Kratos Kompact SEQ with a 24 kV acceleration potential. The bottom spectra is the result of MALDI on the Comstock LI/RTOF 210 with an acceleration potential of -2.3 kV. The lower acceleration potential decreases the resolution to the extent that the MALDI spectrum is very similar to the direct LDI spectrum, and no high mass peaks are observed. 60

Figure 3.5 Direct laser desorption/ionization mass spectra of the inorganic coordination complexes. Spectra were recorded on the Kratos Kompact SEQ with a 24 kV acceleration potential. Note that no high mass peaks are observed.	62
Figure 3.6 Comparison of isotope patterns for the peak at $m/z = 525$ in the direct LDI mass spectrum of $[(\text{tpy})\text{Ru}(\text{tpp})\text{Ru}(\text{tpp})\text{RhCl}_3]^{4+}$. The top spectrum is a theoretical isotope pattern for the fragment ion $(\text{tpp})\text{RhCl}^+$, the middle spectrum is a theoretical isotope pattern for the fragment ion $(\text{tpp})\text{RuCl}^+$, and the bottom spectrum is the experimentally observed isotope distribution. This strategy is used to help identify fragment ions.	63
Figure 3.7 MALDI-TOF mass spectra of trimetallic complexes using the Kratos Kompact SEQ with an acceleration potential of 24 kV. Each complex shows a series of $[\text{M}-n(\text{PF}_6)]^+$ ions as well as some monometallic fragments in the lower mass region. The matrix compound used to collect these spectra sinapinic acid with a matrix-to-analyte ratio of about 500:1.	65
Figure 3.8 Molecular structures of the organic matrix compounds used to study the inorganic coordination complexes. The matrices that produce the $[\text{M}-n(\text{PF}_6)]^+$ ions are sinapinic acid, α -cyano-4-hydroxycinnamic acid, 2,5-dihydroxybenzoic acid, and 6-aza-2-thiothymine.....	69
Figure 3.9 MALDI mass spectra of $\{[(\text{bpy})_2\text{Ru}(\text{dpp})]_2\text{IrCl}_2\}(\text{PF}_6)_5$ in 2,5-dihydroxybenzoic acid acquired on the Kratos Kompact SEQ with an acceleration potential of 24 kV. The top and bottom spectra have matrix-to-analyte ratios of 5000:1 and 200:1, respectively. The higher matrix-to-analyte ratio results in matrix adducts and does not produce the ion series $[\text{M}-n(\text{PF}_6)]^+$	69
Figure 3.10 MALDI-TOF mass spectrum of $\{[(\text{bpy})_2\text{Ru}(\text{dpp})]_2\text{IrCl}_2\}(\text{PF}_6)_5$ in sinapinic acid collected on the Kratos Kompact SEQ with an acceleration potential of 24 kV. The top and bottom spectra have matrix-to-analyte ratios of 5000:1 and 200:1, respectively. The major difference is seen in the low mass region where the monometallic fragment ions are seen.....	70
Figure 3.11 Bridging ligands used to study the effect of conjugation on the spectroscopic properties of polymetallic inorganic coordination complexes. The complexes become easier to reduce as the aromatic system is extended. (See Bridgewater, et al.).....	72
Figure 4.1 Chemical structure of the UV-photoprotective pigment scytonemin in the oxidized and reduced forms.	77
Figure 4.2 Schematic illustration of the steps involved in peptide mass fingerprinting.	79
Figure 4.3 MALDI mass spectrum of a solvent extract of dried <i>N. commune</i> CHEN. DHB was used as the matrix. Comparison with the blank and analysis of pure scytonemin (inset) clearly indicates the presence of the reduced form of scytonemin. The sodium and potassium adducts (570 and 586 Da, respectively) are also seen.....	83
Figure 4.4 PSD mass spectrum of scytonemin. The peaks at 519.7 and 491.6 Da are most likely due to consecutive loss of carbonyl groups. The peak at 273.8 represents the monomer subunit. The region between 250 and 440 Da has been expanded ten-fold in intensity.	84
Figure 4.5 MALDI mass spectra of <i>N. punctiforme</i> cultures grown under different lighting conditions. The sample grown under UV-light shows the presence of scytonemin. The peak at 871.9 Da is pheophytin a, a derivative of chlorophyll a. Peaks	

at 569.3 and 894.2 are sodium adducts of scytonemin and pheophytin a, respectively, while the peak at 910.2 is the potassium adduct of pheophytin a. 85

Figure 4.6 PSD spectrum of pheophytin a. The two main fragments, shown by arrows, are a result of the loss of the phytol side chain and subsequent loss of HOOCCH₃. The region around the peak at 533.9 Da was expanded by a factor of 10. 86

Figure 4.7 MALDI mass Spectra showing the biosynthesis of scytonemin when the culture is grown under UV light. All peaks except 546.5, 871.8, and 894.5 Da are matrix peaks..... 87

Figure 4.8 MALDI mass spectra of *Chroococcidiopsis* grown under high and low UV light. This species is not expected to produce scytonemin because it is endolithic..... 88

Figure 4.9 MALDI mass spectra resulting from the extraction of two cyanobacterial mats. The predominant organism in each mat is indicated. Peaks at 546.8, 569.8, and 584.9 Da represent scytonemin and the sodium and potassium adducts of scytonemin, respectively. 89

Figure 4.10 MALDI TOF mass spectra of Wsp using α -cyano-4-hydroxycinnamic acid (A) and sinapinic acid (B). Each matrix leads to a different series of charge states. 91

Figure 4.11 Peptide mass fingerprint of BSA using sinapinic acid (A) and α -cyano-4-hydroxycinnamic acid (B) as the matrix. Asterisks indicate peaks due to peptides resulting from the autolysis of trypsin. Labeled peaks show peptides of BSA..... 94

Figure 4.12 Top two images show SDS-PAGE gels of 14 fractions collected from ion-exchange chromatography of the supernatant. The first lane of each gel contains molecular weight markers and the last lane in the upper right hand image shows the supernatant. The lower images are Western blots of the two gels showing immunoresponse for proteins believed to be Wsp. 96

Figure 4.13 Peptide mass fingerprint of OmpF resulting in 54% of the amino acid sequence detected. The peak markers and the mass list represent peptides belonging to OmpF. 97

Figure 4.14 Gel images showing fractions from two different ion-exchange separations using TRIS as the buffer. Three *E. coli* proteins were identified in the same molecular weight range as Wsp. The fractions are numbered in order of elution. 98

Figure 4.15 Peptide mass fingerprint of GAPDH-A representing 44% amino acid coverage. The peak markers and mass list pertain to GAPDH-A peptides. 99

Figure 4.16 Peptide mass fingerprint of CSASE-A representing 19% amino acid coverage. The peak markers and mass list pertain to CSASE-A peptides. Trypsin peptide peaks were used for internal calibration. 99

Figure 4.17 Peptide mass fingerprint of Wsp representing 26% amino acid coverage. The mass values were searched against *E. coli* proteins and no results were returned. The peak markers and mass list pertain to Wsp peptides. 100

Figure 4.18 Peptide mass fingerprints of the supernatant from an *E. coli* culture (control) and an *E. coli* culture encoded to produce Wsp (Wsp clone). Peak markers show the presence of OmpF (control) and Wsp (Wsp clone). 101

Figure 4.19 SDS-PAGE gel image of aliquots of the supernatant collected at the times indicated (in hours). Glucose (G) was added to one of the cultures after 24 hours and seems to facilitate protein production. OmpF excretion increases with time. 102

Figure 4.20 Peptide mass fingerprints from gel bands of material collected at 6 (A), 19 (B), and 24 (C) hours. Peak markers in spectrum B indicate OmpF (O) and Wsp (W)

peptides. The production of OmpF increases with time as seen by the relative increase in peak intensity for OmpF peptides. 103

Figure 4.21 Peptide mass fingerprint of supernatant right after clone was developed. Peak markers show peptides from Wsp. The inset is an expansion of the 760 to 860 Da mass range. 104

Figure 4.22 Reaction scheme to determine the activity of glycosyl transferases..... 107

List of Tables

Table 1.1 DD/PG settings	21
Table 1.2 Common contaminants in MALDI and the approximate tolerance limit.....	28
Table 2.1 List of samples and fluxes used to generate a homogeneous glass.....	37
Table 2.2 Instrument conditions and standards prepared for flame atomic absorption spectroscopy of the Virginia soil.....	40
Table 2.3 A list of elements and their certified concentration in the NIST soil sample (SRM 2709).....	50
Table 2.4 A list of the ionization potential for the elements considered in this study.....	52
Table 3.1 Laser desorption/ionization threshold energies for all of the matrices studied.....	58
Table 3.2 High mass fragments observed by MALDI-TOFMS.....	67
Table 3.3 Oxidation and reduction potentials for the inorganic coordination complexes investigated.....	67
Table 4.1 Illustration of the mass accuracy resulting from various calibration methods.....	92
Table 4.2 Observed peptide masses for BSA using the factory calibration and the associated mass accuracy. Corrected masses were obtained by adding the average mass difference to the factory calibrated mass value. The mass accuracy is improved by a factor of 4.	95

List of Equations

Equation 1.1 - Ion kinetic energy	5
Equation 1.2 - Flight time of an ion.....	5
Equation 1.3 - Ion velocity through the drift region	6
Equation 1.4 - Resolution in TOFMS.....	8
Equation 1.5 - Total ion kinetic energy	9
Equation 1.6 - Total ion velocity	9
Equation 1.7 - Ion velocity in the acceleration region	9
Equation 1.8 - Residence time of an ion in the acceleration region.....	9
Equation 1.9 - Residence time of an ion in the acceleration region.....	9
Equation 1.10 - Residence time of an ion in the drift region	9
Equation 1.11 - Total flight time of an ion.....	10
Equation 1.12 - Resolution and kinetic energy	13

List of Abbreviations

ACA	9-anthracenecarboxylic acid
ATT	6-aza-2-thiothymine
BSA	Bovine Serum Albumin
CSASE-A	cysteine synthase A
Da	Dalton, unit of mass
DD/PG	Digital Delay/Pulse Generator
DHB	2,5-dihydroxybenzoic acid
DHC	3,4-dihydroxycinnamic acid
DNBA	3,5-dinitrobenzoic acid
EPS	Extracellular Polysaccharide Sheath
ESI	Electrospray Ionization
FAAS	Flame Atomic Absorption Spectroscopy
FAB	Fast Atom Bombardment
FWHM	Full-Width at Half-Maximum Height
GAPDH-A	glyceraldehyde-3-phosphate dehydrogenase A
HCCA	α -cyano-4-hydroxycinnamic acid
HPLC	High Pressure Liquid Chromatography
ICP-MS	Inductively Couple Plasma Mass Spectrometry
LDI	Laser Desorption/Ionization
MAA	Mycosporine Amino Acid
MALDI	Matrix Assisted Laser Desorption/Ionization
mDNB	meta-dinitrobenzene
m/z	Mass-to-Charge Ratio
Nd:YAG	Neodymium: Yttrium Aluminum Garnet
NMR	Nuclear Magnetic Resonance
OmpF	outer membrane protein F
PSD	Post-Source Decay
Ru-Ir-Ru	$\{[(bpy)_2Ru(dpp)]_2IrCl_2\}(PF_6)_5$
Ru-Rh	$[(tpy)Ru(tpp)RhCl_3](PF_6)_2$

Ru-Ru-Rh	$[(\text{tpy})\text{Ru}(\text{tpp})\text{Ru}(\text{tpp})\text{RhCl}_3](\text{PF}_6)_4$
Ru-Ru-Ru	$\{[(\text{bpy})_2\text{Ru}(\text{dpp})]_2\text{RuCl}_2\}(\text{PF}_6)_4$
SA	sinapinic acid
S/N	signal-to-noise ratio
TOFMS	Time-of-Flight Mass Spectrometry
UV/Vis	Ultraviolet/Visible
Wsp	Water Stress Protein
XRF	X-ray Fluorescence

Chapter 1 – Introduction

Mass spectrometry has become a vital tool for research in all areas of science, including geology, physics, materials, chemistry, biochemistry, and medicine. With the development of "soft" ionization techniques such as electrospray and matrix-assisted laser desorption/ionization (MALDI), it is now possible to mass analyze non-volatile, thermally labile, biological molecules such as proteins and peptides. Time-of-flight mass spectrometry (TOFMS) is particularly attractive for analysis of large molecules because it has a broad mass range.

This chapter will discuss instrumental aspects of TOFMS, MALDI ionization mechanisms and applications, and give a general experimental approach. Successive chapters will discuss the three projects that make up the dissertation research. Each chapter will introduce background topics relevant to that project, describe specific experimental details, and discuss the experimental results. The goal of the research was to test the utility of TOFMS for the analysis of different classes of compounds and its applicability to analytical problem solving.

1.1 Principles of TOFMS

1.1.1 Basic Instrumentation and Separation Mechanism

TOFMS is a pulsed technique because of the need for an initial time reference (time zero) for each recorded mass spectrum. Therefore, ions are typically introduced to the mass spectrometer in well-timed pulses. For this reason the most common ionization source for TOFMS instruments is a pulsed laser, such as a nitrogen or Nd:YAG laser. Continuous ion streams must be pulsed by gating before being introduced to the TOFMS, which complicates the experiment.

A schematic of a linear TOFMS is given in Figure 1.1. The spectrometer consists of three basic regions: The ion source (also known as the extraction/acceleration region), the flight tube (also known as the field-free, or drift region), and the detector. The ion source is the region where ions are either introduced to the spectrometer or created. Typical ionization methods for TOFMS include electron bombardment, electrospray, direct laser desorption/ionization (LDI), and MALDI. The first two methods

generally introduce ions or molecules into the source region, and the laser-based methods generate ions inside the source. As mentioned above, LDI is the most common ionization mechanism used with TOFMS because of the pulsed-mode operation. LDI also has advantages related to mass resolution that are discussed in Section 1.1.3.

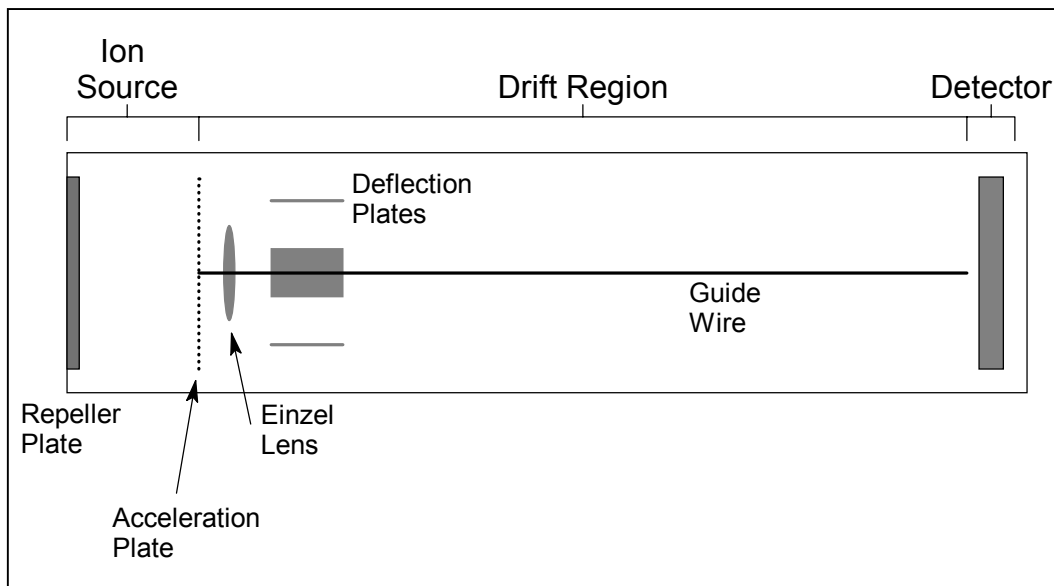


Figure 1.1 Schematic of a linear time-of-flight mass spectrometer. Components are described in the text.

The ion source consists of a series of planar electrodes that accelerate ions towards the detector. There are two basic designs for the ion source: Single-stage and dual-stage. A single-stage ion source has two electrodes where the first electrode is commonly referred to as the repeller plate and the second as the acceleration plate. A dual-stage ion source is a three-electrode arrangement. In this case the first stage is the extraction region and the second stage is the acceleration region. The extraction (center electrode) and acceleration plates have wire mesh in the center that allow for high ion transmission (typically ~90%) while still maintaining a consistent electric field.

Figure 1.2 shows a schematic of a dual-stage ion source and illustrates several ways that positive ions are accelerated out of the ion source towards the flight tube for both single- and dual-stage sources. Negative-ion acceleration is achieved by reversing the polarities of the applied voltages. Also shown are the concepts of continuous (Figure 1.2b) and delayed extraction (Figure 1.2c-f). None of the applied voltages are pulsed

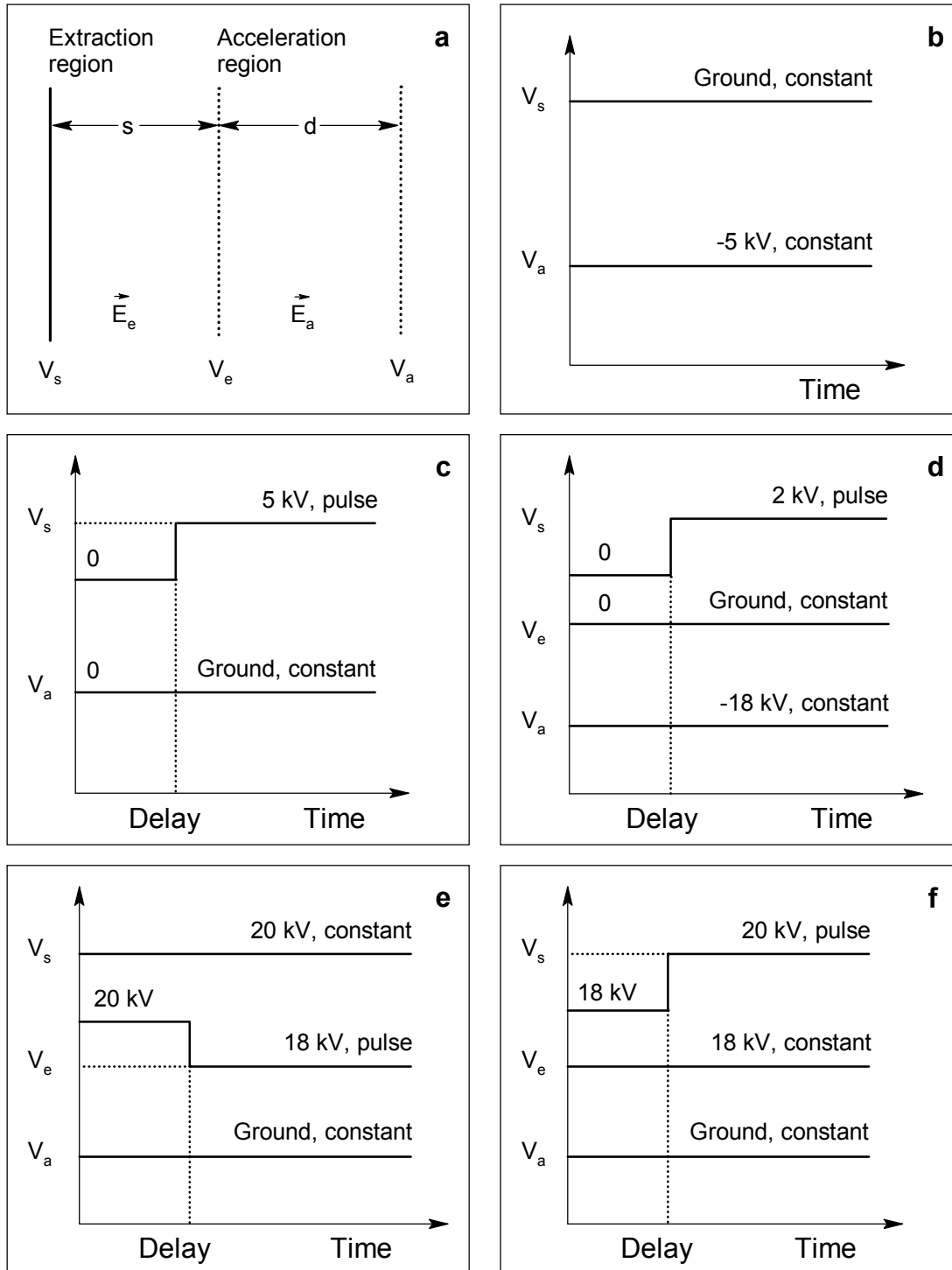


Figure 1.2 Illustrations of voltage pulsing schemes in the ion source. (a) Schematic of a dual-stage ion source. (b) Single-stage ion source with continuous ion extraction, and delayed extraction (c). (e-f) Various voltage pulsing schemes for a dual-stage ion source using delayed extraction.

during continuous extraction. Delayed extraction (or time-lag focusing) was first introduced by Wiley and McLaren in 1955 as a way to improve mass resolution.¹ This method introduces a small time delay prior to ion acceleration. The pulsing voltage can be applied to either the repeller plate (Figure 1.2c,d,f) or the extraction plate (Figure 1.2e). Further discussion of the logic behind dual-stage, pulsed ion extraction appears in Section 1.1.4. The duration of the time delay depends on the geometry of the ion source. Figure 1.3 shows axial and orthogonal sample positions, which are the two possible geometries in the ion source. Typical delay times for an instrument in which the sample is in the plane of the repeller plate (Figure 1.3a), and ion expansion is in the direction of the flight tube, are on the order of hundreds of nanoseconds. Delay times for an instrument where the sample probe is between the repeller plate and the extraction plate (Figure 1.3b), with ion expansion perpendicular to the flight tube, can range from several to tens of microseconds depending on the sample distance from the flight tube axis.

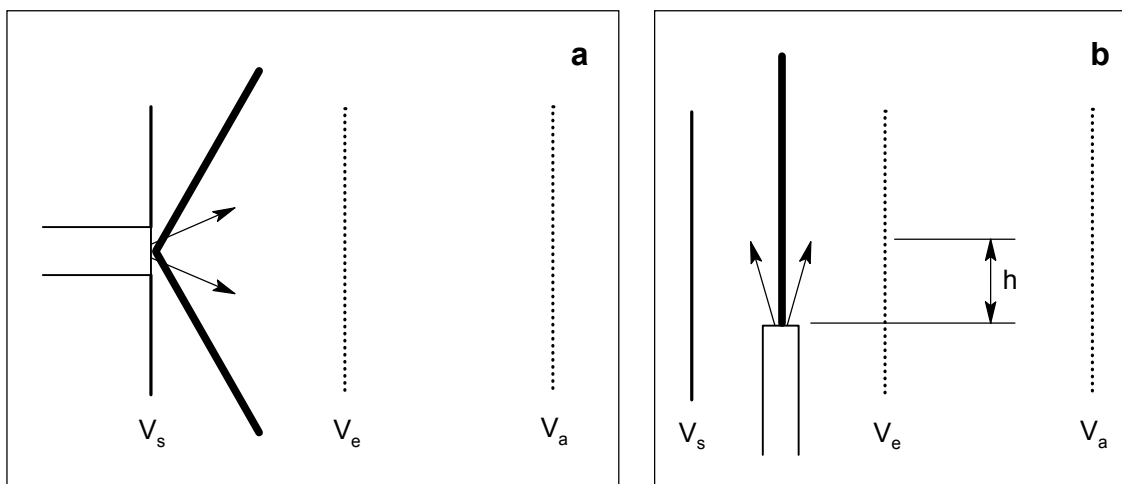


Figure 1.3 Schematic showing sample position within the ion source. (a) The most common sample position for MALDI experiments is in the axial position. The laser comes in at a shallow angle (typically 30 degrees from repeller plate) and plume expansion is in the direction of the flight tube. (b) Some instruments incorporate an orthogonal geometry where the laser hits the sample at ninety degrees and plume expansion is perpendicular to the flight axis.

The flight tube is the region where ions are directed toward the detector and, most importantly, where mass separation takes place. At the front of the flight tube is a set of ion optics that steer and collimate the ion beam. The x- and y-directions of the ion

beam are controlled by a set of deflection plates. These are four small (several square centimeters) metal plates, two for the x-direction and two for the y-direction, that have relatively small (<100 V) potentials applied to them. The potentials on each set of plates are adjusted until the maximum ion signal is detected, thus indicating the ion beam is centered on the surface of the detector. The ion beam is collimated in one of two ways. The first collimation device is known as an Einzel lens, which uses a low voltage elliptical field to control ion beam diffusion. However, similar to an optical lens used to collimate a beam of light, the Einzel lens shows divergence over finite distance (on the order of 1-2 meters). The other method uses a guide wire that runs the entire length of the flight tube.^{2,3} This setup consists of a thin tungsten wire (60 μm diameter) with a low voltage (30-100 V) applied to it. This captures the ions generated in the source and transfers them in a tight packet (5-mm radius after a 2-m flight tube) to the detector.⁴ Flight tubes longer than 2 meters require a guide wire, as the Einzel lens does not provide sufficient beam collimation at these lengths. Both of these methods significantly enhance sensitivity by focusing the majority of ions onto the detector surface.

The separation mechanism of TOFMS is very simple. After the ions are created and accelerated out of the ion source they enter the field-free flight tube. At the end of the acceleration region all ions, independent of their mass, have approximately the same kinetic energy (U), which is defined by Equation 1.1.

$$U = eEs \tag{eq 1.1}$$

Where E is the electric field (in V/cm), e is the charge of an electron (in C), and s is the initial position of the ion (in cm). Equation 1.2 gives the flight time (t) of an ion through the field-free region (D) which is proportional to the square root of its mass-to-charge ratio (m/z).

$$t = \left(\frac{m}{2U} \right)^{1/2} D \tag{eq 1.2}$$

Therefore, singly charged ions with a higher mass will have a lower velocity than lighter ions and consequently reach the detector at later times. The velocity of an ion when it reaches the field-free region is given by Equation 1.3.

$$v = \left(\frac{2U}{m} \right)^{1/2} = \left(\frac{2eEs}{m} \right)^{1/2} \quad (\text{eq 1.3})$$

A more detailed treatment of these principles is found in Section 1.1.3. Typically, flight tubes are 1.0 – 2.0 meters long, but have been made as long as 8 meters.² In general, a longer flight tube results in a larger separation of adjacent masses (higher mass resolution), but can result in loss of sensitivity due to insufficient ion-beam collimation.

The two types of detectors used in TOFMS are micro-channel plates (MCP) and electron multipliers (EM).⁵ Both detectors are capable of achieving gains in the range of 10^5 - 10^7 . This means it is possible to detect single ions, but background noise is often too great to observe the signal. The sensitivity of both detectors depends on the momentum, not the energy, of the impinging ion. For this reason, high mass ions (>5-10 kDa) are more difficult to detect because not every impinging ion ejects an electron from the detector surface. This is especially true when low acceleration potentials (<10 kV) are used in the ion source. Detection efficiency is one of the major limitations on the upper mass range of TOFMS. One way to increase detection efficiency in the high mass range is to incorporate an additional acceleration region, known as post acceleration, just prior to the detector to increase the momentum of the ions.

Both detectors have limitations. When using a MCP for MALDI it is essential not to saturate the detector with low mass matrix ions. If a significant number of the channels are saturated, sensitivity is lost for later-arriving ions (analytes) due to the slow recovery time (several milliseconds) after saturation.⁶ For this reason, some researchers have configured the voltages applied to the deflection plates to deflect low-mass ions away from the detector.³ Discrete-dynode electron multipliers do not suffer from the same saturation effects as MCP detectors. However, EMs can broaden peaks observed in TOFMS. This occurs due to a difference in travel time of electrons ejected from the surface of the detector. If two ions with the same m/z impinge on the detector at the same time, but one hits the center and one hits the edge, there will be a several nanosecond time spread introduced to the observed peak.⁵

1.1.2 Advantages and Disadvantages

TOF instruments are fundamentally different from other mass spectrometers because the detection of ions is temporal rather than spatial. Instruments that use electric and/or magnetic sectors or quadrupole filters for mass selection separate ions based on angular dispersion and therefore require a slit or aperture to select the ion of interest. Because of this, a “mass scan” is required in order to collect an entire mass spectrum. Similarly, ion-traps select the mass of interest by applying the correct voltage to cause the ion to be ejected from its orbit. Therefore, a mass scan is also required for ion-traps. Mass scans increase the time necessary to acquire a mass spectrum and slow down sequential analyses. One of the main advantages of TOFMS is that an entire mass spectrum is recorded on a microsecond time scale for each ionization event. This means that many spectra can be recorded in a very short time, and signal averaging can be used to increase the signal-to-noise ratio. For example, 100 mass spectra can be averaged in ten seconds with a 10-Hz laser. It typically takes four seconds or longer to scan the entire mass range of a quadrupole mass filter to record a single mass spectrum. Another advantage of collecting an entire mass spectrum for each ionization/acceleration event is the ability to accurately measure relative peak intensities even though ion source conditions might fluctuate from pulse-to-pulse. This makes the instrumentation simpler when compared to scanning mass spectrometers that must control, or correct for, instrumental fluctuations during acquisition of an entire mass spectrum.

TOFMS is inherently more sensitive than scanning mass analyzers, with the exception of ion-traps, because all of the ions produced during ionization are recorded for each mass spectrum. Ion throughput is also improved in a TOFMS because there are no slits in the ion source or in front of the detector. Both of these characteristics translate into higher ion transmission for each ionization event. Scanning mass spectrometers detect a small mass range of ions at a time. For example, a quadrupole mass spectrometer that is scanned from m/z 10-1010 collects data at any given m/z value for 0.1% of the scan time. This means that less than 0.1% of the ions created are actually detected during the scan. By comparison, much smaller amounts of material

are required for TOFMS analysis. Detection limits in MALDI-TOFMS are now reaching the attomole range.

Probably the most significant advantage that TOFMS has over other mass analyzers is the theoretically unlimited mass range for ion detection. Scanning instruments have fundamental limitations that are imposed by the ability of the electric, magnetic and rf fields to spatially separate ions. Ion-traps also have limitations on the total number of ions to be stored. For example, quadrupole mass spectrometers have an upper m/z limit of a few thousand due to practical limitations of rf generation. The fundamental separation mechanism in TOFMS does not impose a mass limitation. Although there are practical limitations on the upper mass limit, such as decreased resolution at high mass and detector sensitivity, ions as large as 1,500,000 Da have been detected with TOFMS.⁷

The main disadvantage of TOFMS is the poor mass resolution when compared with other types of mass analyzers. Significant advances have been made to increase resolution in TOFMS and resolution is beginning to approach that of quadrupole and ion-trap instruments. A TOFMS with a resolution of 10,000 is considered a high resolution instrument, but this is a routine resolution for scanning instruments. The next section gives a detailed discussion of the achievable resolution in TOFMS.

1.1.3 Fundamental Limitations on Resolution

TOFMS was first introduced in the 1940's but was soon replaced by magnetic and quadrupole instruments because of poor resolution (about 300). Also, electronics were not available to efficiently record and process a mass spectrum on the microsecond time scale. This required coalescence of multiple spectra in order to obtain an entire mass spectrum. The advancements outlined in the next few sections have resulted in the resurgence of TOFMS as an analytical tool.

Resolution in TOFMS is defined in terms of both mass and time by Equation 1.4.

$$R = \frac{m}{\Delta m} = \frac{t}{2\Delta t} \quad (\text{eq 1.4})$$

The Δm and Δt terms represent the full-width at half-maximum height (FWHM) of the observed peak. If all ions were formed in the same spot at the same time with no initial velocity, the resolution would be limited only by detection electronics. However, this is

not the case, and resolution in TOFMS is severely limited by the ions (with the same m/z) not being formed at the same time, in the same place and with the same kinetic energy prior to acceleration. These differences are commonly referred to as the initial time, space and energy distributions. The ability to minimize these distributions defines the maximum achievable resolution in TOFMS. Wiley and McLaren first studied the relative effect of each of these peak-broadening factors.¹ The following is a detailed derivation of the time-of-flight of an ion that reflects the origin of these limitations.

The velocity of an ion at any given time is given by Equation 1.3 and is related to the kinetic energy. The total kinetic energy of an ion is the sum of its initial kinetic energy and the energy received upon acceleration (eq 1.5).

$$U_T = U_0 + eEs \quad (\text{eq 1.5})$$

The velocity throughout the entire experiment is given by Equation 1.6.

$$v = (U_0 + eEs)^{1/2} \left(\frac{2}{m} \right)^{1/2} \quad (\text{eq 1.6})$$

In the acceleration region the velocity is not constant and changes according to its position (eq 1.7).

$$v = ds / dt \quad (\text{eq 1.7})$$

The time it takes an ion to reach the end of the acceleration region (dt) is found by solving a differential equation (eq 1.8).

$$\int_0^{t_s} dt = \left(\frac{m}{2} \right)^{1/2} \int_0^s \frac{ds}{(U_0 + eEs)^{1/2}} \quad (\text{eq 1.8})$$

The solution is given in Equation 1.9.

$$t_s = \left(\frac{2m}{eE} \right)^{1/2} [(U_0 + eEs)^{1/2} \pm U_0^{1/2}] + t_0 \quad (\text{eq 1.9})$$

The velocity in the field-free region (D) is constant and the time spent in this region is given by Equation 1.10

$$t_D = \frac{(2m)^{1/2} D}{2(U_0 + eEs)^{1/2}} \quad (\text{eq 1.10})$$

The total flight time is therefore found by Equation 1.11

$$t = t_s + t_D$$

$$t = \left(\frac{2m}{eE} \right)^{1/2} [(U_0 + eEs)^{1/2} \pm U_0^{1/2}] + \frac{(2m)^{1/2} D}{2(U_0 + eEs)^{1/2}} + t_0 \quad (\text{eq 1.11})$$

The total flight time depends on when the ion was formed (t_0), its position in the ion source upon acceleration (s) and its initial kinetic energy (U_0).

Figure 1.4 is a graphical representation of the effects of time, space and energy distributions on resolution. The arrows define the direction of motion and the magnitude of the kinetic energy. If two ions of the same m/z have the same initial kinetic energy and are formed at the same position in the ion source, the final peak width is determined by the initial time distribution of ion formation (Figure 1.4a). In this case the peak width is independent of the length of the field-free region. In other words, a longer field-free region will provide more separation between two peaks of differing m/z but will not affect peak width. Using a short pulse width laser to achieve ionization minimizes the initial time distribution. For this reason most ionization sources used in TOFMS are lasers with pulse widths of 5 ns or less. In this case the initial time distribution has a minimal effect on resolution.

Two ions that are formed at the same time, with the same kinetic energy but at different positions in the source region will have different kinetic energies following acceleration (Figure 1.4b). This difference is because the energy an ion receives during acceleration (eEs) due to an electric field depends on the position of the ion. Since electric field strength is measured in V/cm, an ion closer to the field-free region will be given less kinetic energy. In this case, longer flight tubes will provide better peak separation, but will result in broader peaks. At some point in the field-free region the ion with the higher kinetic energy will catch up with the ion that was initially closer to the flight tube. The point is known as the plane of space focus.

From the above derivation of the overall flight time (eq 1.11) it is evident that two ions with the same m/z , formed in the same position at the same time but with different initial kinetic energies, will arrive at the detector at different times (Figure 1.4c). However, the final situation under consideration is shown in Figure 1.4d, where two ions with the same m/z are formed at the same time, in the same position, with the same

initial kinetic energy, but with opposing velocity vectors. This circumstance is referred to as the “turn-around” time of an ion. At the end of the acceleration region both ions will have the same amount of kinetic energy, and therefore the same velocity, but the ion traveling away from the flight tube has to be stopped and turned around by the electric field. The turnaround time results in a temporal distribution of ions with the same m/z .

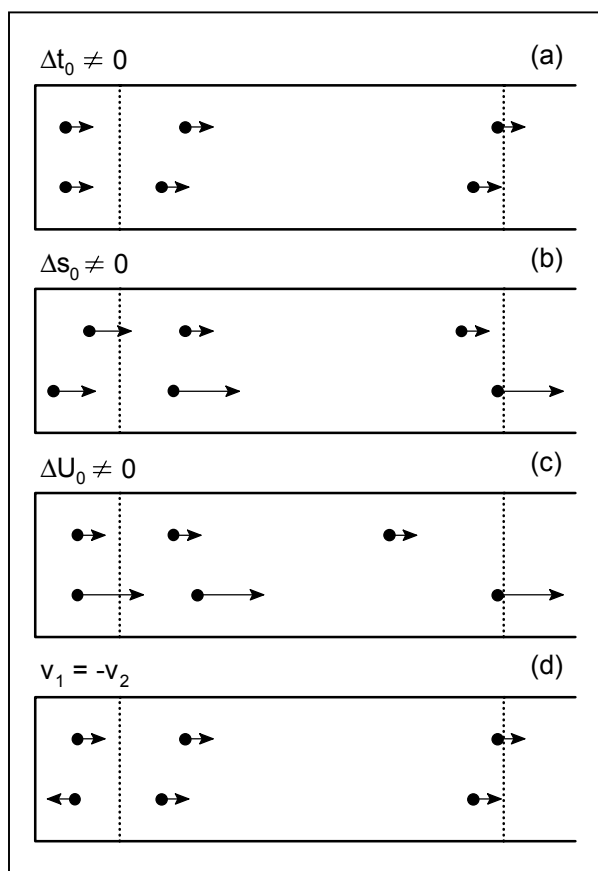


Figure 1.4 Schematic representation of ion focusing for (a) two ions formed at different times, (b) two ions formed in different positions, (c) two ions with different initial kinetic energies, and (d) ions with opposite velocity vectors. All ions have the same m/z ratio. The arrows represent direction of motion and the magnitude of kinetic energy for the ion.

1.1.4 Improving Resolution in Linear TOFMS

Resolution improvements in TOFMS came in several steps. In the 1950's when Wiley and McLaren were investigating ways of improving mass resolution, ions were created in the gas-phase by electron bombardment. This method of ion generation leads to a relatively large initial space distribution as well as the initial energy and

temporal distributions. In 1955 Wiley and McLaren introduced the dual-stage ion source as a means to improve resolution.¹ The new source design, combined with delayed extraction, allowed for corrections of the initial space and energy distributions simultaneously.

Space focus is achieved at the point in the field-free region where the ion with higher kinetic energy catches up with the ion that was initially closer to the flight tube. Using a single-stage ion source it can be shown that the plane of space focus depends on the geometry of the instrument and occurs at a distance equal to twice the length of the acceleration region. This condition forces the space focus plane to be well before the detector in instruments with standard flight tube lengths. However, as Wiley and McLaren showed, using a dual-stage ion source introduces two new parameters to be considered for the overall flight time of an ion; the length of the second stage (d), and the ratio of the acceleration fields (E_a/E_e). These two parameters allow for adjustment of the plane of space focus to the plane of the detector. The length of the extraction region (s) and the acceleration region (d) are fixed. The space focus is then empirically optimized by systematically adjusting the ratio E_a/E_e and observing where the maximum resolution is obtained. Typically, E_e is ten to fifteen percent of E_a .

Energy focusing was achieved by introducing a time delay between ion formation and ion extraction. The increase in resolution resulting from delayed extraction is best explained by considering the situation depicted in Figure 1.4d. If a time delay is introduced the ions will move to a new position in the source. The ion that is closer to the extraction plate will receive more kinetic energy due to its position in the electric field. This has the effect of reducing the peak broadening introduced by the turn-around time. However, delayed extraction during this time period had several limitations. First, the resolution improvement introduced by delayed extraction is mass dependent. This result means the delay must be optimized for ions with differing mass to achieve maximum resolution. Second, energy focusing and space focusing had opposing requirements on several system parameters (mainly, d and E_a/E_e). Therefore, optimal resolution was obtained by adjusting these parameters to reach a compromise between space and energy focusing. Although Wiley and McLaren did improve resolution in TOFMS, resolution was still not comparable to that obtained with scanning instruments.

Mass resolution in TOFMS would be an easier problem to address if the mass focusing were reduced to a single distribution. The advent of a laser as an ionization source has helped dramatically in this aspect. Since samples can be contained on a reasonably well-defined solid surface at the back of the ion source (Figure 1.3a) the problem of initial spatial distribution and turn-around time are immediately eliminated (under continuous extraction conditions). Also, because lasers are available with short pulse widths (<5 ns) the temporal distribution is minimized. For this reason, TOFMS was revitalized in the 1970's, and 80's and resolution was increased even further. Furthermore, since the spatial distribution was eliminated, the majority of instruments during this time period returned to single-stage, continuous extraction ion sources.

Using a laser for desorption/ionization, the distribution in initial kinetic energy becomes the largest resolution-limiting factor in continuous extraction TOFMS. Whereas the spatial and temporal distributions are minimized using laser desorption/ionization, the kinetic energy distribution becomes more difficult to control. The energy from the laser is not evenly distributed to all species during desorption/ionization. In fact LDI results in an initial kinetic energy distribution on the order of 50 eV. However, using higher acceleration fields and reflectrons can minimize the effect of the initial kinetic energy distribution. Using the equations for the flight-time and resolution of an ion, a relationship between resolution and kinetic energy can be derived (eq 1.12)

$$R = \frac{m}{\Delta m} \cong \frac{U}{U_0} \quad (\text{eq 1.12})$$

Equation 1.12 implies that an increase in the acceleration potential will minimize the effect of the initial kinetic energy distribution.^{8,9} For this reason most instruments apply voltages of 10 – 20 kV in the ion source region.

1.1.5 Using a Reflectron to Increase Resolution in TOFMS

The main development during the 1970's and 80's for increasing resolution was the discovery of the reflectron by Mamyrin and co-workers.^{10,11} A schematic representation of the reflectron is seen in Figure 1.5. Reflectrons consist of a series of grids that provide a linear electric field and allow for high ion transmission. The electric field retards the ions and ultimately reflects them backward at some small angle.

Focusing is achieved due to differential penetration of ions with the same m/z . Ions with an initial kinetic energy which is higher than average will penetrate the reflectron further, and ions with an initial kinetic energy less than average will not penetrate as far. The higher energy ions, which now lag behind, will then catch up to the slower moving ions at the detector surface. The small difference in flight path introduced by the reflectron provides a re-focusing of isomass ions at the detector. This type of energy focusing is independent of the mass of an ion, so it is not necessary to adjust the fields to acquire an entire mass spectrum. Dramatic improvements were made regarding resolution in TOFMS using a laser, a reflectron, and high potentials in the source region. The Wiley and McLaren instrument reported a resolution of 300, whereas the new instruments are achieving resolution as high as 35,000.¹² Due to the increase in resolution, TOFMS was revitalized as an analytical technique and began to compete with scanning mass spectrometers.

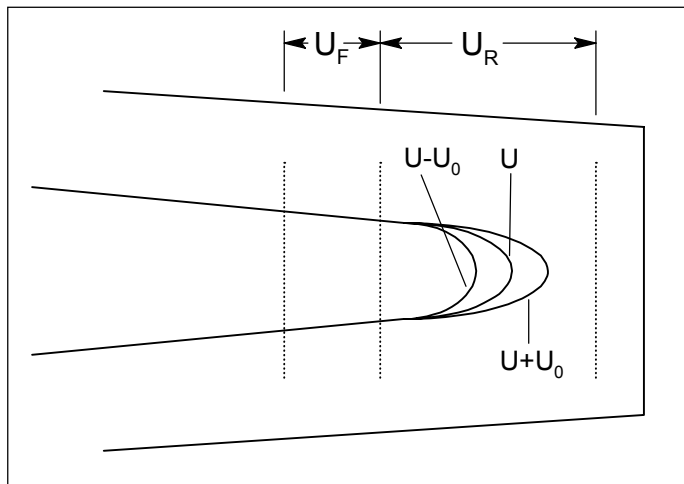


Figure 1.5 Schematic representation of a reflectron. Isomass ions with lower initial kinetic energy ($U-U_0$) have a shorter path length through the reflectron. Ions with higher initial kinetic energy ($U+U_0$) have longer a longer path length, but catch up to other ions at the detector due to their higher velocity. The electric fields U_F and U_R vary linearly over the distances shown.

The disadvantage of the reflectron is a loss in sensitivity. Because the reflectron incorporates a series of grids, there is a decrease in the overall ion transmission. Another factor resulting in lower sensitivity is the loss of secondary, or metastable, ions. As ions travel through the flight tube they are susceptible to fragmentation. Fragment ions formed in the drift region retain essentially the same velocity as the parent ion. In

linear TOFMS the fragments reach the detector at the same time as the parent ions. However, the reduced mass of the fragment ion means that the kinetic energy is lower than that of the parent ion. Fragmentation results in a range of kinetic energies for fragment ions with dissimilar mass. Also, due to the reduction in kinetic energy they barely penetrate the reflectron, which results in a much shorter path length than the parent ion causing them to arrive at the detector at a different time. Product ions with less than ninety percent of the parent mass are seen as broad peaks at short flight times because they are not focused by the reflectron. These two factors result in lower signal intensities and therefore decreased sensitivity when collecting parent ion mass spectra.

The reflectron does however offer a possibility that cannot be achieved with a linear TOFMS. This is known as post-source decay analysis (PSD).^{13,14} This technique allows for the detection of metastable fragment ions produced in the flight tube. There are two ways to perform PSD analysis. The first is rather cumbersome, but does result in reliable analyses. The electric field in a linear reflectron is systematically varied to produce a series of spectra.¹⁵ This variation is necessary because only a small mass range (several hundred Da) of the metastable ions are focused by the reflectron for a given field. For this reason, part of the product ion spectrum appears well resolved while other regions contain broad peaks. In order to resolve the lower mass peaks the potentials applied to the reflector have to be decreased in steps until sufficient resolution of all peaks is obtained. Decreasing the field allows the product ions with lower kinetic energy to penetrate the reflectron. The entire product ion spectrum is then obtained by combining the well-resolved sections of several spectra. This combination makes mass calibration of the entire spectrum more difficult and requires iterative mathematical procedures. The second method does not require scanning the reflectron voltages and stitching spectra together. This system is known as a curved-field (or parabolic) reflectron.^{16,17} The electric field in this device does not vary linearly, but has a field that resembles the arc of a circle. This configuration allows the metastable ions, with a range of kinetic energies, to penetrate the reflectron farther. The result is that all of the metastable ions, as well as the parent ion, can be focused onto the detector

without scanning. Therefore, the multiplex advantage of TOFMS is conserved with this design.

In the PSD experiment a precursor ion is selected by gating electronics that allow a small mass range to pass into the flight tube. PSD allows generation of tandem mass spectrometric data on a TOFMS. PSD has found use in sequencing peptides and proteins by mass spectrometry.

1.1.6 Mass Calibration in TOFMS

Mass calibration is required, as the actual data collected in a TOFMS experiment is the flight time of an ion. Calibration requires that several ions with known masses be detected. These standards can then be used to generate a calibration plot that is then used to transform a TOF spectrum into a mass spectrum. Figure 1.6 shows a typical calibration plot.

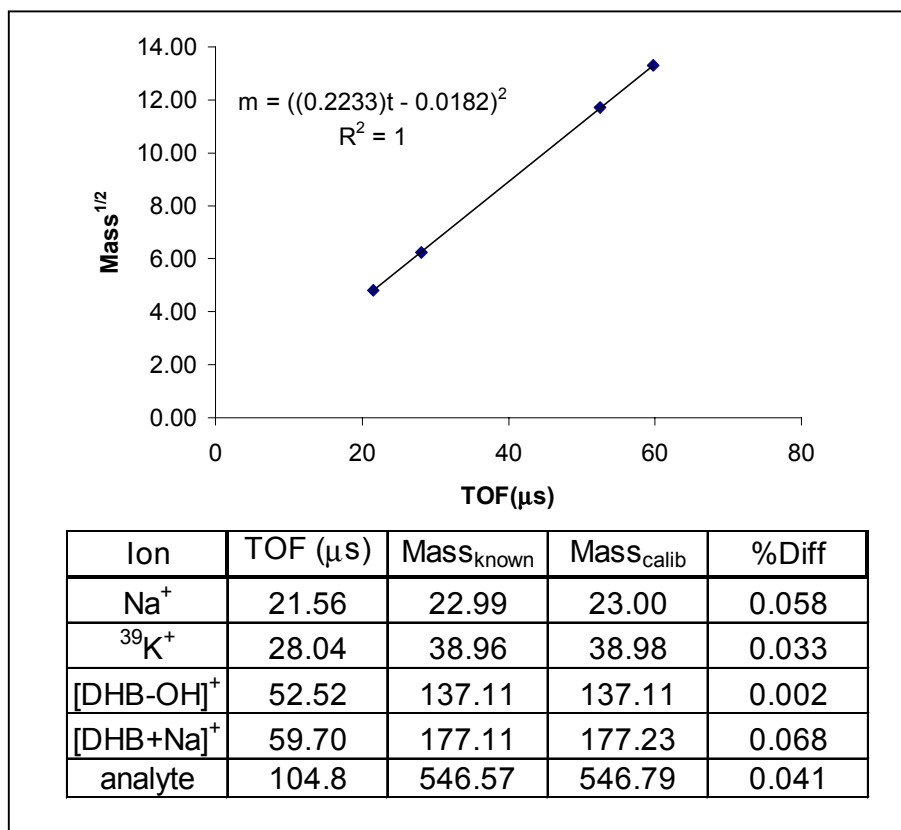


Figure 1.6 Illustration of mass calibration in time-of-flight mass spectrometry. The calibration equation is used to transform a TOF spectrum into a mass spectrum. An example is given in the table, where known mass is compared to calibrated mass.

As with any calibration procedure, there are two types of calibration; internal and external. An external calibration is determined a single time for each instrument. By analyzing a known sample with as broad a mass range as possible. A calibration equation is generated and used to generate mass spectra of all unknown samples. Mass accuracy using external calibration is typically on the order of 0.1% (i.e. ± 1 Da at a m/z ratio of 1000).

Internal calibration provides improved mass accuracy. Internal calibration is achieved by plotting flight time versus the square root of mass for known ions within each mass spectrum collected. In MALDI this is done in several ways. Several of the matrix peaks can be used as internal calibrants. However this provides reliable calibration in the low mass region only. As higher mass analytes are detected the mass accuracy decreases. One should add an internal standard that has a higher mass than the analyte (or at least comparable) in addition to the use of a matrix peak. The analyte mass is then bracketed by the calibration. MALDI analysis of peptides with internal calibration and mass resolution of 10,000 is typically in the range of 0.001% (i.e. ± 1 Da at a m/z ratio of 100,000).¹⁸ This high degree of mass accuracy becomes important when trying to identify proteins by peptide mass fingerprints and database searching, as will be discussed in Chapter 4.

1.2 MALDI-TOFMS Instrumentation

Modern TOFMS instruments used in MALDI typically incorporate dual-stage ion sources with axial geometry and high source potentials (> 20 kV) with the capability to operate in either the linear or reflectron mode. The nitrogen laser is by far the most common source for desorption/ionization. Due to the dense, gas-phase plume generated in MALDI experiments and the use of laser ionization sources with axial geometry there has also been a resurgence of delayed extraction.^{9,19} There is an important difference between the way ions are created with laser sources (from the solid phase) and the creation of ions in the gas-phase (electron bombardment). Wiley and McLaren observed that the initial space and velocity distributions were independent from one another and placed different requirements on instrumental conditions used to obtain maximum resolution. In this case, delayed extraction may or may not increase

the overall resolution. However, during laser desorption from the rear surface of the ion source (Figure 1.3a) the initial velocity and spatial distributions have a strong dependence on one another. This dependence allows higher resolution to be obtained since these distributions do not place opposing requirements on instrument conditions.

Colby, et al.¹⁹ published an elegant manuscript that included computer simulations of both continuous and delayed extraction of several proteins. Their simulation results predicted that the flight-time distribution (the observed peak width) for insulin ($[M+H]^+ = 5734$ Da) under continuous extraction would be 550 ns. The same simulation using delayed extraction predicted a flight-time distribution of 6 ns. Impressively, the simulation allowed for an initial velocity distribution ranging from 0 to 1200 m/s. Simulation results were confirmed by experimental data. The observed peak widths under continuous and delayed extraction were 300 ns and 12 ns, respectively. This corresponds to a 25-fold increase in resolution. The explanation for the increase in resolution is best understood by considering the relationship between an ion's initial velocity and the position in the source at the time of acceleration. After desorption from the surface, all ions are travelling towards the flight tube. During the delay time, ions with higher initial velocity will travel further from the repeller plate and therefore, upon extraction obtain a slightly lower velocity due to their position in the extraction region. The delay compensates for the initial velocity distribution of ions and results in a dramatic increase in resolution.

The other advantage of using delayed extraction in MALDI experiments has to do with the density of the gas-phase plume created during desorption/ionization. The pressure when the laser beam strikes the surface has been measured at greater than 30 Mtorr.²⁰ The pressure of neutral molecules 6 ms after the laser pulse and 3 mm above the surface was measured at 75 mtorr.²¹ This is compared to the typical vacuum pressure of 0.1 to 1 μ torr. Under continuous extraction conditions analyte ions experience many high-energy collisions in the dense plume during desorption and extraction. This results in a broader velocity distribution of analyte ions than would normally be observed, and therefore decrease the resolution. Delayed extraction allows analyte ions to expand away from the surface (to a region of lower pressure) which leads to a narrower distribution in initial velocity due to fewer high energy collisions with

matrix specie. The delay time also allows the analyte ions to undergo fewer collisions during acceleration due to expansion into a region of lower pressure. The combination of space-velocity correction and expansion into regions of lower pressure explain the dramatic increase in resolution observed using delayed extraction in MALDI experiments.

All of the above advancements in TOFMS instrumentation have led to the availability of commercial instruments that can obtain mass resolution in the range of 10,000. These instruments are also designed for high throughput analysis. Current MALDI probes provide multiple-well plates which allow for preparation of up to 384 different samples on a single plate. Appropriate data collection and handling systems (sample stage manipulation, acquisition software, automatic data storage, etc.), allow for instrument automation. For these reasons, MALDI has become an invaluable research tool in automated, high-throughput applications in biotechnology and proteomics.²²

1.3 TOFMS Instruments Used in This Research

1.3.1 Comstock LI/RTOF 210

Much of the initial research was performed using a Comstock LI/RTOF 210 reflectron TOFMS. This instrument has a dual-stage ion source with orthogonal acceleration (Figure 1.3b). Delayed extraction is required because of the orthogonal geometry. The pulsing scheme is seen in Figure 1.2d with a voltage of 325 V applied to the repeller plate and -2350 V applied to the acceleration plate. Due to limitations of the power supplies this instrument can only be operated in the positive-ion detection mode. Instrument parameters, such as source potentials, deflection plate voltages, Einzel lens voltage, and reflectron voltages, were optimized by R.C. Watson to achieve maximum resolution.²³

Laser desorption/ionization is achieved using either the 355-nm third harmonic of a Nd:YAG laser (Continuum Surelite II) or a nitrogen laser operating at 337 nm (Photon Technologies International GL 3300). The Nd:YAG laser has a fixed pulse rate of 10 Hz and a pulse width of 4-6 ns. The laser pulse energy is controlled by adjusting the Q-switch delay, with longer delays giving lower pulse energies. Pulse energies are

measured using a Digirad radiometer with a pyroelectric detection unit. Typical pulse energies vary depending on the application (as noted in each experimental section) but are usually in the range of 10 to 100 μJ . The beam profile is circular with a Gaussian energy distribution and the laser beam is typically focused to a diameter of approximately 10 μm .²³

The nitrogen laser has a variable pulse rate, from single-shot to 20 Hz, with a pulse width of 600 ps. The energy per pulse is controlled using a circularly variable neutral density filter purchased from Melles Griot. Pulse energies are measured using a Digirad R-752 radiometer (Terahertz Technologies Inc.). The beam profile is rectangular with dimensions of 3 x 6 mm at the exit port of the laser. The optical configuration is shown in Figure 1.7. All mirrors were aluminum films optimized for reflection of UV light. The 1.0-meter focal length cylindrical lens is used because the long dimension of the beam has a higher divergence than the short dimension. Considerable effort was required to keep the beam at a practical size by the time it reached the focusing lens (about 1.2 m) due to the high divergence of the beam. The 1.0-meter focal length lens and the cylindrical lens were used in combination to collimate the beam over this distance. A small portion of the beam was selected using an adjustable iris with an open diameter of about 6-mm. The beam was then focused using a 25-cm focal length lens. All lenses and the window on the mass spectrometer are quartz. To measure the spot size, the beam is focused onto burn paper that leaves an image of the beam. The spot size is then measured using Vernier calipers. In this manner the beam size at the focal point was determined to be 100 x 600 μm . The long dimension of the beam was oriented perpendicular to the flight axis to minimize problems with space focus.

The timing of events in TOFMS is of the utmost importance. A schematic representation of these events is seen in Figure 1.8. The firing of the laser triggers the beginning of each data collection event. The laser has a “sync out” port which generates a signal with a 19 V amplitude (specification by manufacturer is 24 V) and a 1.5 μs pulse width 1.0 μs prior to the laser firing. This signal is sent via BNC cable to a digital delay/pulse generator (Stanford Research Systems, model DG535). However, the DD/PG requires that the signal amplitude for an external trigger be less than 2.56 V so the signal is first sent through an attenuator to achieve an amplitude of 1.6 V. Table

1.1 shows the settings used to program the DD/PG to receive (from the laser) and transmit (to the instrument electronics) the timing signals. The DD/PG is set up to trigger on the leading edge of the sync out signal from the laser. The output signal of the DD/PG is then delayed relative to the input signal by 948 ns. This is because the sync out signal from the laser is sent 1.0 μs prior to the laser actually firing, and the transmission time through the BNC cable was measured to be 52 ns. The output from the DD/PG is a TTL voltage pulse with a 500 μs pulse width. The extended pulse width is used to prevent multiple triggers of the instrument in the event the laser should fire again prior to the next scheduled pulse (a misfire). The TTL pulse from the DD/PG is sent to the repeller plate power supply which marks the “zero” point of data collection and corresponds to the time when the laser pulse reaches the sample surface. The application of a potential to the repeller plate then occurs after a user-defined delay. The repeller plate voltage pulse begins the acceleration of the ions towards the flight tube. Data collection and manipulation, along with all other instrumental details are outlined in R. C. Watson’s M.S. Thesis.²³

Table 1.1 DD/PG settings

Output	Delay – channel A	Delay – channel B	Trigger	Threshold	Slope	Impedance
to AB, TTL	$A = T + 9.48 \times 10^{-7}$	$B = A + 0.00005$	External	+0.50 V	Positive	50 Ω

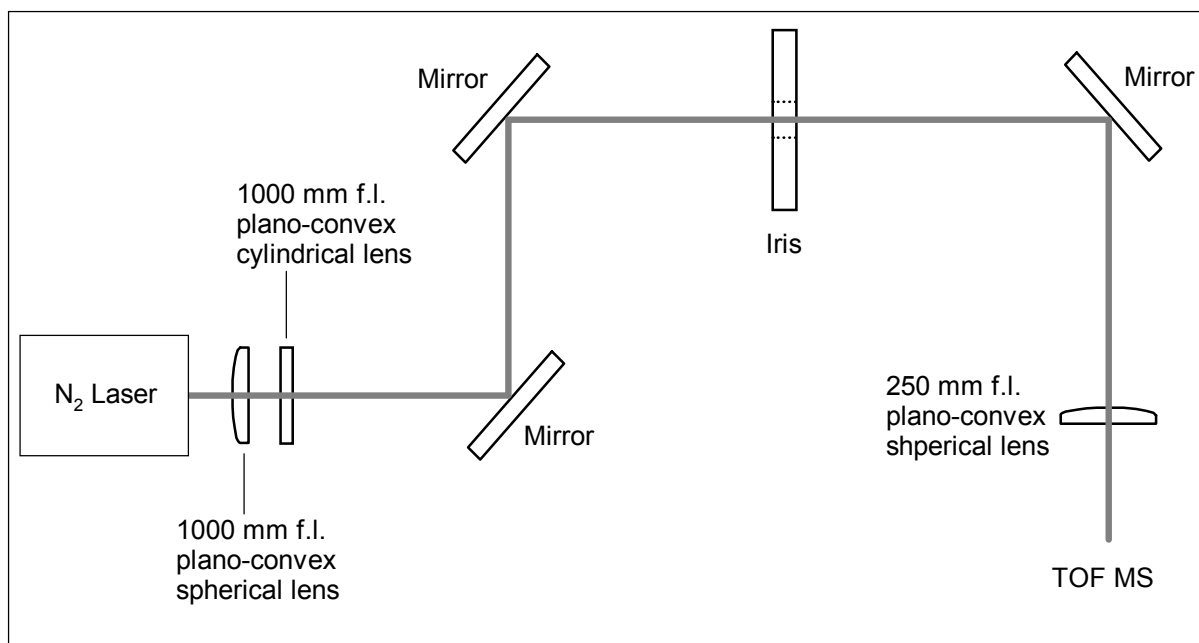


Figure 1.7 Optical setup when using the PTI 3300 nitrogen laser for desorption/ionization. All lenses are quartz, all mirrors are Al coated borosilicate glass. The laser beam is focused onto to the sample in the axial position. Pulse energy measurements are taken after the focusing lens.

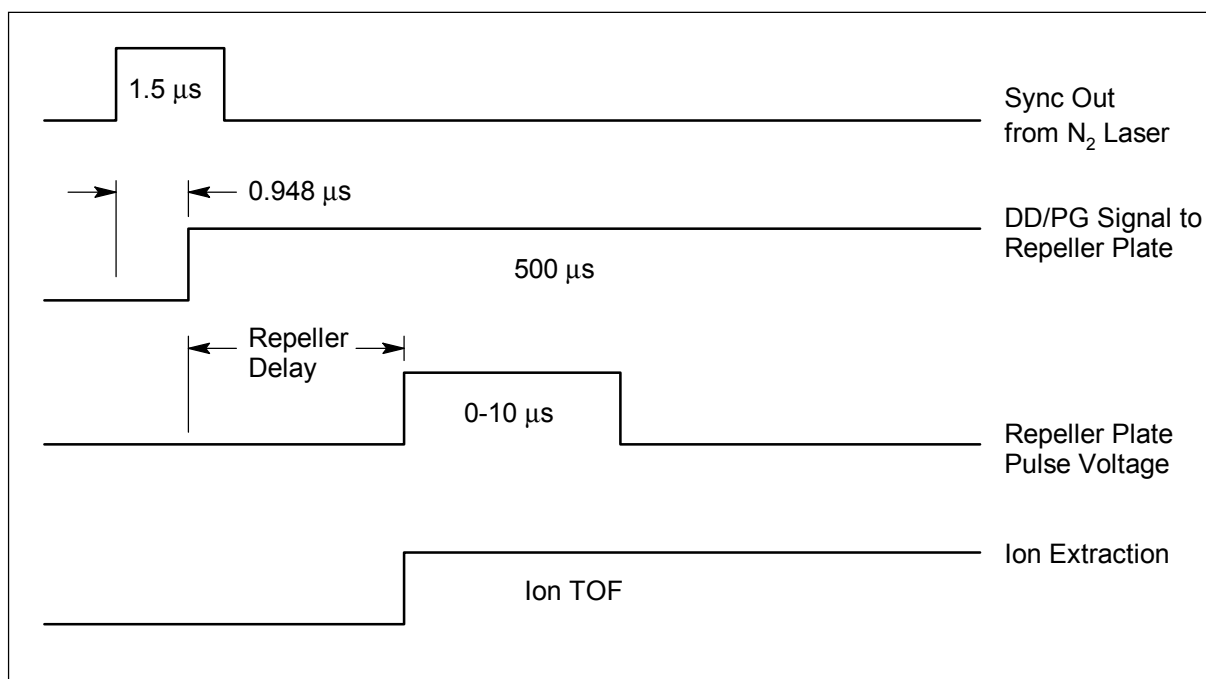


Figure 1.8 Sequence of timing events in a TOFMS experiment. The sync out signal from the laser is sent 1.0 μs prior to the laser firing. After the appropriate delay, the DD/PG triggers the repeller plate power supply as the laser hits the surface. The repeller plate is then pulsed after a user-selected delay time.

1.3.2 Kratos Kompact SEQ

This instrument can be operated in several modes: high mass or low mass, positive- or negative-ion detection, delayed or continuous extraction, linear or reflectron, and parent ion or PSD detection. Fewer instrumental details (timing, reflectron voltages, detector voltage, absolute laser energy, etc.) are known about the Kratos Kompact SEQ because of the integrated (“black box”) design. Whereas the Comstock RTOF/210 is a “research-grade” instrument, the Kratos Kompact SEQ was designed to be “user friendly.” This limits instrument control due to predetermined instrument conditions which are not easily varied (fixed voltage on the detector, only two possible acceleration potentials, fixed reflectron voltages, etc.). However, the Kratos instrument allows for faster, automated data collection and storage, a 20-well sample probe, and it can be operated in positive- and negative-ion mode. The mass resolution is also much better than that achievable with the older Comstock RTOF/210 because of design parameters discussed below.

All instrument parameters are controlled using a Microsoft Windows-based software package developed by Kratos (Launchpad version 1.2.2). This provides a “user friendly” interface with the instrument as well as complete instrument control, automation, data collection, and spectrum display. Data is collected by the computer and is immediately displayed as a mass spectrum. The time-of-flight information is not available to the user.

The ion source has a dual-stage design that uses a pulsing scheme as seen in Figure 1.2e. The repeller plate can be set at ± 5 kV or ± 20 kV. The polarity is positive for detection of positive ions and negative for negative ions. The extraction grid is initially at the same potential as the repeller plate. After the user-selected delay time, the extraction plate voltage is lowered to ± 4.2 kV or ± 17 kV. The acceleration plate and the flight tube are held at ground potential. The low voltage settings are used for analysis of low molecular weight compounds (<1000 Da) and the high voltage settings are used for compounds up to 250,000 Da. The sample is in an axial geometry (see Figure 1.3a). The high source voltages and axial geometry are the two main reasons for the increase in resolution over the Comstock RTOF/210. When the low source potentials are employed, the resolution at masses above 1000 Da is similar for both instruments.

A nitrogen laser from Laser Science, Inc. achieves desorption/ionization. The pulse energy is controlled using a variable neutral density filter and is automatically calibrated each time the instrument is operated. The laser power setting is a relative value from 0-180. The actual power to the sample is not measured directly but goes up in log scale from 0-180. Details of the optical configuration, such as incidence angle and beam size/shape, are not known.

In the linear mode, the flight path is 1.7 meters, and ions are detected by a discrete-dynode electron multiplier. The longer flight tube also helps increase the mass resolution. The reflectron is positioned approximately twelve inches from the ion source and has a curved field design.¹⁶ PSD spectra are collected by using an electrostatic mass gate at the exit of the ion source to select the parent ion. The gate allows a mass window of about 20 Da to pass. Again, the ions in reflectron mode are detected using a discrete-dynode electron multiplier.

1.4 MALDI-TOFMS

MALDI was first introduced by Hillenkamp and Karas in 1988 and has since revolutionized the role of mass spectrometry in the analysis of biopolymers and other high-mass compounds.²⁴ Since the original publication, there have been nearly 3000 articles discussing the theory and applications of MALDI. A large majority of MALDI studies use TOFMS due to the unlimited mass range of this mass analyzer and the compatibility with pulsed laser sources. Compounds as large as 1,500,000 Da have been detected using MALDI-TOFMS.⁷ This technique has been applied to a variety of samples such as proteins, peptides, oligonucleotides, oligosaccharides, non-covalent complexes, inorganic supramolecular assemblies, synthetic polymers, fullerenes, and dendrimers. Matrices have been discovered that allow for laser desorption/ionization in the UV and IR regions of the electromagnetic spectrum, however the majority of applications use UV lasers.

Even though ionization mechanisms are poorly understood, the pragmatic aspects of MALDI are simple. Figure 1.9 shows a schematic representation of the MALDI process. Matrix compounds for UV-MALDI are typically aromatic organic acids

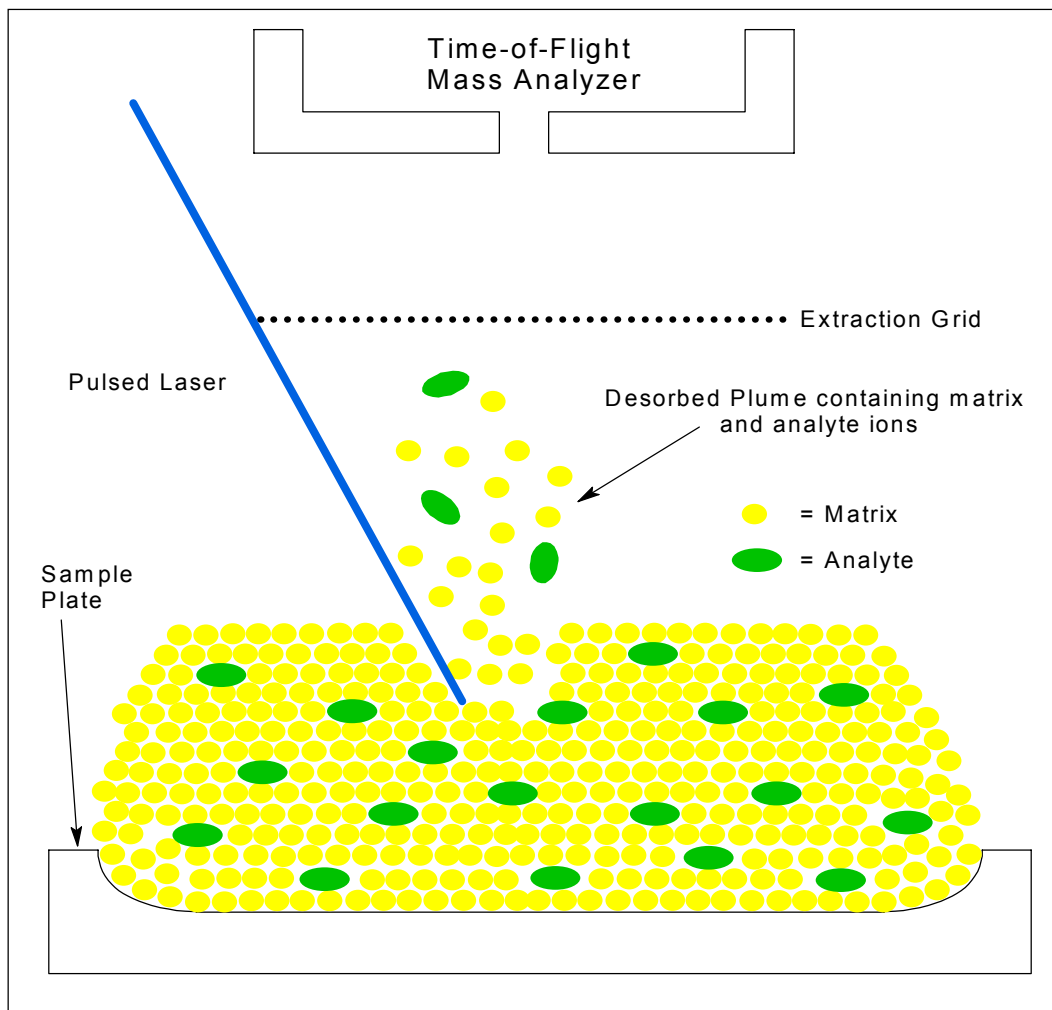


Figure 1.9 Schematic representation of the MALDI process. A small volume of solid is sublimed due to the laser pulse. The gas phase plume contains neutrals, ions and clusters of the matrix as well as analyte ions.

(benzoic and cinnamic acid derivatives) that have large extinction coefficients at the operating wavelength of the laser. Typically, the analyte does not absorb the laser radiation to any appreciable extent. Using the “dried-droplet” method, a solution of the analyte is mixed with a solution of the matrix (typically 0.5 μL each) and applied to the sample probe. The matrix is in large molar excess relative to the analyte, with typical ratios ranging from 200:1 to 5000:1. The droplet is then allowed to evaporate, resulting in a crystalline deposit. During crystallization the analyte is incorporated into the crystal lattice of the matrix. The laser energy is absorbed almost exclusively by the matrix due to its molar excess and high extinction coefficient, which causes desorption of a small volume of the solid sample. The matrix plays an essential role in desorption and

ionization of non-volatile analytes. During desorption the analyte is carried into the gas-phase along with the matrix, where analyte ionization takes place. Desorption results in a relatively dense gas-phase plume that expands into the vacuum region of the mass spectrometer. Ions are then sampled and separated by the mass spectrometer. Ions generated by MALDI are typically detected as singly charged species with little to no fragmentation.

1.4.1 Experimental Parameters in MALDI

Sample preparation methods, matrix choice, matrix-to-analyte ratio, laser wavelength, laser pulse width, incidence angle of the laser beam, and laser fluence are all parameters that have been investigated by other research groups. The pulse width and incidence angle have little effect on the results.²⁵ All of the other parameters can have a dramatic influence on the success or failure of MALDI. The importance of matrix choice and matrix-to-analyte ratio is illustrated through examples found in Chapter 3 and Chapter 4.

Many researchers have discussed the effects of sample preparation conditions. By far the most common method is the dried droplet method first introduced by Hillenkamp and Karas.²⁴ Most of the other preparation methods are variations of the dried droplet method.²⁶ The most important concept of sample preparation is to homogeneously incorporate the analyte into, or at least on the surface of, the crystal structure of the matrix. Complete homogeneity is not possible, but some methods are better than others. More homogeneous distribution of the analyte leads to more reproducible results. The method we use to increase homogeneity is fast evaporation of the solvent during drying. In order to achieve this, the sample spot is produced by the dried droplet method from a binary solvent mixture that usually includes water. The dried spot is then redissolved in methanol or acetonitrile and dried under nitrogen. The fast evaporation does not allow the formation of large crystals. As seen in Figure 1.10, this method results in smaller more homogeneous crystals and shows dramatic improvements in spot-to-spot reproducibility.

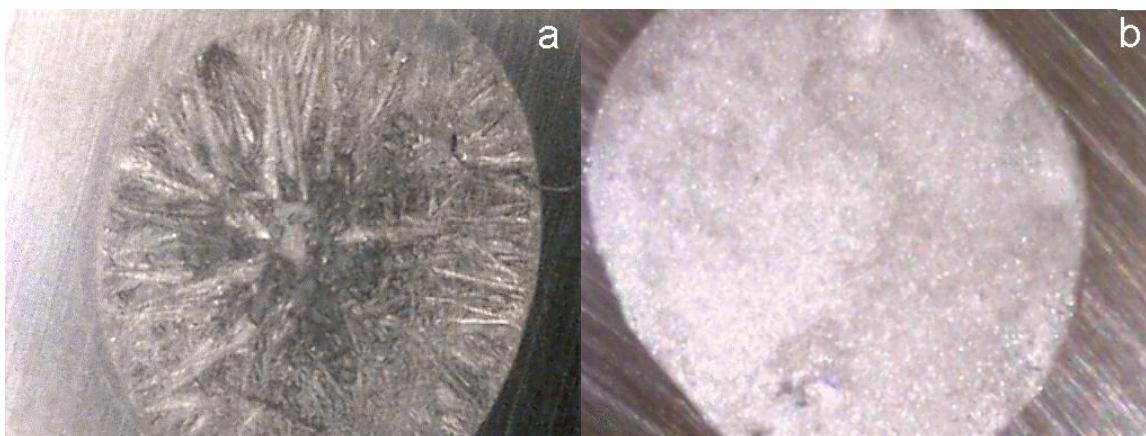


Figure 1.10 Images of DHB sample spot showing the difference in crystal size before (a) and after (b) recrystallization. The sample in (a) was redissolved in methanol and evaporated under a stream of nitrogen to produce the sample seen in (b). The spots are about 3 mm in diameter.

Another important aspect of sample preparation is the presence of contaminants. Although MALDI is generally considered to tolerate salts and detergents, as compared with electrospray, there are limits. Table 1.2 shows some typical values for contamination levels that affect MALDI results.²⁷ The deleterious effects of these compounds are most commonly due to disruption of the co-crystallization of the matrix/analyte mixture. Many biological samples have large amounts of buffer and salts. There are several ways to desalt the sample prior to MALDI analysis. Methods used prior to mixing the analyte with the matrix include gel electrophoresis, dialysis, and ultrafiltration. However, these clean-up procedures are time-consuming. Several researchers have shown that the sample can be “washed” after spot preparation.²⁸ Washing is achieved by running a small amount of cold water over the dried spot. This method removes salts but leaves the protein and matrix behind. This trick provides a simple and rapid method for desalting protein and peptide preparations.

By far the most common laser used for desorption/ionization is a nitrogen laser. Many of the useful MALDI matrices have a strong absorbance at the output wavelength of 337 nm. Low cost and robustness are two more important reasons many researchers use a nitrogen laser. Groups interested in formulating ionization mechanisms for MALDI will typically use a variety of other lasers, including a frequency-tripled or quadrupled Nd:YAG (355 nm and 266 nm, respectively), excimer lasers with outputs in the range of 193 – 308 nm, and CO₂ lasers that operate at 10.6 μm. IR-MALDI typically results in

Table 1.2 Common contaminants in MALDI and the approximate tolerance limit.

Buffer of Detergent	Tolerance ^a
NaCl	50 nM
Phosphate	10 mM
Tris Base	50 mM
Urea	1 M
Guanidine	1 M
PEG 2000 ^b	0.1% (w/v)
Sodium Dodecyl Sulphate ^c	0.01% (w/v)
CHAPS ^c	0.01% (w/v)
Triton X-100 ^b	0.1% (v/v)
n-octyl- β -glucopyranoside ^d	1% (v/v)

a – Tolerance values are approximate and may vary with matrix and analyte concentration

b – Can suppress ionization completely, detergent should be avoided if possible

c – Reduces spectrum quality and signal intensity

d – No bad effect, may actually improve results

similar mass spectra but is believed to have an entirely different mechanism. Energy absorption in the IR region involves vibronic transitions. Extinction coefficients of the matrices used for IR-MALDI are several orders of magnitude lower than their UV counterparts (10^3 l/mol/cm versus 1-50 l/mol/cm). There is also a dramatic difference in the penetration depth of the laser.²⁹ In UV-MALDI penetration depth is on the order of several hundred nanometers, while in IR-MALDI penetration depth is tens of micrometers. Because of this difference IR-MALDI requires much higher laser fluence and, due to the amount of material removed during desorption, more sample.

In both IR and UV-MALDI there is a threshold fluence for analyte ion production. The relationship between ion production and laser fluence is also very non-linear.²⁶ At low laser fluence no ions are observed in the spectrum, however a small increase can cause large ion signals. This effect is known as the threshold fluence. This value varies for each matrix, as will be illustrated in Chapter 3. Ion production continues to increase above the threshold, but at the cost of resolution and cluster formation. For this reason,

most MALDI experiments are performed with a laser fluence just above the threshold value.

1.4.2 Ionization Mechanism in MALDI

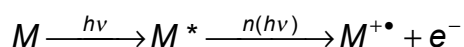
Despite thousands of experiments performed using MALDI, there is still no single theory that explains all the observed results.³⁰ Even combined theories are poorly understood and require much more study. The inadequacy of theory has meant that successful results are obtained by trial-and-error. The broad range of samples, matrices, and experimental parameters employed in MALDI has complicated the explanation of the ionization mechanism. Conditions such as laser wavelength, laser power, and matrix-to-analyte ratio must be optimized for different analytes and matrices. For example, positional isomers of dihydroxy benzoic acid have been shown to produce different results under different conditions.³¹ In this case success was partially attributed to the incorporation of protein into the matrix crystals (or at least adsorption onto crystal surfaces), and partially to the wavelength of the laser used for desorption/ionization. Even though all matrices produced acceptable results, the experimental conditions had to be optimized for each isomer. The only generally accepted conclusion for success in MALDI is that localization of the analyte in the crystal structure or on the crystal surface is required. A detailed discussion of ionization pathways in MALDI is beyond the scope of this dissertation, but it is important to recognize the complexity of the process.

Zenobi and Knochenmuss have recently published the first review article discussing the ionization mechanism in MALDI.³⁰ There are a variety of pathways that are currently being considered for ion formation in MALDI. These pathways include gas-phase photoionization, ion-molecule reactions, disproportionation, excited-state proton transfer, energy pooling, thermal ionization, and desorption of preformed ions. Due to the complexity of the desorption event, a number of these pathways act in concert to produce analyte ions.

When discussing the ionization mechanism it is convenient to discuss primary and secondary ion formation, where primary ions are the first ions generated (usually matrix ions), and secondary ions (usually analyte ions) are created by reactions of primary ions and neutral molecules. The three types of ions observed in MALDI

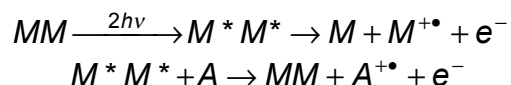
experiments are radicals, protonated/deprotonated, and cationized metal adducts. Analyte ions are most commonly observed as protonated species, whereas matrix ions are commonly observed as both radicals and protonated species.

The first possibility for primary ion generation is photoionization. Because matrix compounds have high extinction coefficients, this pathway seems the most straightforward. A general scheme for this type of ionization is shown in the following reaction.



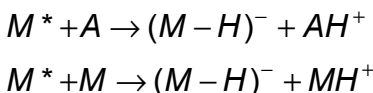
M is used to represent matrix. Typically, matrix compounds have excited-state lifetimes on the order of 5 to 10 nanoseconds. After absorption of one photon, the excited-state species may absorb one or two additional photons, which would then lead to ionization. Consider the ionization potential for 2,5-DHB, which is 8.05 eV as determined by molecular beam experiments.³² Ionization by a nitrogen laser would then require a three-photon absorption process because each photon only has 3.68 eV of energy. Statistically, this process seems unlikely due to the typical irradiance values used in MALDI ($10^6 - 10^7$ W/cm²) and the number of gas-phase molecules created during desorption. Karbach and Knochenmuss³² conducted three-photon ionization experiments and the process was found to be very inefficient even at an irradiance of 10^8 W/cm². Further evidence against multiphoton ionization is that MALDI has been found to depend on the number of photons delivered to the sample, not on the rate at which they are delivered.³³ Multiphoton absorption mechanisms show a clear dependence on the rate at which photons are delivered to the sample. The ionization potential decreases for clusters of matrix molecules, but still requires at least three photons. The ionization potential of most matrices commonly used in UV-MALDI are around 8 eV which suggests that direct photoionization is not a reasonable pathway to ion formation. However, a photo/thermal model could explain a two-photon ionization. The rapidly expanding, gas-phase plume generated by MALDI has been found to be hot, approximately 600 K.³⁴ So thermal energy might make up for small energy deficits in two-photon absorption.

Even though multiphoton absorption does not completely explain ionization observed in MALDI, excited-state matrix molecules are still believed to play an important role. Many researchers now believe that more than one excited matrix molecule is needed in order to explain ionization in MALDI. One of the most plausible models proposed involves energy pooling of multiple excited-state matrix molecules, as shown in the following reaction schemes.



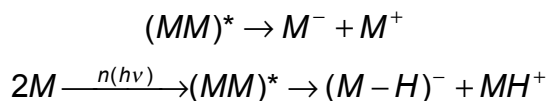
For DHB, the excited-state density, or the number of excited-state molecules in the gas-phase plume, is estimated to be about 1 out of 4 at threshold laser fluences.³⁵ Luminescence was quenched at excited-state densities typical of MALDI plumes because of the reaction of two excited-state molecules. Further evidence for the energy-pooling model was found through computer modeling studies.³² The ion production was calculated using measured parameters for DHB (excited-state lifetime, ionization potential, energy of first excited-state, etc.) without consideration of a pooling mechanism. The results predict a 10-fold increase in ion production when pooling is considered. Additional evidence supporting coalescence of excited-state molecules as an ionization mechanism is found in the “matrix suppression effect” observed in MALDI.³⁶ At sufficiently high analyte concentrations the matrix ion signals are completely suppressed. There was an analyte size dependence for the effect as well. The authors conclude that this effect is most easily explained if ionization occurs as a result of exciton pooling. From the above observations, energy pooling evidently results in higher ion production than single-molecule multiphoton processes.

Excited-state proton transfer was the first model proposed as an ionization mechanism in MALDI.³⁷ This process seems likely because it only requires absorption of one photon and the excited-state molecules are presumed to be much more acidic than ground-state molecules. The excited-state acidity of aromatic hydroxyls and amines has been shown to have pK_a values 9 units lower than ground state species.³⁸ Using this model the following reaction pathways have been proposed.



However, there is no direct evidence that common MALDI matrices have the ability to undergo excited-state proton transfer reactions.³⁹ Furthermore, many of the compounds that do exhibit excited-state proton transfer activity, such as salicylic acid, do not perform well as MALDI matrices. Excited-state proton transfer reactions would also not account for the presence of radical species in the observed mass spectra. However, in solution the molecular environment (i.e. solvation) dramatically affects excited-state proton transfer. At present, there is not enough information about the molecular environment of the gas-phase plume to make definitive statements about the role of excited-state proton transfer as an ionization mechanism.

Even less is known about the possibility of disproportionation reactions. Many matrices provide equal intensity signals in both the positive- and negative-ion mode for analytes such as peptides. This phenomenon is most easily explained by consideration of disproportionation reactions. Given that matrix clusters are known to form, as they are observed in the mass spectrum, the following reactions may occur.



The discussion so far has pointed toward the involvement of clusters or pairs of matrix molecules. The energetics involved in proton disproportionation for several matrix dimers is about 5 eV, which is well within the range of a two-photon excitation by a nitrogen laser.⁴⁰

In some instances, desorption of preformed ions has been shown to play a key role in the observed mass spectrum. This model assumes that the ions are present in the solid phase prior to laser desorption. Most of the studies done on this topic incorporate ionic species in the MALDI preparation⁴¹ or derivatize peptides with ionic groups such as phosphonium groups.⁴² This model has not been extensively tested for

analytes such as peptides or proteins. In most systems studied by MALDI, the contribution of pre-formed ions is considered to be relatively small, if present at all.

Secondary ions observed in MALDI can be formed by reaction with excited-state matrix molecules, matrix ions, or by cationization. The most important reactions are those leading to protonated or cationized species, as these are the most commonly observed analyte ions. While primary ions are formed during desorption and initial expansion of the MALDI plume, secondary ions are formed in the gas-phase.

Gas-phase proton affinities of several common matrices have been measured and are found to be in the range of 183-225 kcal/mol.³⁰ The proton affinities of peptides and proteins are on the order of 240 kcal/mol. Therefore, proton transfer from the matrix to a neutral gas-phase peptide or protein will always be favored thermodynamically. One published study of ion angular and velocity distribution in the MALDI plume helps verify this pathway.⁴³ The authors measured the ion densities of matrix and analyte ions in the gas-phase plume over a range of matrix-to-analyte ratios and obtained two important results. First, the analyte ions have lower velocities than matrix ions by about 100 – 200 m/s. Second, by imaging the matrix ions and analyte ions, they showed that there is a depletion of matrix ions in the region of the protonated analyte ions. Interestingly, HCCA with a proton affinity of about 202 kcal/mol typically produces multiply charge protein ions, whereas sinapinic acid with a proton affinity of about 210 kcal/mol results in singly charged protein ions. This difference is presumably due to multiple proton transfer due to the lower proton affinity of HCCA.⁴⁴

Many analytes are detected as metal-ion adducts such as $[M+Na]^+$. In some instances these cations are the only species observed for an analyte. Liao and Allison⁴² observed that this process depends, in the case of hexatyrosine, on the choice of matrix and the sample preparation conditions. Their results show that sinapinic acid produces $[M+H]^+$ ions almost exclusively, HCCA produces an equal mixture of $[M+H]^+$ and $[M+Na]^+$, and DHB produces $[M+Na]^+$ almost exclusively when an excess of NaCl was added to the samples. They also report that the results are similar when no excess NaCl is added. However, when HCCA was desalted using ion-exchange resins, the $[M+Na]^+$ peak disappeared. NaCl impurities in the matrix are responsible for

cationization. It is not clear why some matrices result in cationization and others do not. However, several other studies showed that cationization takes place in the gas phase.

Much more research is needed to fully understand the pathways to ion formation in MALDI. The variety of samples and experimental conditions make elucidation of an ionization mechanism difficult. Different ionization pathways dominate for different analytes, matrices, and experimental conditions. No single pathway is responsible for the ions observed in MALDI.

Chapter 2 – LDI-TOFMS of Borate Glass Samples

2.1 Introduction

Analysis of solid samples using direct laser desorption/ionization often suffers from interference.⁴⁵ For example, attempting to quantify the amount of lead in paint is difficult because of the different pigments used. If both samples had the same amount of lead, analysis of white paint could show a different level of lead than black paint. The black paint would absorb more light (energy) than the white paint, which could result in the production of more ions. This phenomenon is known as matrix interference. The two general types of interference are chemical and physical. Examples of chemical interference include suppression or enhancement of ionization, adduct formation, and speciation. The classic example of physical interference is sample heterogeneity.

X-ray fluorescence analysis suffers from similar matrix effects, most notably heterogeneity and particle size distribution. In 1957, Fernand Claisse proposed a sample preparation method to overcome these matrix effects.⁴⁶ This method involves heating a mixture of the sample and an excess of lithium or sodium borate (the flux) to a temperature slightly higher than the melting point of the flux. Molten lithium borate has an exceptional ability to solvate most solids, including refractory materials. After casting of the molten mixture, the single-phase glass bead is a homogeneous solid solution.

The goal of this research project is to use lithium borate fusion as a sample preparation technique to reduce matrix effects in LDI-TOFMS. We would also like to investigate the feasibility of using this technique to quantify trace elements in a variety of solid samples, such as ores, soil, and paint. This chapter will present an introduction to the fusion technique, discuss experimental details and results, and comment on the usefulness of the method.

2.2 Lithium Borate Fusion Technique

2.2.1 Advantages and Disadvantages

The most significant advantage of this sample preparation technique is the production of a homogeneous sample. Analytical chemists are usually given a small

sample that has been collected from a larger bulk material, such as a soil sample or an ore deposit. One of the most important challenges for an analytical chemist is to ensure that the data collected from a sample is representative of the bulk material.

Heterogeneity in the analytical sample can lead to erroneously high or low values.

Homogenization of the sample helps ensure that the quantitative data obtained describe the actual contents of the sample accurately.

Matrix effects can also skew the data from the true value. The lithium borate fusion technique provides a standardized sample preparation method that should help eliminate variability in matrix effects. This is not to say that a matrix effect will not be present but that the effect will be similar for a wide variety of sample types.

The fusion technique also offers a convenient way to add an internal standard to the sample. Addition of known amounts of analyte will help quantify an unknown amount of a substance. The addition of an internal standard is particularly relevant to LDI-TOFMS because of the shot-to-shot variability observed. Fluctuations in laser intensity lead to differential amounts of desorbed material from shot-to-shot, which makes quantification by LDI-TOFMS difficult. However, relative peak intensities will remain constant from one spectrum to the next. An internal standard can be used to judge changes in relative peak intensity and therefore allow quantification.

The biggest disadvantage of the fusion technique is dilution of the sample. In order to form a single-phase glass there must be a certain ratio of sample-to-flux. This ratio depends on the flux used, but is typically between 1:4 and 1:6. Trace element detection is therefore more difficult using this technique. The limit of detection is expected to be substantially higher than for analysis of pure samples.

Accurate determination of volatile or semi-volatile species is difficult because the mixture must be heated above the melting point of the flux. Fusion temperatures are typically in the range of 800 to 1100 degrees centigrade. Elements and compounds that have a significant vapor pressure at these temperatures will be lost during fusion. Volatile elements such as mercury are difficult to quantify using the fusion technique.

2.2.2 Fluxes and Additives

There are a variety of fluxes and additives available for different samples. Additives are used to assist in glass formation, control oxidation/reduction chemistry and achieve an appropriate viscosity and surface tension in the molten state. Components in some samples have a tendency to cause the glass to become brittle and crack. Addition of SiO_2 , Al_2O_3 , or GeO_2 can improve the glass stability. Most fusions are carried out in platinum crucibles because they are inert and can withstand high temperatures. However, if the sample contains sulfides or oxidized compounds the crucible can be irreversibly damaged by chemical attack. An oxidizing agent, such as BaO_2 , CeO_2 , or KNO_3 can be added to maintain an oxidizing environment and prevent crucible damage. Finally, some fluxes and flux/sample combinations will have a molten state that wets the surface of the crucible. This makes removal of the molten solution and casting difficult. In this instance, a small amount (1-3% by weight) of a non-wetting agent, such as KI, is added to increase the surface tension. Most alkali metal bromides and iodides are good non-wetting agents for use with platinum crucibles.

The most common fluxes used in XRF sample preparation are alkali borates, such as sodium tetraborate, lithium tetraborate and lithium metaborate. Table 2.1 gives a list of samples and fluxes used to prepare homogeneous glasses.⁴⁷ In general, lithium metaborate is used when acidic oxides (i.e. silica) are present, whereas lithium tetraborate is used when basic oxides (i.e. carbonate) are present.⁴⁸ A combination of lithium metaborate and lithium tetraborate is probably the most versatile flux. The ratio of the two can be varied to accommodate different amounts of basic or acidic oxides.

Table 2.1 List of samples and fluxes used to generate a homogeneous glass.

Flux	Sample
Sodium Tetraborate $\text{Na}_2\text{B}_4\text{O}_7$	Iron ores, Bauxites Sulphide ores, Ferroalloys
Lithium Tetraborate $\text{Li}_2\text{B}_4\text{O}_7$	Cements, Silicate rocks Aluminosilicates, Minerals
Lithium Metaborate LiBO_2	Silicate rocks Silica-alumina refractories

2.3 Experimental Details

2.3.1 Materials

Ultrapure-grade lithium metaborate and lithium tetraborate and lithium bromide, a non-wetting agent, were purchased from SPEX CertiPrep, Inc. Potassium iodide, a non-wetting agent, was purchased from Aldrich. All flux materials and additives were stored in a desiccator to prevent water absorption and facilitate accurate mass measurements. The epoxy used for mounting glass beads was purchased from Struers, Inc. Yttrium oxide was purchased from Aldrich. Zinc oxide was purchased from Alpha Aesar. One of the soil samples was obtained in southwest Virginia and the other from NIST (SRM 2709).

A Claisse Fluxer 7132 Bis platinum crucible from SPEX CertiPrep was used for fusion. The crucible is made of an 95% Pt/5% Au alloy which provides a non-wetting surface. A 30 mm 95% Pt/5% Au alloy mold for casting was purchased from Alpha Aesar. A Meker type high-temperature burner was purchased from VWRSP. The crucible clamping assembly was manufactured in-house and will be described in detail in the next section.

1000 $\mu\text{g/mL}$ standards of Fe, Mg, Mn, and Zn were purchased from SPEX Plasma Standards and were made up in 2% HNO_3 . These solutions were used to make series of standards for flame atomic absorption spectroscopy. Concentrated acids were purchased from Fisher Scientific.

2.3.2 Glass Preparation

The duration of the fusion depends on the temperature, amount and composition of the sample, and the composition of the flux. The total mass (sample plus flux) added to the crucible was typically 300 mg. Small amounts were used in order to keep the glass bead small and reduce the fusion time. The fusion time should be minimized to reduce the loss of volatile components. In general, the melt was visually inspected until particulates appeared to dissolve, then the melt was heated for several more minutes to ensure dissolution. The long stainless steel rods on the clamping assembly allow for constant stirring of the melt. Constant mixing helps ensure homogeneous incorporation

of the sample in the resulting glass. Fusion typically takes six to ten minutes of heating and mixing. The melt is then poured into a preheated platinum mold and allowed to cool. A non-wetting agent was added to all sample preparations to prevent the melt from sticking to the crucible and to ensure that the pour from the crucible was complete. The non-wetting agent is typically added at a concentration of 1-3% by weight. Initially, potassium iodide was used as a non-wetting agent but resulted in very large potassium ion signals in the mass spectra. Subsequent fusions were conducted using lithium bromide as a non-wetting agent.

A successful preparation yields a small glass bead, typically 0.5 cm across the flat surface, with no visible particulates. The surface in contact with the mold during cooling is smooth and polished, so that no surface preparation is required prior to mass analysis.

Certain flux compositions, 100% LiBO_2 for example, do not result in amorphous samples upon casting and cooling. The results of several sample preparations were crystalline rather than amorphous. Another factor that affects the glass-forming properties of the melt is the concentration of the sample. At high concentrations, greater than 25%, the melt would crystallize upon casting. For this reason, care must be taken in choosing the flux composition and the amount of sample incorporated into the melt.

2.3.3 Flame Atomic Absorption Spectroscopy

An acid digestion of the Virginia soil sample was performed in order to conduct FAAS experiments on selected elements. The digestion procedure was adapted from EPA method 3050B and is found in Appendix A. This procedure is not a total acid digestion procedure, meaning that alumino-silicates are not dissolved. However, it does dissolve elemental oxides, such as iron oxide.

Analysis of the acid digestion was conducted using a model 3110 Atomic Absorption Spectrometer from Perkin Elmer with a multi element lamp from Fisher Scientific. The instrument manual provides a “characteristic concentration” for analysis of common elements.⁴⁹ This value is the solution concentration that will give an absorbance of 0.2. The manual also provides a typical linear dynamic range for each element. This value gives the approximate concentration at which the calibration curve

becomes non-linear. A series of standards were prepared for each element based on the suggested values in the manual. Table 2.2 shows the instrument parameters and standard concentrations used to generate calibration curves for the chosen elements. The digestion solution was diluted by a factor of 100 for the analysis of Fe and a factor of 10 for Mg, Mn, and Zn. Samples were diluted with water to help reduce the acidity of the solution and minimize damage to the burner.

Table 2.2 Instrument conditions and standards prepared for flame atomic absorption spectroscopy of the Virginia soil.

Element	Absorbance Wavelength (nm)	Characteristic Concentration (ppm)	Linear Dynamic Range (ppm)	Standards Prepared (ppm)
Fe	252.3	8	10	20, 10, 5, 1
Mg	202.6	9	10	10, 5, 1, 0.5
Mn	279.8	5	5	10, 5, 1, 0.5
Zn	213.9	1	1	5, 1, 0.5, 0.1

2.3.4 LDI-TOFMS

Mass spectrometric analysis was performed on the Comstock LI/RTOF 210. LDI was achieved using the third harmonic (355 nm) of a Nd:YAG laser. Details of instrumentation and experimental setup can be found in section 1.3.1 and the M.S. thesis of R. C. Watson.²³ Typical laser energies were 40 μ J/pulse to 1.0 mJ/pulse, depending on the intensity of the signal of interest. In general, it is best to use the lowest pulse energy possible as higher energies produce more intense matrix ion signals. All spectra were recorded in the positive, reflectron mode.

The glass beads were set in an epoxy mold so they could be mounted to the sample probe (see Figure 2.1). The smooth, flat surface resulting from contact with the mold during casting was always the surface presented to the laser. A small hole was drilled into the center of the epoxy so that a small screw could be used to attach the sample to the probe. The flat surface of the bead was positioned 4.3 cm below the central axis of the flight tube, just below the repeller and extraction plates, and positioned between these two plates. The probe is a 9.75-inch long, 1-inch diameter

stainless steel rod. A teflon seal allows the probe to be rotated without increasing the pressure in the mass spectrometer. The sample is rotated after acquiring a series of spectra to expose a smooth, clean surface.

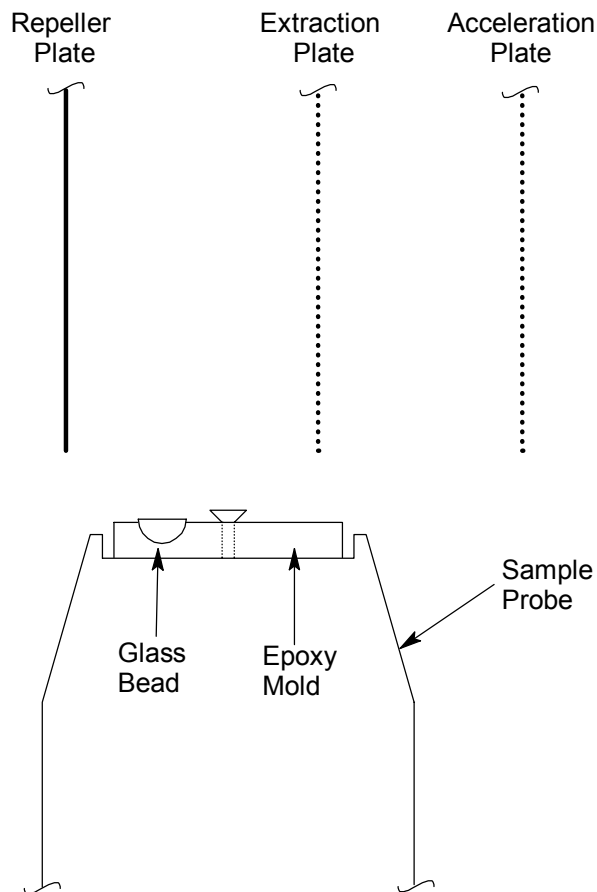


Figure 2.1 Schematic showing how the glass beads are mounted to the sample probe and the position of the sample relative to the ion source and flight tube.

The repeller delay must be optimized for a small mass range because all ions have a similar initial kinetic energy distribution. After desorption/ionization, heavier ions will have a lower velocity and therefore require more time to reach the flight axis prior to acceleration.²³ The repeller delay can also be used to reduce low-mass background signals when analyzing high-mass species. The optimum repeller delay for the low-mass region (10-40 Da) is 5-7 μs . The optimum delay time for an analyte with a mass of 100 Da is 18-20 μs . When the delay is optimized to detect the analyte, the low-mass ions (background signals) will travel past the flight axis by the time the repeller plate is pulsed. The low-mass ions are either pumped away by the vacuum or are so dispersed

at the time of acceleration that they are not focused by the mass spectrometer. In either case the intensity is significantly reduced. This point will be illustrated in Section 2.4.2 and Figure 2.3. In this way, the repeller delay offers a way to reduce interference from low-mass ion signals, providing there is a significant mass difference.

2.4 Results and Discussion

2.4.1 Flame Atomic Absorption Spectroscopy

To conserve the NIST SRM, we chose to work with the local soil first to test the validity of the LDI-TOFMS method. The concentration of major elements in the Virginia soil sample were found by performing an acid digestion procedure followed by FAAS. Absolute quantification was not the goal, but rather to gain approximate concentrations. Later LDI-TOFMS experiments were to be conducted using soil and other samples obtained from NIST. Iron, magnesium, manganese, and zinc were chosen for analysis because of the low chance of chemical interference during FAAS and their abundance in most soils. By FAAS the concentration of elements in Virginia soil were found to be 30,000 $\mu\text{g/g}$ for iron, 2900 $\mu\text{g/g}$ for magnesium, 600 $\mu\text{g/g}$ for manganese and 400 $\mu\text{g/g}$ for zinc.

2.4.2 LDI-TOFMS of Glass Samples

Pure lithium borate glasses were analyzed first to assess the nature of the background signal. The spectrum did not change significantly when different ratios of LiBO_2 and $\text{Li}_2\text{B}_4\text{O}_7$ were used to prepare the glass. The low-mass region typically contains ion signals from lithium (^6Li and ^7Li), boron (^{10}B and ^{11}B), sodium (^{23}Na), and potassium (^{39}K and ^{41}K). There is also a series of peaks between 55 and 57 Da that are assigned to the different isotopes of LiBO_2 . The presence of these peaks in the spectrum automatically eliminates the possibility of iron and manganese analysis by this technique due to overlapping masses. The mass for the major isotope of iron is ^{56}Fe and the only stable isotope of manganese is ^{55}Mn . However, there are no significant signals at higher mass. Analysis using this technique will most likely be limited to elements with an atomic mass greater than 57 Da because of the intense matrix signals.

The study began by doping metal oxides into the borate glass. ZnO was added to a 2:1 mixture of LiBO_2 and $\text{Li}_2\text{B}_4\text{O}_7$ at a concentration of 9.2% by weight (7.5% Zn). The mixture was then heated to approximately 1100°C for 10 minutes. The melt was then cast into the platinum mold and allowed to cool. This resulted in a transparent glass with no visible particulates, meaning the ZnO was dissolved by lithium borate. Figure 2.2 shows the TOFMS observed, as well as a comparison to the blank. The major isotopes of zinc appear in the spectrum as well as a peak at 128 Da. This peak could either be $^{64}\text{Zn}_2^+$ or $^{64}\text{ZnO}_4$. The laser pulse energy was 3 mJ and the repeller delay was set to 30 μs . This is not the optimum delay for this mass range, but shorter delay times resulted in a large background signal that saturated the detector. As discussed in Section 2.3.4, increasing the delay allows a majority of the low mass matrix ions to be dispersed prior to acceleration. As seen in Figure 2.3, the background signal at shorter delay times consists mostly of unresolved metastable ions, which results in very broad peaks over the entire low mass range. Identical instrument conditions were used to collect both spectra, with the exception of the repeller delay. The top spectrum was collected using a repeller delay of 17 μs while the bottom spectrum was collected using a delay of 35 μs . This illustrates the advantage of the perpendicular geometry employed, which allows the use of long delay times. When lower pulse energies were used in order to reduce the background signal, no zinc peaks were detected. This result was disappointing considering the high concentration of ZnO doped into the glass and the relatively low signal intensity.

A pressed pellet of pure ZnO was analyzed by LDI-TOFMS in order to assess the identity of the peak at 128 Da. The resulting mass spectrum is shown in Figure 2.4. There are a series of peaks that correspond to Zn, ZnO, and Zn_2 , Zn_2O , Zn_2O_2 , and Zn_3 singly charged, positive ions. The insets show the calculated isotopic distributions for Zn and Zn_2 . The metal-oxide peaks have similar isotopic distributions to the respective metal series, as oxygen only has one major isotope. The metal peaks (Zn and Zn_2) are more intense than the respective oxide peaks. This result suggests that the peak at 128 Da in Figure 2.2 is $^{64}\text{Zn}_2$, not $^{64}\text{ZnO}_4$. However, it is unclear why there is only one peak at 128 Da in Figure 2.2.

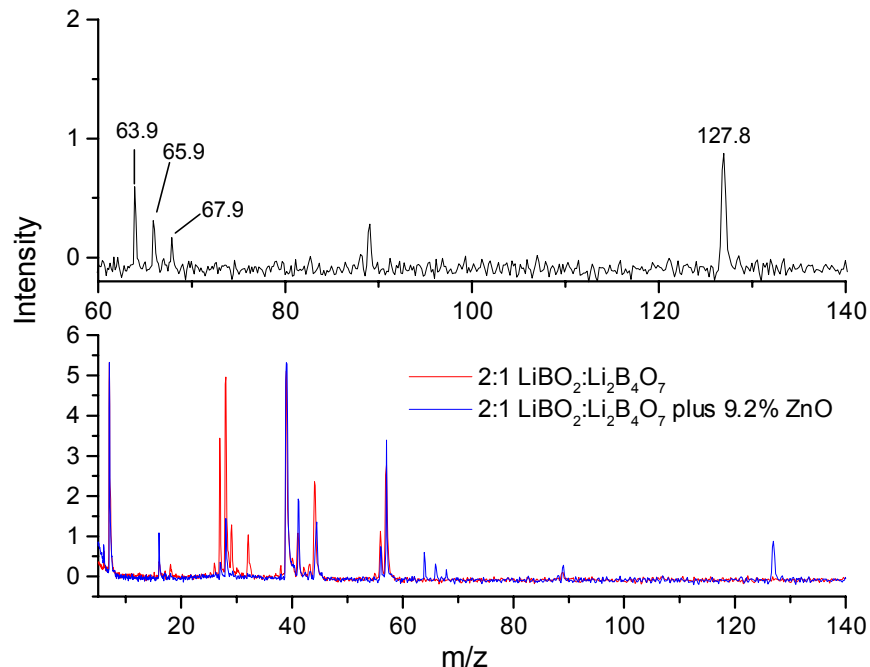


Figure 2.2 LDI-TOFMS of a glass bead that contains 9.2% (w/w) zinc oxide. The three major isotopes of zinc are clearly seen as well as a peak that is believed to be $^{64}\text{Zn}_2$ at 128 Da. Both spectra were recorded under identical instrument conditions.

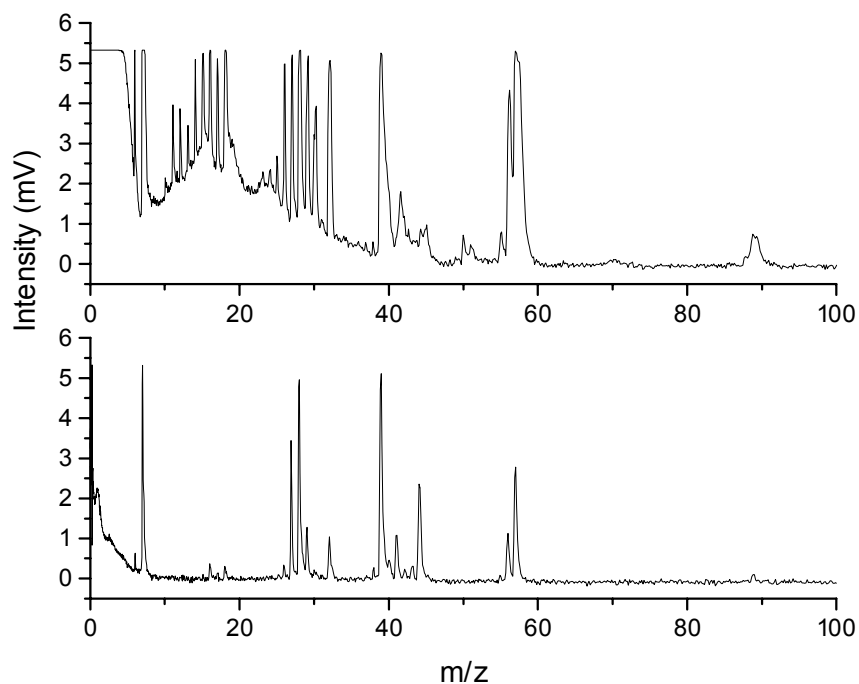


Figure 2.3 Mass spectra of a blank glass bead made using a 2:1 mixture of LiBO_2 and $\text{Li}_2\text{B}_4\text{O}_7$. The spectra were collected using a repeller delay of $17\ \mu\text{s}$ (top) and $35\ \mu\text{s}$ (bottom). All other instrument conditions were identical. This illustrates how longer delay times can be used to eliminate low mass matrix ion signals.

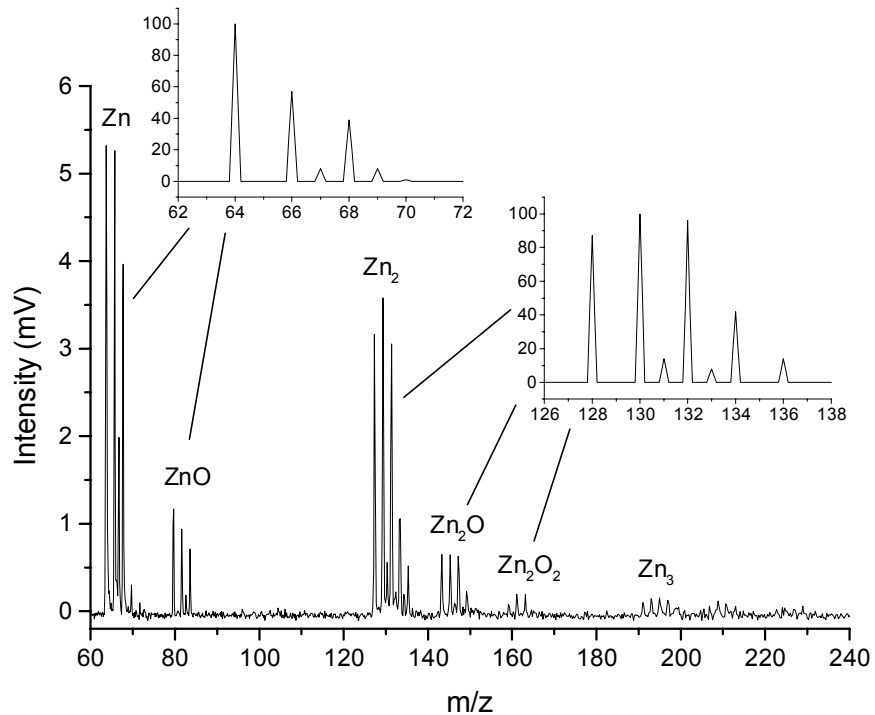


Figure 2.4 Mass spectrum resulting from LDI-TOFMS analysis of a pure zinc oxide pellet. The insets show the calculated isotope pattern of the Zn and Zn₂ series of ions. The respective oxides have similar isotopic distributions to the metal ion series.

Another fusion was conducted using yttrium oxide at a dopant concentration of 7.1 weight percent (5.6% Y) in Li₂B₄O₇. The resulting glass was transparent with no signs of particulates. Figure 2.5 shows the mass spectrum of this sample and it appears that yttrium is more easily detected than zinc. This spectrum is an average of 20 shots. The signal-to-noise ratio for the Y⁺ peak is 16 and there are few matrix peaks. The laser energy in this experiment was 220 μJ/pulse, and the repeller delay was optimized for this mass region at 17 μs. The reduced background signal is a result of the reduced laser energy required to obtain a good signal for Y⁺ and YO⁺, relative to the ZnO experiments. The ionization potential of yttrium (6.38 eV) is significantly less than that of zinc (9.39 eV) which may help explain these results.⁵⁰

Several different concentrations were tested in order to determine the detection limit of yttrium. The results from a glass containing 2.6% Y₂O₃ (2.0% Y) are shown in Figure 2.6. This spectrum is an average of 100 shots. The laser energy was 750

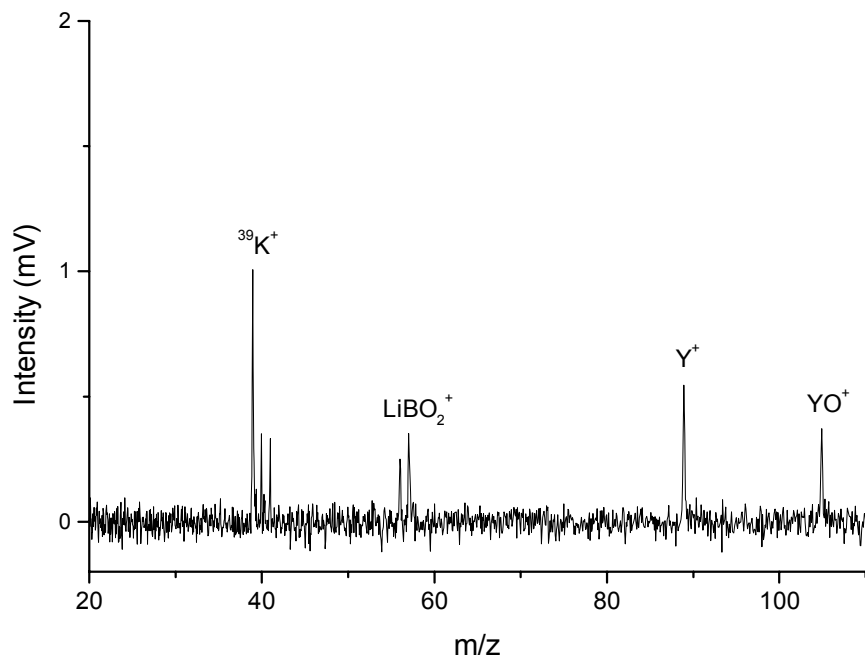


Figure 2.5 LDI-TOFMS results from analysis of a glass bead doped with 7.1% (w/w) yttrium oxide. The low intensity of the matrix peaks is due to the low laser energy necessary to obtain the Y^+ and YO^+ signals.

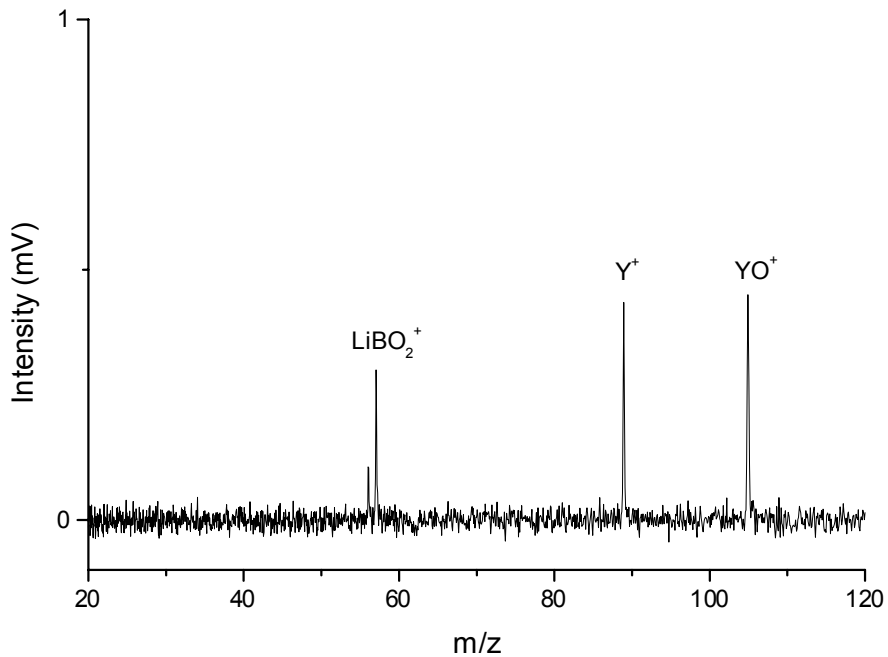


Figure 2.6 LDI-TOFMS results from analysis of a glass bead doped with 2.6% (w/w) yttrium oxide. The low intensity of the matrix peaks is due to the low laser energy necessary to obtain the Y^+ and YO^+ signals.

$\mu\text{J}/\text{pulse}$ and the repeller delay was set at $16\ \mu\text{s}$. The lower concentration of Y_2O_3 requires a significantly higher laser energy, however there is not a significant increase in the background signal. The broad, low-mass background signal due to metastable decay was higher. The signal stability for the Y_2O_3 doped sample was very good, allowing up to 1000 shots to be averaged. Another glass bead was prepared with a Y_2O_3 concentration of 300-ppm (250-ppm Y). The laser energy required to detect the yttrium and yttrium oxide peaks was $1\ \text{mJ}/\text{pulse}$, with the repeller delay set at 15 microseconds. Figure 2.7 shows intense background signals while the Y^+ and YO^+ peaks are barely visible with a S/N of 6 and 18, respectively. The limit of detection for yttrium oxide in the glass is estimated to be 150 ppm. This means that a “real” sample would have to contain at least 600 ppm Y_2O_3 , considering the dilution ratio of the sample in the flux is about 1:4. This is by no means trace-level detection.

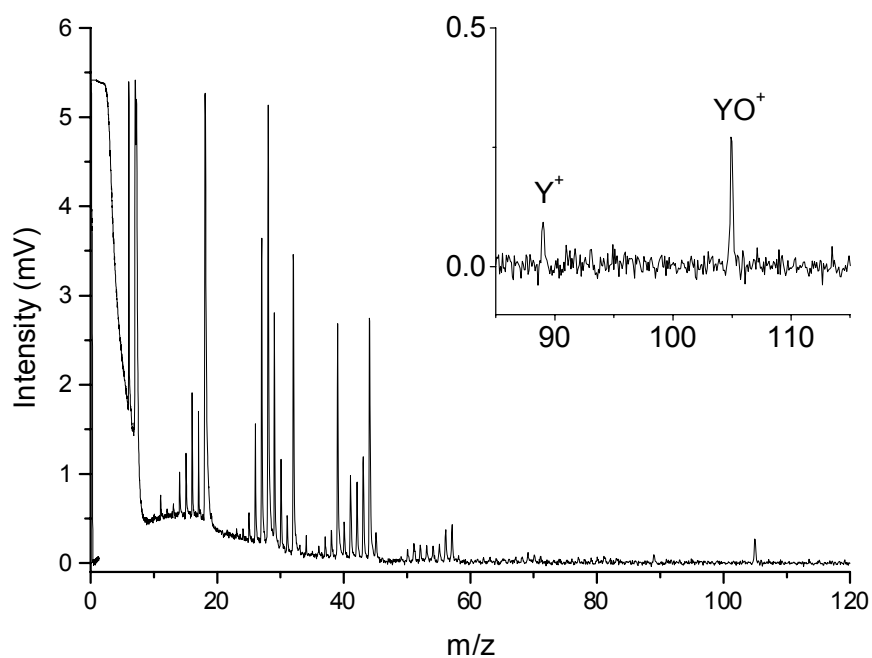


Figure 2.7 LDI-TOFMS results from analysis of a glass bead doped with 300 ppm yttrium oxide. The high intensity of the matrix peaks is due to the high laser energy necessary to obtain the Y^+ and YO^+ signals. The inset shows the relatively weak analyte ion signals. This concentration is near the detection limit.

Two different soil samples were studied by the fusion method. The first was the Virginia soil mentioned above. The soil was ground into a fine powder using a mortar and pestle. A glass bead was prepared using $\text{Li}_2\text{B}_4\text{O}_7$ as the flux with a soil concentration of 16% by weight. The resulting glass bead did have several particulates, but this was assumed to be alumino-silicate in nature. Figure 2.8 shows the LDI-TOFMS of glass beads with and without Virginia soil. The two spectra were collected under identical instrument conditions. The laser energy in each case was $400 \mu\text{J}/\text{pulse}$ and the repeller delay was set at $20 \mu\text{s}$. The peaks seen in the inset of Figure 2.8 have never been observed in the blank samples. The masses of several of these peaks match those of FeO ($^{56}\text{FeO} = 72 \text{ Da}$, $^{57}\text{FeO} = 73 \text{ Da}$) and FeO_2 ($^{56}\text{FeO}_2 = 88 \text{ Da}$, $^{57}\text{FeO}_2 = 89 \text{ Da}$). However, the isotope ratio of the observed peaks, $^{56}\text{Fe}:^{57}\text{Fe} = 0.45$, does not match the expected value of $^{56}\text{Fe}:^{57}\text{Fe} = 43$. The observed isotopic distributions are usually within 10% of the calculated distribution. This result suggests that the observed

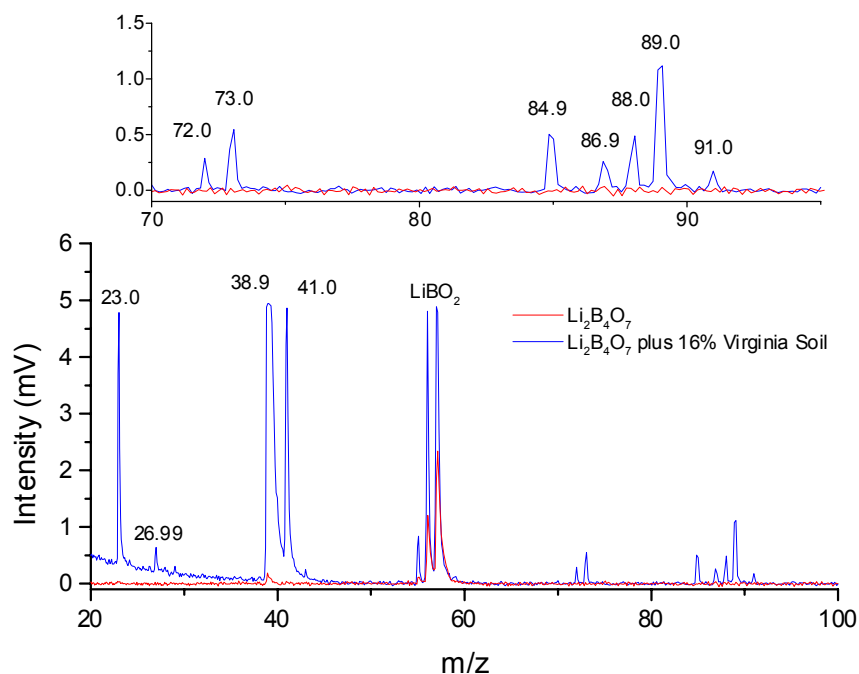


Figure 2.8 LDI-TOFMS of a glass bead containing 16% (w/w) Virginia soil. The spectrum shows the presence of new peaks in the 70-95 Da range as well as the large increase in signal intensity for Na and K (23 and 39/41 Da, respectively). The upper inset is an expansion of the 70-95 Da region. See text for peak assignments.

peaks are not iron oxides. While it is not clear whether these peaks represent FeO and FeO₂ they do appear to be metal oxides, due to the difference of 16 Da. It is not likely that these peaks are multiple metal clusters or multiply charged ions because of the 1 Da difference. Due to the relatively high concentration of iron in this soil, as determined by FAAS, it would seem likely that these peaks are iron oxides, but the peak identities are uncertain because the observed isotopic patterns do not match the expected distributions.

The peak at 84.9 Da does not match the mass of an expected metal oxide (i.e. magnesium oxide, manganese oxide, etc.). Mass alone is not sufficient information to assign this peak. The peak at 86.9 Da could be MnO₂, but it is difficult to assess the presence of Mn because of the overlapping matrix signal at 55 Da. This illustrates the difficulty of identifying metals by the observation of oxide and/or cluster ions. It is far easier to identify the reduced metal ion. In this case identification is difficult due to overlapping matrix peaks.

Although sodium and potassium are commonly observed in the background signal, there is a dramatic increase in signal intensity in the spectrum of the soil sample. Other matrix signals, such as the LiBO₂ peaks, show a relative intensity change of about 4. The much larger change in relative intensity for sodium and potassium suggests that these elements have a much higher concentration in the glass bead containing the soil. Sodium and potassium are common elements found in soil and are also easily ionized. A peak at 27 Da, which is indicative of aluminum, is also detected in the mass spectrum of the soil sample.

The second soil sample is a NIST standard reference material (SRM # 2709) which came from the San Joaquin Valley in California. As outlined in the certificate of analysis, Table 2.3 shows the concentration of various elements in the soil.⁵¹

Another glass bead was prepared using a 1:1 mixture of LiBO₂ and Li₂B₄O₇ and 20% (w/w) SRM 2709. After fusion, no particulates could be seen in the glass. Figure 2.9 shows the LDI-TOFMS results obtained at two different repeller delays. The spectra in Figure 2.9 are an average of 25 single-shot spectra collected using a laser pulse energy of 300 μJ/pulse and a repeller delay of 10 μs, which is the optimum delay for the mass range shown. The blank has the same flux composition as the bead with the

Table 2.3 A list of elements and their certified concentration in the NIST soil sample (SRM 2709).

Element	Concentration
Aluminum	7.50 %
Iron	3.50 %
Potassium	2.03 %
Calcium	1.89 %
Magnesium	1.51 %
Sodium	1.16 %
Titanium	0.342 %
Barium	968 ppm
Manganese	538 ppm
Strontium	231 ppm
Chromium	130 ppm

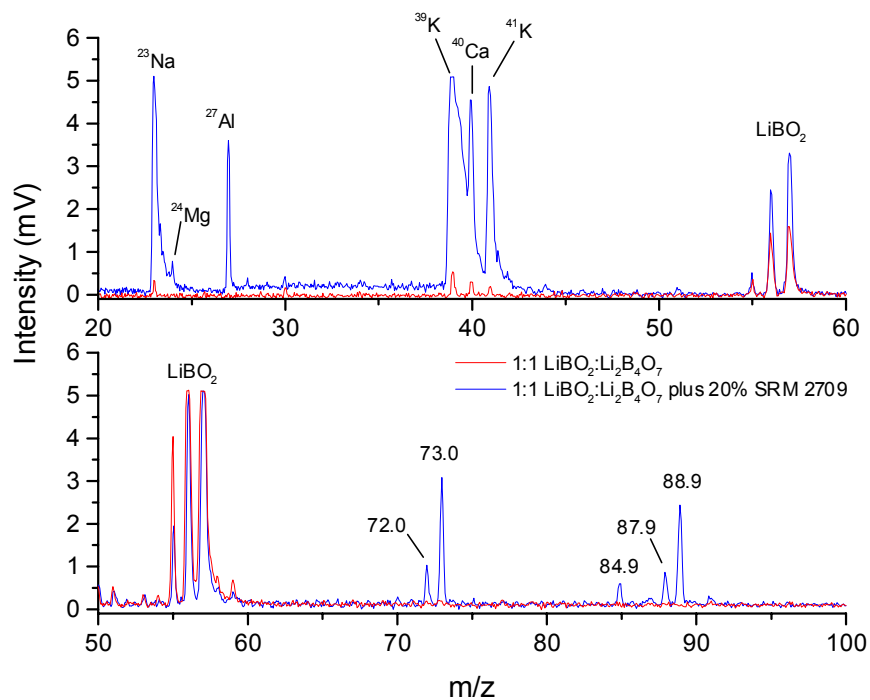


Figure 2.9 LDI-TOFMS analysis of the glass bead containing 20% (w/w) SRM 2709. The upper spectrum shows the drastic increase in Na and K as well as the appearance of Mg and Al. The lower spectrum is very similar to the spectrum obtained for the Virginia soil. See text for peak assignments.

dissolved soil. Similar to the results for the Virginia soil, there is a drastic difference in the relative intensity of Na and K with a much smaller relative intensity change for the LiBO_2 peaks. In addition, there are peaks that identify Mg and Al. The bottom spectra were collected using a laser pulse energy of $700 \mu\text{J}/\text{pulse}$ and a repeller delay of $20 \mu\text{s}$. Again, the long delay reduces the broad background signal at higher laser energies. The spectrum of the bead with the dissolved soil is almost identical to the one seen in Figure 2.8. The same peak assignments are assumed for this sample. There were no peaks detected at higher mass (using delay times of up to $40 \mu\text{s}$) for either soil sample.

2.5 Conclusions

The fusion method using lithium borates is not an effective sample preparation technique for the positive-ion LDI-TOFMS analysis of trace elements. In most cases, a concentration of several weight percent was required in order to obtain a significant ion signal. The matrix background signal in most cases was intense and contained ion signals that overlap with ions of interest.

It is assumed that ionization in the laser-induced plasma is a competitive process. Table 2.4 shows the ionization potential for the elements that are in several of the samples discussed in the previous section. The high concentrations of lithium combined with the relatively low ionization potential of this element are believed to suppress ionization of the elements of interest. Many of the spectra recorded showed saturated signals for lithium ions, small mass clusters, and other alkali metal ions, mainly sodium and potassium. A flux containing elements with higher ionization potentials, such as boro-silicate compounds, may help decrease the limit of detection.

Quantification using LDI-TOFMS is difficult. The signal intensity of an ion varies substantially due to shot-to-shot fluctuations in laser intensity. Comparisons of averaged spectra (50-100 shots) from the same sample also reveal significant differences in signal intensity. The advantage of a homogeneous sample is nullified by the fluctuation in signal intensity. The difficulties in quantification of elements, in addition to the high limit of detection, suggest that LDI-TOFMS is not as beneficial as well established analytical techniques such as XRF spectroscopy and ICP-MS.

Table 2.4 A list of the ionization potential for the elements considered in this study.

Element	Ionization Potential (eV)
Lithium	5.39
Yttrium	6.38
Zinc	9.39
Aluminum	5.99
Iron	7.87
Potassium	4.34
Calcium	6.11
Magnesium	7.65
Sodium	5.14
Titanium	6.82
Barium	5.21
Manganese	7.44

The fusion technique has been used to prepare samples for analysis by laser ablation ICP-MS.^{52,53,54} Perkins, et al. have successfully used this method of analysis for quantitative trace and ultra-trace detection of elements in silicates.⁵³ The detection limits were found to be better than those obtained using XRF spectroscopy. The success of ICP-MS analysis, when compared to the method presented here, is a result of the high ionization efficiency provided by the inductively coupled plasma versus the low ionization efficiency observed using direct ablation/ionization.

Chapter 3 – Characterization of Inorganic Coordination Complexes by LDI- and MALDI-TOFMS

3.1 Introduction

The coupling of different types of metal complexes with varied chemical properties has led to the construction of interesting supramolecular species. These high molecular weight complexes generally contain multiple metal centers (homo- and heteronuclear) with a variety of multidentate polypyridyl ligands. Such polymetallic coordination complexes are under investigation as sensitizers for solar-energy conversion,^{55,56,57} photocatalysts,⁵⁸ selective “light-activated anticancer drugs,”⁵⁵ and a variety of other molecular devices.⁵⁹ The general molecular design of these inorganic assemblies consists of light-absorbing units, central electron-collecting units, and bridges between the units.⁶⁰

Typical structural characterization methods for multimetallic coordination complexes include NMR spectroscopy, electrochemistry, X-ray crystallography, and UV/Vis spectrophotometry. Unfortunately, suitable crystals are not always obtainable for X-ray analysis. NMR spectra are usually complex due to the large number of aromatic protons on the polypyridyl ligands and the occurrence of multiple diastereoisomers. NMR signals also often suffer from paramagnetic effects.⁵⁷ The structural information obtained from electrochemistry and UV/Vis spectroscopy can be ambiguous. For these reasons, there is interest in finding a more universal method to characterize the structure and purity of supramolecular assemblies.

Mass spectrometry should be an effective tool for the structural analysis of inorganic coordination complexes, however, the low volatility, sensitivity, and lability of these species have made MS characterization problematic. Significant advances have been made with fast-atom bombardment^{61,62,63,64} and electrospray-ionization mass spectrometry,^{65,66,67,68,69,70} although these techniques still have limitations. FAB-MS has been successful for monometallic and small polymetallic compounds, but fragmentation often causes a low intensity or complete absence of the molecular ion.^{71,72,73} The limited choice of matrices for FAB-MS also creates problems with the solubility of coordination complexes. ESI-MS also requires the complex to be soluble and chemically stable in a

suitable ESI solvent. Furthermore, the electrospray interface can generate interference by forming new species during ionization.^{56,72,74}

Little work has been published on laser-based mass spectrometric methods for structural characterization of inorganic complexes. With its high mass range of greater than 1×10^6 Da⁷ and adjustable laser desorption energies, matrix-assisted laser desorption/ionization time-of-flight mass spectrometry seems well suited for the analysis of large inorganic complexes. By analogy to MALDI-TOFMS of polar, easily fragmented proteins, MALDI should be useful for the analysis of fragile inorganic complexes.

Typically, ultraviolet MALDI requires a matrix compound that absorbs the laser radiation directly, usually an organic acid, and an analyte that does not. Ionization of the analyte is achieved by protonation or electron abstraction by the matrix in the gas-phase. There is also the possibility of detecting pre-formed ions, as discussed in Section 1.4.2. UV MALDI of inorganic complexes is complicated by the fact that most of these analyte molecules also have strong absorption bands in the UV. Some portion of the laser radiation is absorbed by the analyte, leading to a spectrum that resembles both hard (direct LDI) and soft (MALDI) ionization techniques.

Although several researchers report using MALDI-TOFMS for structural analysis of similar polymetallic species, such as metallodendrimers^{75,76,77,78} and metal clusters,^{79,80} to our knowledge there have been no systematic investigations of experimental conditions reported for MALDI analysis of metal-polypyridyl complexes. This chapter presents results from a systematic investigation of different matrices, sample concentrations, and instrument conditions for the MALDI-TOFMS analysis of the four inorganic coordination complexes shown in Figure 3.1. These results demonstrate some of the experimental considerations of using MALDI-TOFMS for the structural characterization of this class of compounds.

3.2 Experimental Details

3.2.1 Chemicals

The inorganic coordination complexes were synthesized and purified by Karen Brewer's research group at Virginia Polytechnic Institute and State University.^{81,82,83} Sinapinic acid, 2,5-dihydroxybenzoic acid, 3,4-dihydroxycinnamic acid, dithranol, 6-aza-

2-thiothymine, meta-dinitrobenzene, 3,5-dinitrobenzoic acid, and 9-anthracenecarboxylic acid were purchased from Aldrich and used without further purification. α -cyano-4-hydroxycinnamic acid was also purchased from Aldrich, but was further purified by re-crystallizing several times in ethanol. All solvents were HPLC grade.

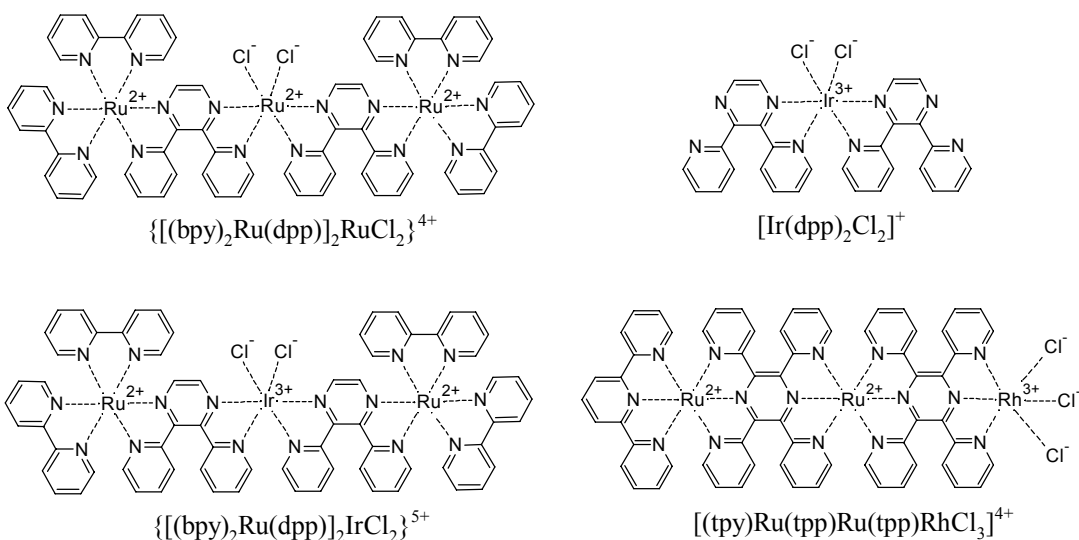


Figure 3.1 2-dimensional representation of the chemical structure of the inorganic coordination complexes investigated.

3.2.2 Sample Preparation

Sinapinic acid and α -cyano-4-hydroxycinnamic acid were prepared as saturated solutions in 9:1 acetonitrile/water (v/v). 3,4-dihydroxycinnamic acid, 9-anthracenecarboxylic acid, dithranol, and 6-aza-2-thiothymine were prepared as saturated solutions in acetonitrile. 3,5-dinitrobenzoic acid, and meta-nitrobenzene were prepared as ~20 mg/mL solutions in acetonitrile, and 2,5-dihydroxybenzoic acid was prepared as ~20 mg/mL solution in 9:1 acetonitrile/water (v/v). A fresh matrix solution was prepared daily because these compounds undergo chemical degradation in solution, which reduces their effectiveness in the ionization process. Solutions of the inorganic complexes were prepared weekly at a concentration of 1.0 mg/mL in acetonitrile. The solutions for the concentration dependence study were made by diluting the 1.0 mg/mL solutions of the inorganic complexes in acetonitrile to make final

concentrations of 0.5, 0.25, 0.1, and 0.05 mg/mL. These concentrations correspond to a molar matrix-to-analyte ratio ranging from 200:1 to 5000:1. 10 μ L of matrix solution and 10 μ L of inorganic complex were combined in an Eppendorf tube and vortexed for 20-30 seconds to ensure complete mixing. A 1-2 μ L aliquot of this mixture was placed on the MALDI sample plate and dried under a gentle stream of nitrogen.

Samples prepared for analysis on the Comstock LI RTOF/210 were recrystallized using 0.5 μ L of HPLC grade methanol. As shown in Figure 1.11, on a polished aluminum surface recrystallization results in a smaller more homogeneous crystal distribution and thus leads to better shot-to-shot reproducibility. However, recrystallization requires that all components in the sample are soluble in the chosen solvent. This method may not be applicable to all matrix/analyte combinations. Sample preparations for analysis on the Kratos Kompact SEQ did not require this recrystallization step due to the nature of the sample probe's surface. The sample wells were chemically etched into a stainless steel plate, which gives them a rough surface. The large number of surface defects result in formation of more seed crystals during evaporation and therefore smaller crystals upon complete dryness.

3.2.3 Mass Spectrometric Analysis

Initial experiments with direct LDI and MADLI-TOF-MS were performed on the Comstock reflectron time-of-flight mass spectrometer (model LI RTOF/210) using the 355-nm output of a Nd:YAG laser (Continuum Surelite II).²³ Experiments using this mass spectrometer were also performed using the 337-nm output of a nitrogen laser (Photon Technologies International GL3300). Results were similar using either laser.

As discussed in Chapter 1, samples are held in a perpendicular geometry in the LI RTOF/210. Because ions created by MALDI have similar initial velocity distributions the repeller delay has a lesser effect. Contrary to the results presented in section 2.4.2 where the repeller delay could be used to reduce matrix interference, there is little advantage with longer delay times in MALDI. Therefore, the sample probe was modified to reduce the distance between the flight axis and the sample (relative to experiments in Chapter 2) in order to minimize in-source fragmentation reactions. A schematic of the

modified probe is provided in Figure 3.2. A typical delay time for this sample position is 7 μ s.

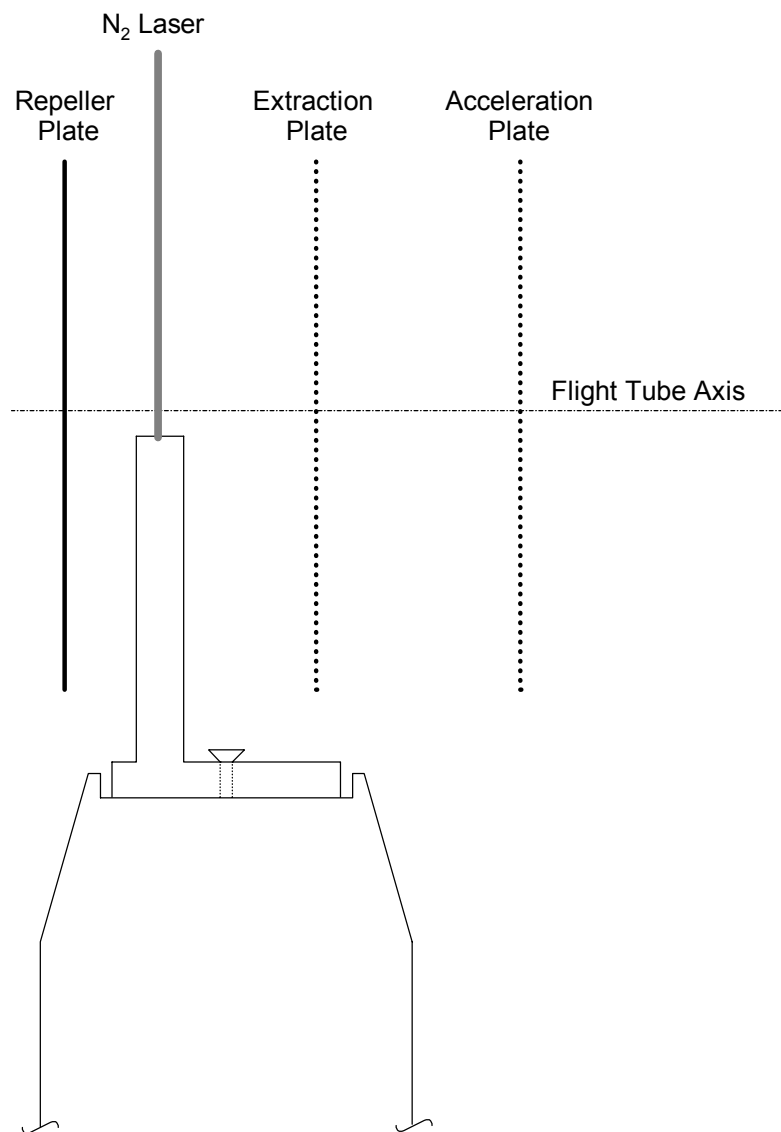


Figure 3.2 Schematic showing aluminum probe extension. The sample is typically held 7 mm below the flight axis.

Subsequent experiments were performed on a Kratos Kompact SEQ TOF-MS that uses a nitrogen laser (337 nm) for desorption/ionization and a discrete-dynode electron multiplier for ion detection. Delayed extraction was used to improve resolution and the delay time was set to optimize the mass region of the molecular ion. Delay times using this instrument are on the order of several hundred nanoseconds. Although the instrument is equipped with a reflectron, all spectra were collected in linear mode

due to superior resolution. Both positive and negative-ion modes were investigated, but no results were obtained in the negative-ion mode. Acceleration potentials of 5 kV and 24 kV were investigated. Results using the 5 kV acceleration potential were similar to those obtained with the Comstock LI RTOF/210. Higher acceleration potentials produced more efficient detection of the higher mass fragments ($[M-n(\text{PF}_6)]^+$), as will be discussed in Section 3.3.1.

For both instruments, 50-100 laser shots were averaged to obtain an averaged mass spectrum. The laser energy was adjusted to optimize the signal-to-noise ratio and resolution, and was typically just above the threshold for ionization. Observed threshold energies for each matrix are shown in Table 3.1. The reported energies are relative values, absolute numbers are not known. Laser energies significantly above threshold decrease resolution due to larger initial kinetic energy distributions. However, threshold energies tend to produce fewer ion signals, leading to less structural information. Therefore, a compromise between signal quality (resolution and S/N) and structural information was found by adjusting the laser energy. Mass spectra were typically calibrated using the Na^+ peak and several of the known matrix peaks. Mass accuracy was typically 0.1 % or better. Mass accuracy in this study is limited by the inability to resolve the complex isotopic distributions of the high-mass peaks, leading to variability in the peak apex from shot-to-shot and lower mass accuracy.

Table 3.1 Laser desorption/ionization threshold energies for all of the matrices studied.

Matrix	DHB	SA	HCCA	DHC	DNBA	mDNB	dithranol	ATT
Threshold Energy	75	75	45	55	100	55	55	65

3.3 Results and Discussion

3.3.1 Acceleration Potential and Resolution

MALDI mass spectra of the monometallic complex were similar using either high or low acceleration potential, as shown in Figure 3.3. Furthermore, the pseudomolecular ion (PM^+ , the complex with no counter ion) at $m/z = 731$ was observed for both acceleration potentials with MALDI and direct LDI. As reported by R. C.

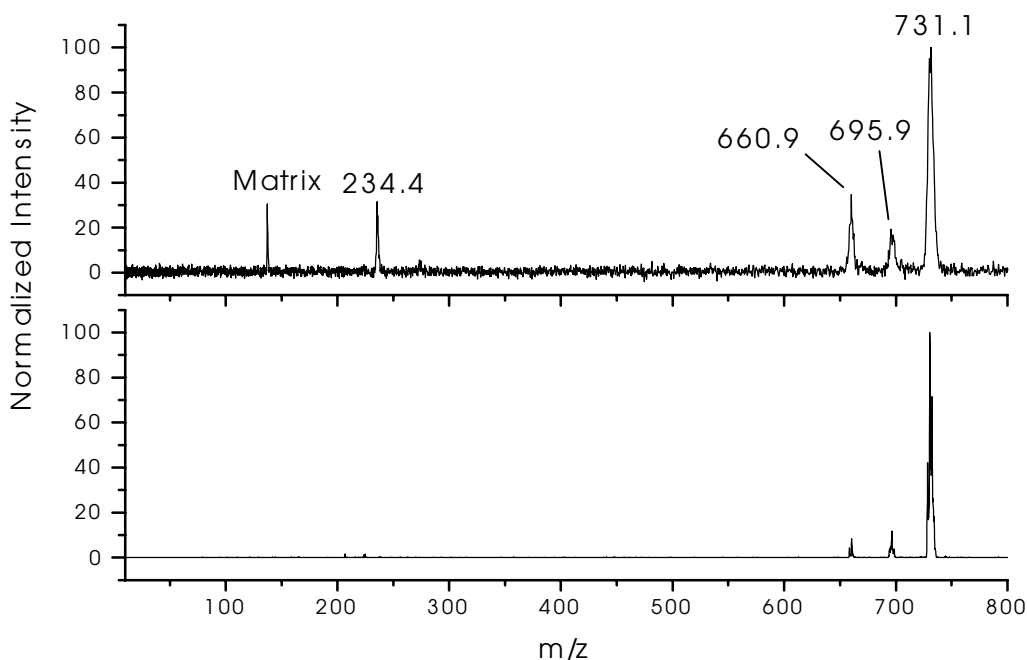


Figure 3.3 MALDI mass spectra of $[\text{Ir}(\text{dpp})_2\text{Cl}_2]^+$ on two different instruments. The pseudomolecular ion is seen in both cases (731), along with peaks that show the loss of each Cl (696, 661). The top spectrum was collected using the Comstock LI/RTOF 210 with an acceleration potential of -2.3 kV. The bottom spectrum was collected on the Kratos Kompact SEQ with an acceleration potential of 24 kV.

Watson²³ and confirmed here, MALDI-TOFMS analysis of the trimetallic complexes using the Comstock LI RTOF/210 (acceleration potential = -2.3 kV), did not result in detection of the PM^+ or any multiple-metal fragments. MALDI mass spectra collected using low acceleration potentials showed less fragmentation in the lower mass region (<1000 Da), but were generally similar to those observed with direct LDI at high acceleration potential. Figure 3.4 illustrates this point for the $\{[(\text{bpy})_2\text{Ru}(\text{dpp})]_2\text{RuCl}_2\}(\text{PF}_6)_4$ complex. At the top is a direct LDI spectrum recorded on the Kratos Kompact SEQ with a high acceleration potential (24 kV). The bottom shows the MALDI spectrum, with DHB as the matrix, acquired on the Comstock LI/RTOF 210 with a low acceleration potential. In both cases no ions were detected above the m/z range shown. A majority of the experiments on the trimetallic complexes using the Comstock instrument were performed by R. C. Watson.²³ I found that MALDI

experiments with the Kratos Kompact SEQ using the low acceleration potential (5 kV) resulted in similar findings.

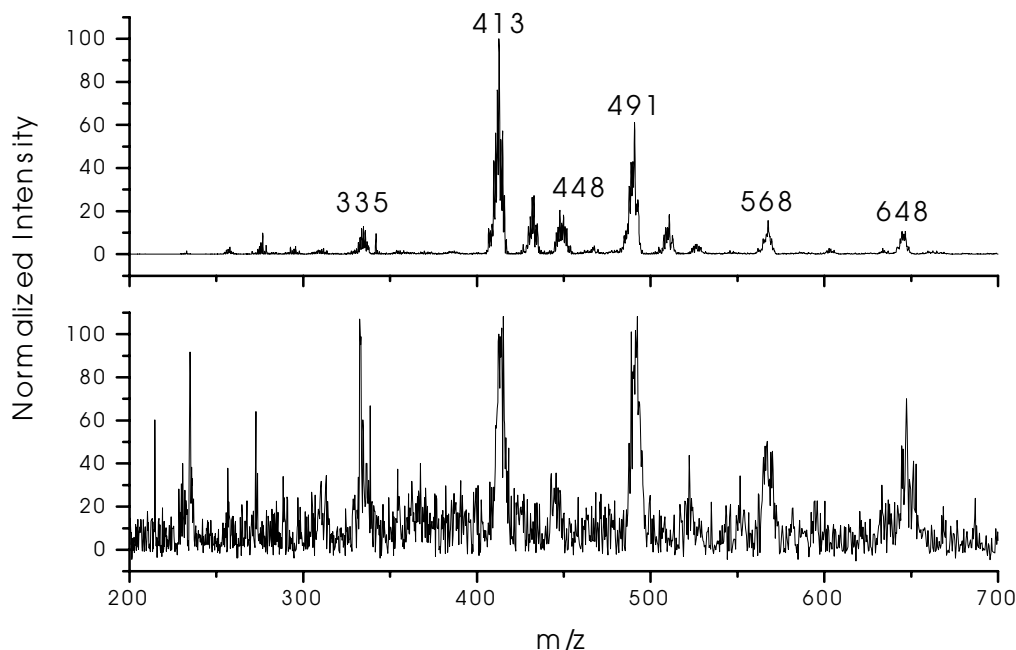


Figure 3.4 Comparison of mass spectra of $\{[(bpy)_2Ru(dpp)]_2RuCl_2\}(PF_6)_4$ using different acceleration potentials. The top spectrum is the result of direct LDI on the Kratos Kompact SEQ with a 24 kV acceleration potential. The bottom spectrum is the result of MALDI analysis on the Comstock LI/RTOF 210 with an acceleration potential of -2.3 kV. The lower acceleration potential decreases the resolution to the extent that the MALDI spectrum is very similar to the direct LDI spectrum, and no high-mass peaks are observed.

MALDI-TOFMS experiments were performed using the Kratos Kompact SEQ with a high acceleration potential (24 kV). These experiments showed a series of peaks due to the molecular ion with varying degrees of counterion loss ($[M-n(PF_6)]^+$) for all multimetallic complexes investigated. I conclude that the absence of high mass peaks using low acceleration potentials is due primarily to poor resolution and/or detection efficiency rather than to a lack of complex stability. As discussed in Chapter 1, several reports have shown that resolution is greatly improved when higher acceleration potentials are applied in the ion source region.^{8,9} Higher acceleration potentials result in the initial kinetic energy distribution composing a smaller portion of the total energy of the ions, which correlates directly with mass resolution. The efficiency of electron

multipliers and micro-channel plate detectors also increases with higher ion impact velocity (see Section 1.1.1).

3.3.2 Direct Laser Desorption/Ionization

All of the complexes were investigated by direct LDI-TOFMS on the Kratos Kompact SEQ with the high acceleration potential. As shown in Figure 3.5, no peaks greater than 900 Da were observed for any of the compounds. The mass spectrum of the monometallic complex showed the following ion signals: $[\text{Ir}(\text{dpp})_2\text{Cl}_2]^+$ (732 Da), $[\text{Ir}(\text{dpp})_2\text{Cl}]^+$ (696 Da), $[\text{Ir}(\text{dpp})_2]^+$ (660 Da), and dpp^+ (234 Da). The relative simplicity of this spectrum was not surprising, but it does show the lability of the Ir-Cl bond in the monometallic compound. It was somewhat surprising that no signal was observed for the $[\text{Ir}(\text{dpp})]^+$ ion fragment.

No multimetallic fragments were observed for the trimetallic complexes with direct LDI. The mass spectra of $\{[(\text{bpy})_2\text{Ru}(\text{dpp})]_2\text{RuCl}_2\}(\text{PF}_6)_4$ and $\{[(\text{bpy})_2\text{Ru}(\text{dpp})]_2\text{IrCl}_2\}(\text{PF}_6)_5$ showed many of the same fragment ions. The most intense ion peak in both spectra was $[(\text{bpy})_2\text{Ru}]^+$ (413 Da). Other ion signals common to both compounds were $[\text{Ru}(\text{dpp})]^+$ (334 Da), $[(\text{bpy})_2\text{RuCl}]^+$ (448 Da), $[(\text{bpy})\text{Ru}(\text{dpp})]^+$ (491 Da), and $[(\text{bpy})_2\text{Ru}(\text{dpp})]^+$ (648 Da). However, the relative intensities of these fragment ion signals were different for each compound. Ru-ligand fragment ions were observed for both compounds, but there were no fragment ions containing Ir. This observation was confirmed by both mass and isotope pattern. The isotope pattern of Ru-containing ions is dramatically different from that of Ir-containing ions due to the relative number of isotopes for each metal. Isotope patterns were also used to confirm that no multiply charged ions were detected. The m/z difference between ions in the isotope pattern varies depending on the charge state of the ion; 1.0 Da for singly charged ions, 0.5 Da for doubly charged ions, 0.33 Da for triply charged ions, and so on.

Similarly, the direct LDI mass spectrum of $[(\text{tpy})\text{Ru}(\text{tpp})\text{Ru}(\text{tpp})\text{RhCl}_3](\text{PF}_6)_4$ did not show multimetallic fragment ions. The largest ions signals in the mass spectrum were $[\text{Ru}(\text{tpp})_2]^+$ (877 Da), $[(\text{tpy})\text{Ru}(\text{tpp})]^+$ (721 Da), $[(\text{tpp})\text{RuCl}]^+$ (525 Da), $[\text{Ru}(\text{tpp})]^+$ (489 Da), and $[(\text{tpy})\text{RuCl}]^+$ (370 Da). No Rh-containing fragment ions were detected. Although the atomic mass of Rh falls within the range of the Ru isotope masses, peak

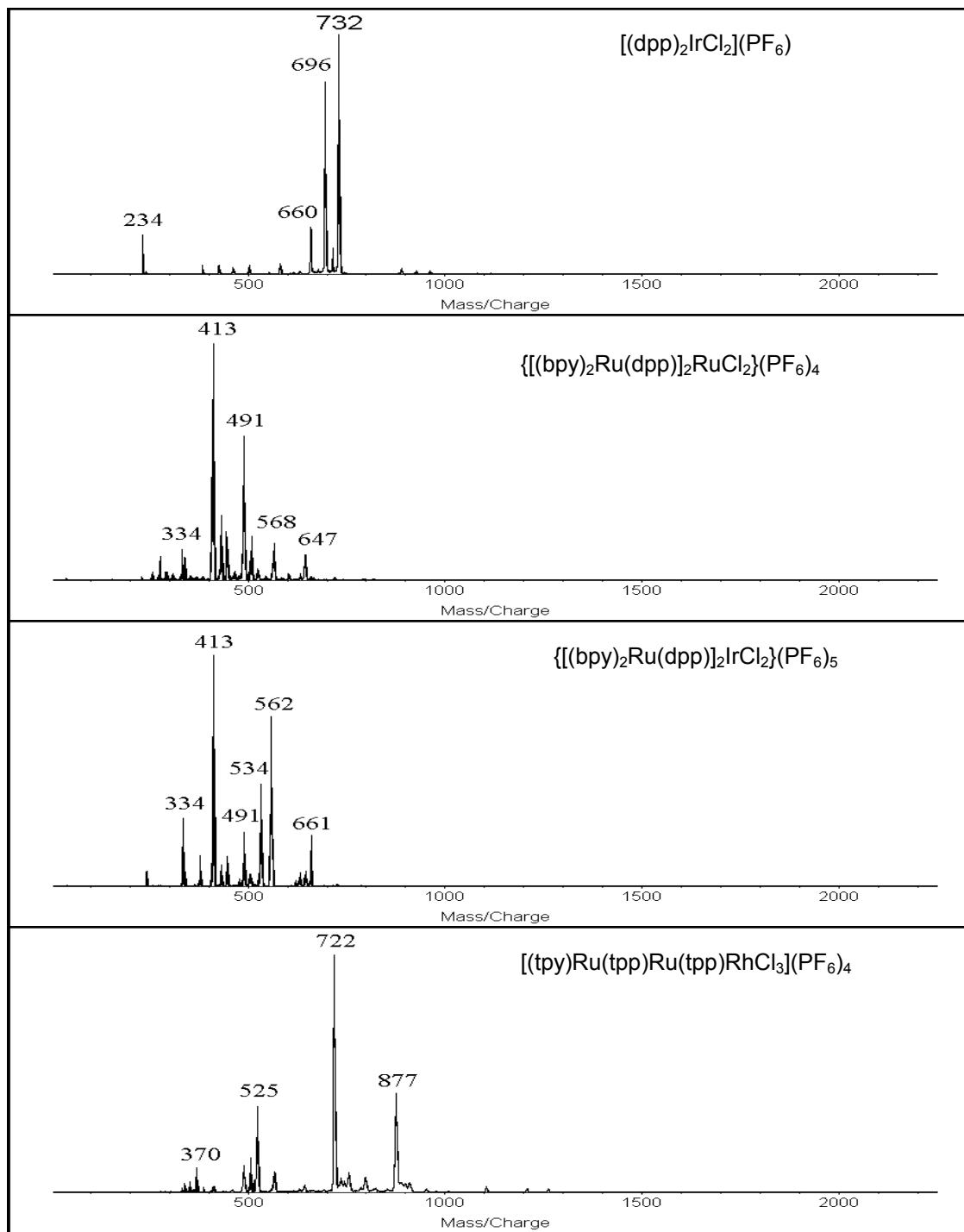


Figure 3.5 Direct laser desorption/ionization mass spectra of the inorganic coordination complexes. Spectra were recorded on the Kratos Kompact SEQ with a 24 kV acceleration potential. Note that no high-mass peaks are observed.

assignment of the fragment ions is straightforward because the single isotope of Rh produces fewer peaks than do ions containing Ru. Figure 3.6 demonstrates the difference in isotopic distributions of Rh- and Ru-containing ion fragments. The $(\text{tpp})\text{RhCl}^+$ and $(\text{tpp})\text{RuCl}^+$ ions only differ in mass (average mass) by 1.8 Da. However, as shown in the upper two spectra, the peak distributions differ substantially. These peak distributions were calculated using an isotopic distribution calculator⁸⁴ and the results were plotted in Excel. The peak in the experimentally observed spectrum (bottom) with its apex at $m/z = 525$ clearly matches the isotopic pattern for the Ru-containing fragment. All peaks in the LDI spectrum were analyzed with regards to their isotopic patterns.

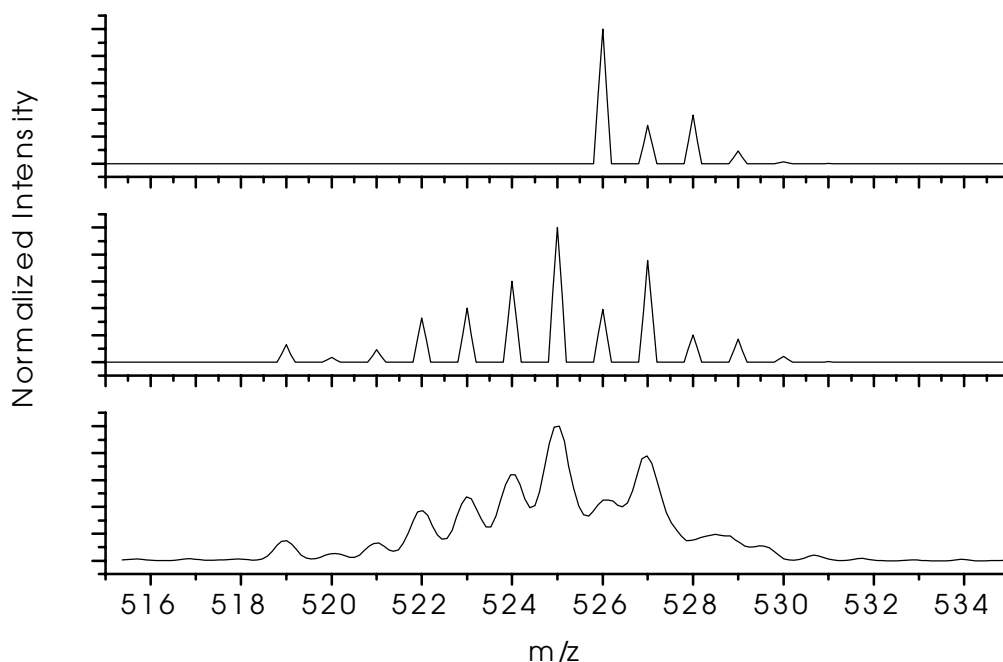


Figure 3.6 Comparison of isotope patterns for the peak at $m/z = 525$ in the direct LDI mass spectrum of $[(\text{tpy})\text{Ru}(\text{tpp})\text{Ru}(\text{tpp})\text{RhCl}_3]^{4+}$. The top spectrum is a theoretical isotope pattern for the fragment ion $(\text{tpp})\text{RhCl}^+$, the middle spectrum is a theoretical isotope pattern for the fragment ion $(\text{tpp})\text{RuCl}^+$, and the bottom spectrum is the experimentally observed isotope distribution. This strategy is used to help identify fragment ions.

The observation of Ru-Cl ion fragments indicates that there are gas-phase reactions or rearrangements occurring in the ion source. This behavior is seen with all

of the trimetallic complexes during direct LDI studies. We did not attempt to identify all of the product ions observed in the mass spectra because insufficient data is available for definitive assignments. The extra product ions make interpretation of the spectra, and therefore characterization of the trimetallic complexes, more difficult.

3.3.3 MALDI-TOFMS

The spectrum resulting from MALDI analysis of the monometallic complex was similar to the direct LDI spectrum, but with the addition of the matrix peaks. The relative peak intensities were different in the MALDI spectrum but the three major peaks ($[\text{PM-2Cl}]^+$, $[\text{PM-Cl}]^+$, and PM^+) were the same. For the direct LDI analysis the peak ratios were 2:8:10 ($[\text{PM-2Cl}]^+:[\text{PM-Cl}]^+:\text{PM}^+$), while MALDI analysis resulted in less fragmentation with peak ratios of 1:1:10, reflecting the soft ionization of MALDI.

Analysis of the trimetallic complexes using MALDI-TOF-MS showed a decrease in the number of monometallic fragment ions compared to direct LDI-MS. The intensity of the monometallic fragment peaks depended on the matrix-to-analyte ratio (discussed in detail in section 3.3.5). Figure 3.7 shows typical MALDI mass spectra of the trimetallic complexes and further illustrates the soft ionization achieved with MALDI. Peaks with a m/z less than approximately 480 are attributed to the matrix. The major high-mass peaks in each spectrum correspond to the molecular ion with varying degrees of PF_6^- loss $[\text{M-n}(\text{PF}_6)]^+$. The molecular ion is not observed in the MALDI analysis of any of the multimetallic complexes. The highest m/z peaks in the spectra for the Ru-Ru-Ru and Ru-Ir-Ru complexes (2058 and 2148 Da, respectively) do not match any of the expected mass fragments in the $[\text{M-n}(\text{PF}_6)]^+$ series. These peaks are probably the result of gas-phase rearrangements and/or matrix adducts. I did not attempt to make assignments for these peaks, as the mass alone is insufficient data to determine exact composition at this resolution.

The series of ions $[\text{M-n}(\text{PF}_6)]^+$ were all observed as singly charged species, and no multiply charged fragments were detected in any of the mass spectra. Although not fully expected, this behavior has been observed in MALDI analysis of metallodendrimers⁷⁵ and similar metal-polypyridyl systems.⁸⁵ Bodige, et al.⁷⁵ postulated that the observed ions were a result of protonated, fully reduced metal complexes with

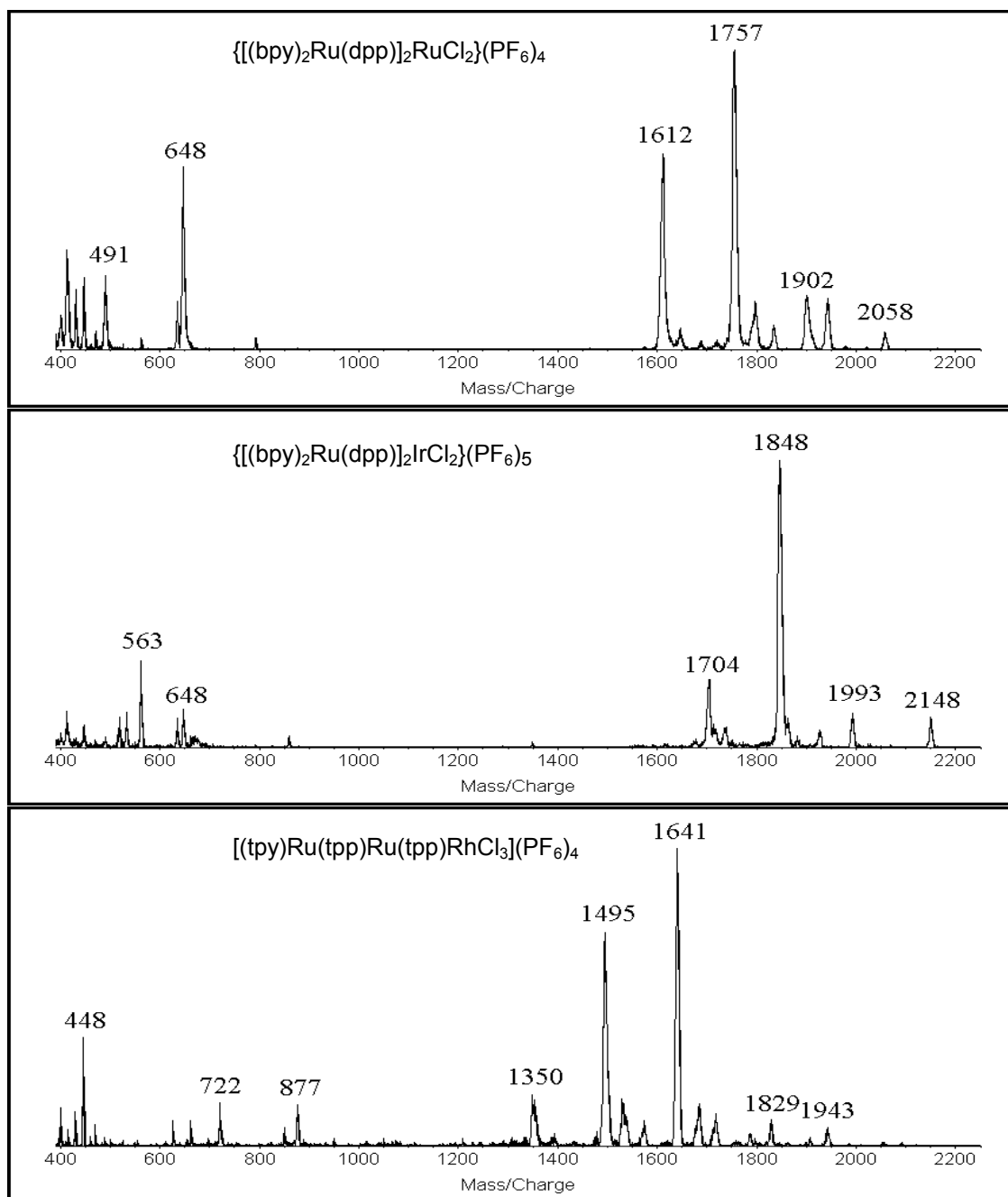


Figure 3.7 MALDI-TOF mass spectra of trimetallic complexes using the Kratos Kompact SEQ with an acceleration potential of 24 kV. Each complex shows a series of $[M-n(PF_6)]^+$ ions as well as some monometallic fragments in the lower mass region. The matrix compound used to collect these spectra sinapinic acid with a matrix-to-analyte ratio of about 500:1.

varying retention of PF_6^- counterions. Mass accuracy was not sufficient in our experiments to determine if the $[\text{M}-n(\text{PF}_6)]^+$ ions were protonated or radicals. However, using DHB as the matrix produced numerous matrix adducts in the spectra. In fact, most of the matrices that we investigated produced a small degree of adduction as evidenced by low-intensity peaks that did not match rational fragmentation patterns. Although not conclusive evidence, the presence of adducts suggests that the $[\text{M}-n(\text{PF}_6)]^+$ ions are not radicals.

In Table 3.2, the $[\text{M}-n(\text{PF}_6)]^+$ pattern for the Ru-Ru-Ru and the Ru-Ir-Ru complexes are similar in that neither complex loses Cl. In contrast, the Ru-Ru-Rh complex shows an $[\text{M}-2\text{Cl}-n(\text{PF}_6)]^+$ fragmentation pattern. Further interpretation of these results reveals some interesting trends. Bridgewater, et al.⁸¹ studied the UV/Vis spectroscopy and electrochemistry of the Ru-Ru-Ru and Ru-Ir-Ru complexes. The results of the electrochemical experiments are summarized in Table 3.3. These complexes exhibit one reversible oxidation (metal-based) and seven reversible reductions (ligand-based) in solution. It is also observed that the Ru-Ir-Ru complex has bridging ligand reductions that occur at more positive potentials (are more easily reduced) than the Ru-Ru-Ru complex. Assuming the complexes are fully reduced in the gas-phase MALDI plume, the series of ions produced in the Ru-Ir-Ru complex are of a more reduced nature than those observed for the Ru-Ru-Ru complex, and thus follow the same trend as observed in the solution-phase electrochemistry. For example, assuming the ions are protonated, the peak at $m/z = 1704$ in the spectrum of the Ru-Ir-Ru complex corresponds to a four-electron reduction, whereas the most-reduced species observed in the spectrum of the Ru-Ru-Ru complex is the three-electron reduction product at $m/z = 1612$.

The observed fragment ions for the Ru-Ru-Rh complex consistently show the loss of two chloride ions as well as varying degrees of PF_6^- loss (see Table 3.2). The solution-phase electrochemistry of a similar complex, $[(\text{tpy})\text{Ru}(\text{tpp})\text{RhCl}_3](\text{PF}_6)_2$, shows one reversible oxidation, one irreversible reduction, and three reversible reductions (see Table 3.3).⁸³ Interestingly, the first reduction (irreversible) corresponds to a two-electron reduction based on the Rh metal center. This reduction leads to the loss of two chloride ligands and the rearrangement around the Rh into a square-planar coordination

Table 3.2 High-mass fragments observed by MALDI-TOFMS.

Ru-Ru-Ru	$[M]^+$	$[M-(PF_6)]^+$	$[M-2(PF_6)]^+$	$[M-3(PF_6)]^+$	$[M-4(PF_6)]^+$
	— (2047)	1902 (1902)	1757 (1757)	1612 (1612)	— (1467)
Ru-Ir-Ru	$[M]^+$	$[M-(PF_6)]^+$	$[M-2(PF_6)]^+$	$[M-3(PF_6)]^+$	$[M-4(PF_6)]^+$
	— (2283)	— (2138)	1993 (1993)	1848 (1848)	1704 (1703)
Ru-Ru-Rh	$[M-2Cl]^+$	$[M-2Cl-(PF_6)]^+$	$[M-2Cl-2(PF_6)]^+$	$[M-2Cl-3(PF_6)]^+$	$[M-2Cl-4(PF_6)]^+$
	— (1930)	— (1785)	1641 (1640)	1495 (1495)	1350 (1351)

Values in parenthesis are calculated monoisotopic masses. A dash indicates no peak was observed for that ion.

Table 3.3 Oxidation and reduction potentials for the inorganic coordination complexes investigated.

$E_{1/2}$ (V) ^a	oxidation ^e	oxidation	reduction	reduction	reduction	reduction
Ru-Ru-Ru ^b	+0.83	+1.60	-0.71	-0.88	-1.43	-1.52
Ru-Ir-Ru ^c	NR	+1.56	-0.39	-0.54	-1.06	-1.22
Ru-Rh ^d	NR	+1.60	-0.23 ^f	-0.60	-0.98	-1.40

^a Measured vs. Ag/AgCl. ^b Adapted from Brauns, et al. ^c Adapted from Bridgewater, et al. ^d Adapted from Lee, et al. ^e See appropriate reference for exact redox assignments. ^f Irreversible, two-electron reduction centered on Rh. NR indicates no value was reported.

geometry. Although $[(\text{tpy})\text{Ru}(\text{tpp})\text{RhCl}_3](\text{PF}_6)_2$ is not the same compound we studied, the third Ru-metal center is far removed from the Rh-metal center. Therefore, the redox chemistry at the Rh-metal center in the trimetallic complex is expected to be similar. Ligand-based reductions of these two complexes are expected to be significantly different. With this in mind, we again observe the same trend for the Rh reduction in the MALDI-TOF-MS analysis as in the solution-phase electrochemistry.

The complexes may be reduced in solution during preparation. Several of the matrix compounds used are acids that would be good reducing agents. However, reduction of a metal-polypyridyl complex affects the charge transfer states that are responsible for the color of many inorganic coordination complexes. In other words, reduction of the complex would lead to a visible color change. The color of the complex was clearly visible when a high concentration (matrix-to-analyte ratio of 200) was used to prepare the MALDI spots. No color change was observed during the MALDI preparation of the complexes, which provides evidence against solution-phase reduction.

3.3.4 Matrix Selection

The quality of the MALDI analysis depends strongly on the choice of matrix. In the analysis of all complexes used in this study, we investigated a series of matrices that included proton-donating matrices (SA, DHB, HCCA, DHC, ACA), electron-scavenging matrices (DNBA, mDNB), and neutral matrices (ATT, dithranol) (Figure 3.8). The MALDI spectra using the electron-scavenging matrices resembled those of direct LDI and did not show the $[\text{M}-n(\text{PF}_6)]^+$ ion series in the mass spectra. However, in light of the correlation with the redox chemistry it is not surprising that electron-withdrawing matrices do not generate intact polymetallic ions. Of the remaining matrices only SA, DHB, HCCA, and ATT showed the $[\text{M}-n(\text{PF}_6)]^+$ pattern in the MALDI spectra.

Although four matrices produced the $[\text{M}-n(\text{PF}_6)]^+$ pattern, they did not perform equally well. The most dramatic example is DHB. Even at low matrix-to-analyte ratios (100:1) there were a significant number of matrix adducts. As seen in Figure 3.9, increasing the matrix-to-analyte ratio made the matrix adduct peaks more intense than the $[\text{M}-n(\text{PF}_6)]^+$ ion signals. Of the four successful matrices, SA and ATT gave the best

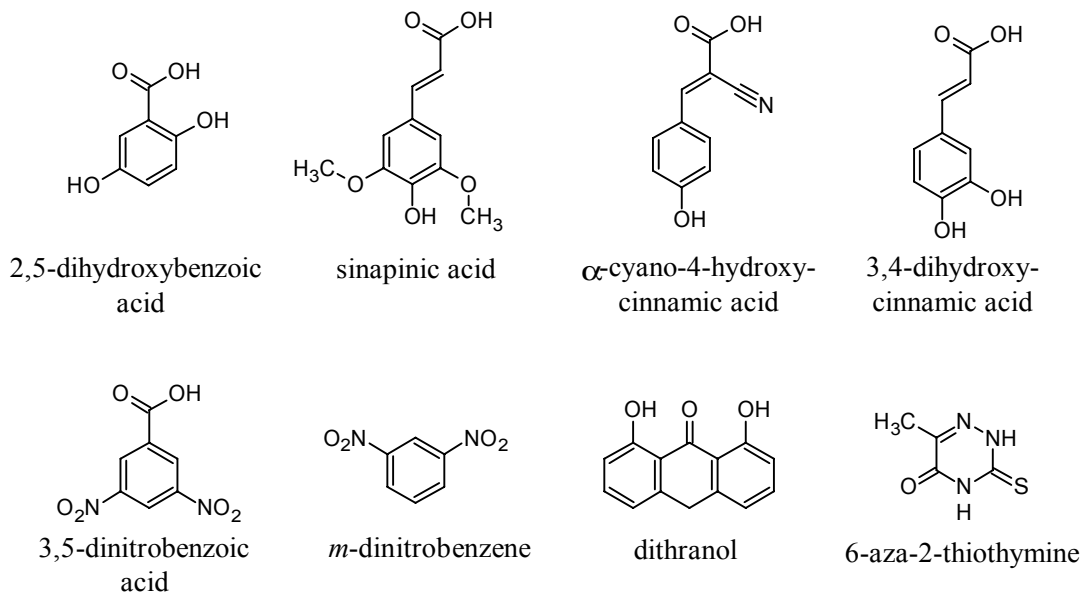


Figure 3.8 Molecular structures of the organic matrix compounds used to study the inorganic coordination complexes. The matrices that produce the $[M-n(\text{PF}_6)]^+$ ions are sinapinic acid, α -cyano-4-hydroxycinnamic acid, 2,5-dihydroxybenzoic acid, and 6-aza-2-thiothymine.

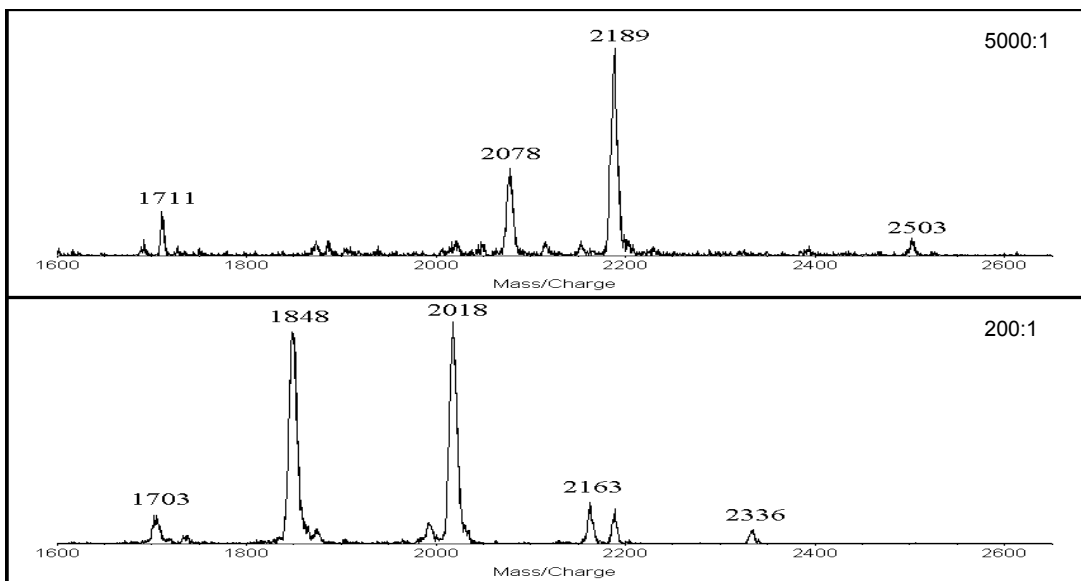


Figure 3.9 MALDI mass spectra of $\{[(\text{bpy})_2\text{Ru}(\text{dpp})]_2\text{IrCl}_2\}(\text{PF}_6)_5$ in 2,5-dihydroxybenzoic acid acquired on the Kratos Kompact SEQ with an acceleration potential of 24 kV. The top and bottom spectra have matrix-to-analyte ratios of 5000:1 and 200:1, respectively. The higher matrix-to-analyte ratio results in matrix adducts and does not produce the ion series $[M-n(\text{PF}_6)]^+$.

results. They produced few, if any, matrix adducts and a broad range of $[M-n(\text{PF}_6)]^+$ peaks. HCCA produced fair results, but like DHB also had a tendency to produce matrix adducts.

3.3.5 Matrix-to-Analyte Ratio

For the matrices that produced the $[M-n(\text{PF}_6)]^+$ series, the matrix-to-analyte ratio was investigated by varying the ratio from 200:1 to 5000:1. With the exception of DHB, the $[M-n(\text{PF}_6)]^+$ region of the spectra did not show much variability. Figure 3.10 shows MALDI spectra of $\{[(\text{bpy})_2\text{Ru}(\text{dpp})]_2\text{IrCl}_2\}(\text{PF}_6)_5$ in sinapinic acid. The top and bottom spectra have matrix-to-analyte ratios of 5000:1 and 200:1. It is clear that the spectra are similar, and do not follow the same trend as that observed using DHB. The matrix-to-analyte ratio does affect the lower-mass monometallic fragments as observed in these two spectra. The monometallic fragments in the 200:1 matrix-to-analyte sample preparation are relatively larger than those in the 5000:1 preparation. Again, it should be noted that peaks seen at m/z less than 480 are matrix peaks. This trend is sensible because at high dilution ratios (5000:1) the matrix is absorbing more of the laser pulse

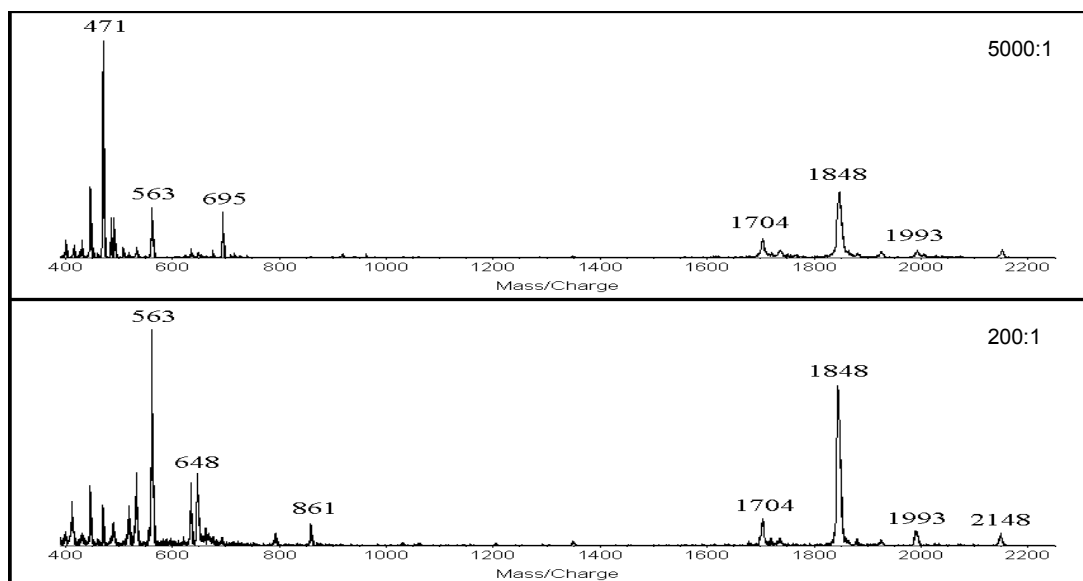


Figure 3.10 MALDI-TOF mass spectrum of $\{[(\text{bpy})_2\text{Ru}(\text{dpp})]_2\text{IrCl}_2\}(\text{PF}_6)_5$ in sinapinic acid collected on the Kratos Kompact SEQ with an acceleration potential of 24 kV. The top and bottom spectra have matrix-to-analyte ratios of 5000:1 and 200:1, respectively. The major difference is seen in the low mass region where the monometallic fragment ions are seen.

energy so that the complex is less likely to fragment due to direct absorption. However, the higher matrix-to-analyte ratios have a tendency to produce high-mass matrix adduct peaks with significant intensity, making interpretation and characterization more difficult. A low to moderate matrix-to-analyte ratio (500:1 – 2000:1) appears to give the best results.

3.4 Conclusions

There have been many papers published that discuss gas-phase chemistry of inorganic coordination complexes,^{86,87} but to our knowledge there are few if any that study multimetallic complexes in the gas-phase. Our results demonstrate the ability to use MALDI to produce stable, gas-phase ions of multimetallic supramolecular complexes. For the UV-absorbing complexes that we studied, the mass spectra exhibit characteristics of both hard (direct LDI) and soft (MALDI) ionization techniques. The extent of fragmentation and adduct formation can be controlled by adjusting the matrix-to-analyte ratio.

Both direct LDI and MALDI produced suitable mass spectra to characterize the monometallic complex. The direct LDI of such monometallic complexes can be a useful alternative to MALDI if matrix or adduct peaks interfere with measurement of the analyte peaks. Direct LDI of the trimetallic complexes resulted in extensive fragmentation with no fragments containing more than one metal. MALDI analysis of the trimetallic complexes resulted in fewer low-mass fragments and a series of high-mass ions that allowed complete structural characterization of the complexes.

The fragmentation patterns of the pseudomolecular ions in the MALDI spectra could be correlated to the known redox behavior of the trimetallic complexes. Although it is difficult to extrapolate too far between gas- and solution-phase phenomena, this result does suggest that MALDI mass spectrometry could be used to predict redox properties of closely related complexes.

There are several interesting possibilities for the extension of this research. The bridging ligand dpp becomes easier to reduce when aromatic groups are bonded to the side of the pyrazine ring. Bridgewater, et al.⁸² synthesized a series of complexes using the dpp-based ligands shown in Figure 3.11: $\{[(\text{bpy})\text{Ru}(\text{dpp})]_2\text{IrCl}_2\}^{5+}$ (which was studied

in this research), $\{[(bpy)Ru(dpq)]_2IrCl_2\}^{5+}$, and $\{[(bpy)Ru(dpb)]_2IrCl_2\}^{5+}$. The change in reduction potential in this series is more subtle than the change observed for the series of complexes discussed in this chapter. The change in reduction potential between $\{[(bpy)Ru(dpp)]_2IrCl_2\}^{5+}$ and $\{[(bpy)Ru(dpp)]_2RuCl_2\}^{5+}$ is about 0.32 V for each of the first four reductions (refer to Table 3.3). The change between $\{[(bpy)Ru(dpq)]_2IrCl_2\}^{5+}$ and $\{[(bpy)Ru(dpb)]_2IrCl_2\}^{5+}$ is about 0.16V for the first four reductions.⁸² Future experiments will determine if there is still a shift in the $[M-n(PF_6)]^+$ series of peaks for the smaller change in reduction potential observed in these two complexes.

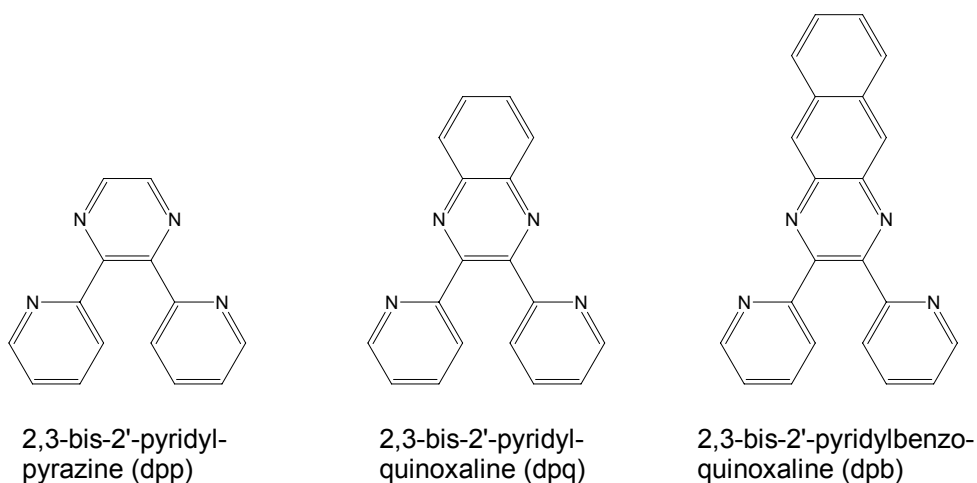


Figure 3.11 Bridging ligands used to study the effect of conjugation on the spectroscopic properties of polymetallic inorganic coordination complexes. The complexes become easier to reduce as the aromatic system is extended. (See Bridgewater, et al.)

A series of complexes that have a broader range of reduction potentials should be investigated. According to the results presented in this chapter the observed series of peaks will depend on the reduction potentials of the complex. The data in Table 3.2 and 3.3 indicate there may be a reduction potential “window” for the observed ions. Assuming ionization is a result of protonation of the fully reduced complex, the three peaks observed for $\{[(bpy)_2Ru(dpp)]_2RuCl_2\}(PF_6)_4$ correspond to species with reduction potentials between -0.71 and -1.43 V. Similarly, the series for $\{[(bpy)_2Ru(dpp)]_2IrCl_2\}(PF_6)_5$ correspond to species with reduction potentials between -0.54 and -1.22 V. However, these two observations do not provide enough evidence to suggest that there is a reduction potential range for ions produced by MALDI. Data

from a larger number of complexes will help determine whether there is a reduction potential “window” for stable ion formation in the MALDI plume.

Chapter 4 – Using MALDI-TOFMS to Study Cyanobacteria

4.1 Introduction

The advent of soft ionization techniques like ESI and MALDI have made mass spectrometry a vital tool for studying biochemical processes in organisms. Since the 1980's mass spectrometry has been used to characterize carbohydrates, peptides, proteins, DNA, metabolites, phospholipids, and whole cells.⁸⁸ Mass spectrometry provides a rapid method for positive identification of biomolecules based upon molecular weight and offers better resolution and improved mass accuracy compared to techniques such as SDS-PAGE.

Cyanobacteria are widely studied organisms with many interesting properties such as the ability to withstand desiccation, a wide range of pH and temperature, and the ability to protect themselves against UV exposure.⁸⁹ This chapter will discuss the utility of mass spectrometry in the study of cyanobacteria. I have developed a rapid MALDI-TOFMS screening method for the UV-absorbing pigment scytonemin⁹⁰ and peptide mass fingerprinting is used to monitor the production and purification of an interesting cyanobacterial protein known as Wsp. I also discuss many other possibilities in the future experiments section.

4.1.1 Background Information on Cyanobacteria

Cyanobacteria are prokaryotic organisms that use sunlight as their source of energy (photosynthetic) and can fix carbon and nitrogen from the atmosphere for synthesis of biological molecules with oxygen as the byproduct (autotrophic). Cyanobacterial cells, like many other gram-negative bacteria, are encapsulated in an extracellular polysaccharide sheath (EPS) and tend to grow in colonies. Colonies of *Nostoc commune*, a common species of cyanobacteria, range from several millimeters to tens of centimeters in size. The EPS protects cells from phagocytosis, acts as an anchor for binding to substrates, protects cells during desiccation, and prevents lysis by other bacteria and viruses.⁹¹ The EPS makes up about 60% of the dry weight of *N. commune* colonies. Water stress polypeptides and UV-absorbing pigments are also contained in the EPS.

Cyanobacteria are believed to be the first photoautotrophic (using sunlight for energy and producing oxygen) organisms on earth and are likely to be responsible for the development of the ozone layer and the accumulation of oxygen in our atmosphere.^{92,93} Fossils date the origin of cyanobacteria to approximately 3.4 billion years ago.⁹⁴ Their ability to fix atmospheric nitrogen is important to other life forms (i.e. heterotrophs), and they represent the first step in the nitrogen cycle. Special cells called heterocysts carry out nitrogen fixation. Nitrogen is reduced by a series of enzymes to produce ammonia, which is then used to produce all of the nitrogen-containing biomolecules. Ammonia is also released from the cells to the surrounding environment, thus providing heterotrophs with a source of nitrogen. For this reason, many species have some degree of a symbiotic relationship with proximal life forms.⁹⁵ Cyanobacteria are believed to be vital for the successful production of rice because of their contribution to the fertility of soil.⁹⁶

There are hundreds of species of cyanobacteria, which can be found in every part of the world, including polar regions, deserts, caves, aquatic habitats, and terrestrial environments. The ability to survive in harsh environments has earned these bacteria the title of extremophiles. Exposure to UV-light and dehydration/rehydration cycles are two of the stresses that cyanobacteria must endure in order to survive.

Many species of cyanobacteria, most notably *N. commune*, have the unique ability to withstand long periods of desiccation. Cultures of cyanobacteria have resumed physiological activity after one hundred years of desiccation.⁹⁷ Desiccation tolerance in cyanobacteria is poorly understood, but is believed to be facilitated by the EPS, the non-reducing disaccharides trehalose and sucrose, and a variety of water stress proteins (Wsp).^{98,99} The role of these compounds is most likely to maintain the structural integrity of cell membranes during desiccation.

Intense UV light can cause extensive damage to cells, including DNA mutation, inhibition of photosynthetic productivity, inhibition of heterocyst formation, production of harmful radical species, and lipid peroxidation.¹⁰⁰ Avoidance, repair, and protection are the three basic mechanisms used to cope with the deleterious effects of UV radiation. Most organisms use a combination of all three of these mechanisms.

Numerous cyanobacteria use avoidance as a UV-protection mechanism. Species of *Chroococcidiopsis* that grow in the arctic regions are chasmoendolithic, meaning they grow within the void spaces inside rocks to avoid UV exposure.¹⁰¹ Cyanobacteria growing in aquatic environments use gas vacuoles to migrate up and down the water column to avoid UV light.¹⁰² At midday they reside below the water surface, where other compounds in the water absorb most of the UV light, while at night they rise to the surface. Cyanobacteria in terrestrial mat communities will grow below other species, such as fungi or lichens, in order to avoid UV exposure.¹⁰³ However, it is not always possible for cyanobacteria to take advantage of avoidance as a mechanism for UV protection.

Repair mechanisms use enzymes and other molecules produced by the organism to fix damaged molecules. Superoxide dismutase is an enzyme that is responsible for the destruction of reactive species that lead to mutations in DNA, such as hydrogen peroxide, hydroxyl radicals and superoxide radicals.¹⁰⁴ Carotenoids act as antioxidants for removal of singlet oxygen species and triplet chlorophyll, and they inhibit lipid peroxidation.¹⁰⁰ A series of enzymes that are also responsible for degradation and resynthesis of damaged proteins. Repair mechanisms have several shortcomings. First, repair mechanisms require physiological activity and therefore do not protect cyanobacteria during periods of desiccation. Second, it is always better to prevent damage than to repair it. Finally, as the extent of damage increases the reliability of repair mechanisms diminishes.¹⁰⁴

Preventative mechanisms involve the synthesis of UV-absorbing pigments. Mycosporine-like amino acids are a class of compounds synthesized by a variety of organisms, including cyanobacteria, fungi, algae, and marine invertebrates.¹⁰⁵ Approximately nineteen different MAAs have been identified in nature and they all have the same basic cyclohexanone core with various amino acid or amino alcohol groups as substituents. In *N. commune* one MAA is covalently linked to oligosaccharides and is located in the EPS.¹⁰⁶ This pigment has an absorption maximum at 335 nm and absorbs approximately 67% of UV radiation before it reaches the cells. Although the absorbance maximum is in the UV-A range (315-400 nm), there is a significant absorption in the UV-

B range. Another MAA produced in *N. commune* has an absorbance maximum at 310 nm and is largely responsible for filtering UV-B radiation (280-315 nm).

Scytonemin is a UV-absorbing pigment that is only produced by cyanobacteria.¹⁰⁷ The *in vivo* absorbance maximum for scytonemin is 370 nm, but absorption ranges from 240 to 450 nm. Scytonemin is the only cyanobacterial pigment that has a significant absorption in the UV-C region (190-280 nm). Presently the Stratosphere absorbs all of the UV-C radiation before it reaches the earth, however UV-C radiation did reach earth's surface prior to the development of the atmosphere. It is speculated that scytonemin played an important role in the survival of early cyanobacterial species due to the absorbance of UV-C radiation.¹⁰⁸ Scytonemin is the predominant UV-A-absorbing pigment produced by cyanobacteria, and is thought to be derived from metabolites of aromatic amino acid synthesis. The chemical structures of scytonemin in the oxidized and reduced form are shown in Figure 4.1. This lipid-soluble, symmetrical indolyphenol is quite stable under neutral conditions, and is not subject to rapid photodegradation as evidenced by long-term persistence in terrestrial crusts and dried cultures.¹⁰⁹

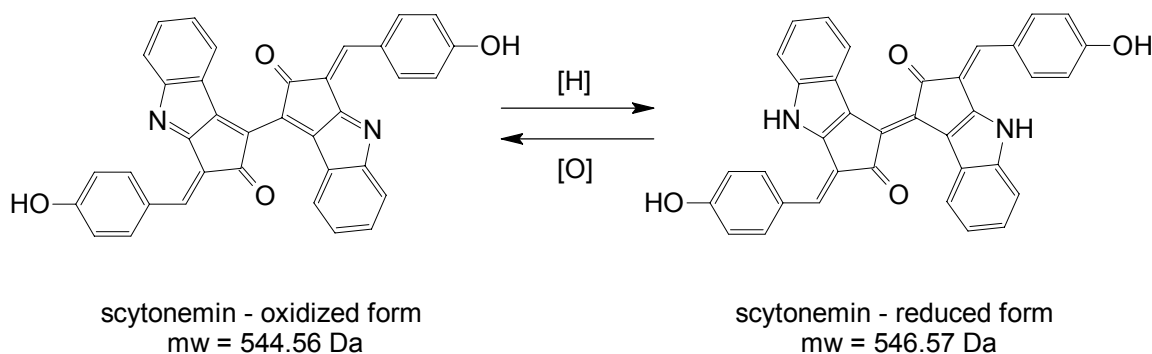


Figure 4.1 Chemical structure of the UV-photoprotective pigment scytonemin in the oxidized and reduced forms.

4.1.2 Using Mass Spectrometry to Study Organisms

Because of its many advantages, MS has become a standard part of many biology and biochemistry laboratories. MS has been particularly useful in the emerging field of proteomics.^{22,110} Proteomics, short for PROTEin analysis using information provided by genOMICS, is the natural extension of genomics. By analyzing patterns of

protein expression, proteomics seeks to correlate different cellular states with specific protein expression and, by extension, gene expression. For example, cyanobacterial cultures grown with and without UV exposure will produce different amounts of various proteins. MS is used to monitor differential protein expression between the two cultures. This information can then be correlated with known genetic information, which will provide a better understanding of mechanisms and pathways involved in UV tolerance.

There are essentially two functions for mass spectrometry in proteomics: peptide mass fingerprinting and *de novo* sequencing. Peptide mass fingerprinting is a technique used to identify proteins whose amino acid sequences are known.^{111,112} Figure 4.2 gives a schematic illustration of the steps involved in identifying a protein using a peptide mass fingerprint. Typically, a mixture of proteins is separated using SDS-PAGE in one or two dimensions. Gel bands are then excised and subjected to proteolytic cleavage, most often using trypsin. This process is known as in-gel digestion. Trypsin is an enzyme that cleaves peptide bonds at the carboxy-terminus of lysine and arginine amino acid residues. The selective activity of trypsin leads to a predictable series of peptides which are then extracted from the gel and analyzed by mass spectrometry. The peptides detected by the mass spectrometer make up the “fingerprint” and the mass values are used to search a database to identify the protein if unknown. Database searches are typically restricted by additional parameters such as protein molecular weight and species of origin, both of which are typically known. One of the most reliable databases for protein sequences is the Swiss-Prot database which was established by the Swiss Institute of Bioinformatics and the European Bioinformatics Institute.^{113,114} Entries to this database are evaluated by a group of scientists prior to inclusion. This evaluation results in fewer sequences entered into the database, but a much lower occurrence of sequence errors and a high degree of annotation. The database is public and there are several web-based search engines that use the Swiss-Prot database.^{115,116} These web sites also have other useful tools, for example the protein sequence can be used to generate a list of peptides resulting from treatment with a variety of proteolytic enzymes. This tool is useful for routine identification of protein known to be present in a mixture.

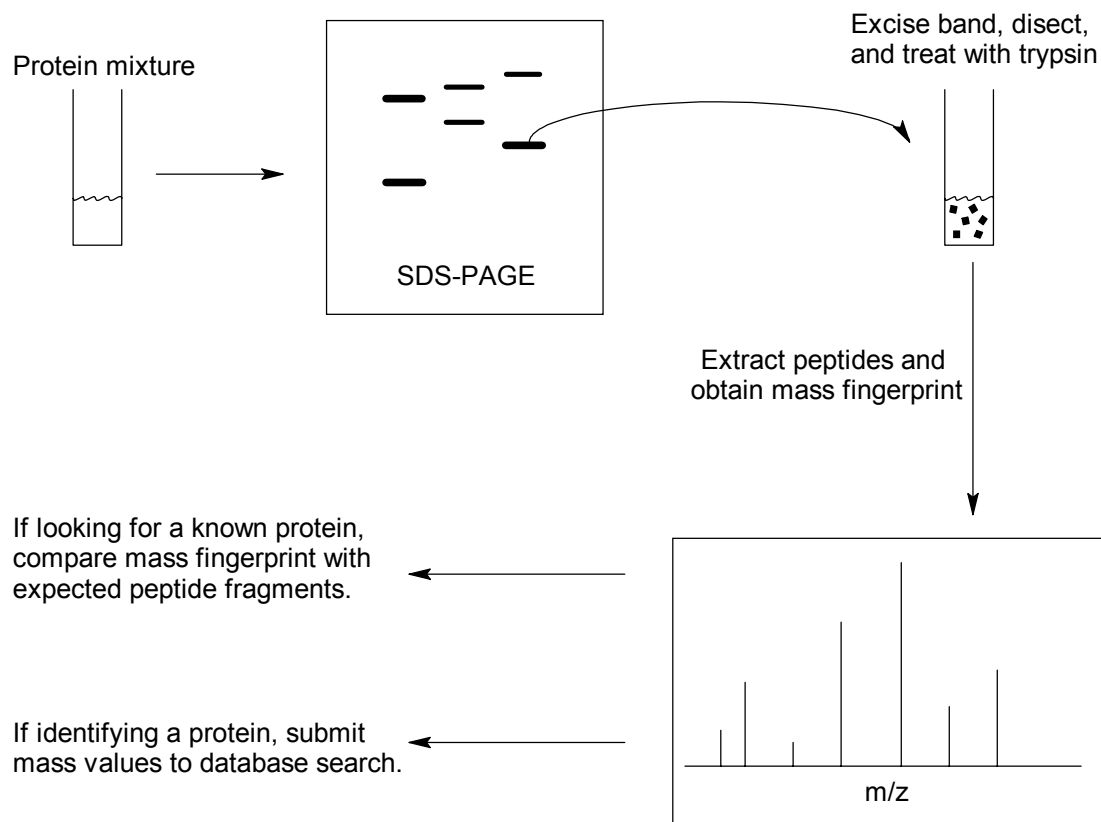


Figure 4.2 Schematic illustration of the steps involved in peptide mass fingerprinting.

Peptide mass fingerprinting is used to identify unknown proteins and/or to confirm the identity of a known protein. Both of these applications will be discussed in Section 4.3.3. MALDI-TOFMS is usually the instrument of choice for peptide mass fingerprinting because of the ability to detect all of the peptides simultaneously. The positive identification of a protein using a peptide mass fingerprint with database searching generally requires that a minimum of 15% of the amino acid sequence is represented by the peptides detected.¹¹⁷ Four independent peptides (i.e. with no sequence overlap) are usually sufficient to obtain 15% sequence coverage, but this depends on the molecular weight of the protein and the length of the peptides detected.

Mass accuracy is a very important aspect of protein identification using peptide mass fingerprinting. Clauser, et al. explored the role of mass accuracy in identifying proteins using peptide mass fingerprinting.¹⁸ Their study showed that if the mass accuracy is ± 10 ppm, no false positive identifications were returned when as few as five peptides were matched. The number of peptides required for an accurate match

increases as the mass accuracy decreases, as nine peptides are required to eliminate false positives at a mass tolerance of ± 0.5 Da. However, this study did not consider the possibility of limiting the search using a molecular weight range (known from SDS-PAGE) and species of origin. These limitations will loosen the restrictions on the number of peptides required for a given mass accuracy. A high degree of mass accuracy can be obtained using an internal calibration and by attaining isotopic resolution. Internal calibration is typically achieved using several of the peptide peaks due to the autolysis of trypsin, since these are almost always present. Isotopic resolution provides narrower peak widths which leads to less uncertainty in the mass of the observed peak.

De novo sequencing requires a tandem mass spectrometric technique, most commonly ESI-MS-MS using either a triple quadrupole or ion-trap mass analyzer.¹¹⁸ The peptide mixture resulting from proteolytic digestion is separated by chromatography and each peptide is introduced to the mass spectrometer independently. A parent-ion spectrum is obtained for each peptide as it elutes from the column. Subsequently, the parent ion is fragmented through gas-phase collisions and a daughter-ion spectrum is obtained. Commercial instruments are available that allow for automation of parent- and daughter-ion spectra. The data is then analyzed using computer algorithms developed based on the fragmentation behavior of polypeptides.^{118,119} *De novo* sequencing is a considerably more involved technique than peptide mass fingerprinting and requires a great deal of expertise.

4.2 Experimental Details

4.2.1 Scytonemin Screening

All solvents were HPLC-grade, and reagents were used as received. Growth of laboratory cultures was accomplished at room temperature under ambient conditions and/or exposed to high UV-A/B light. Cells were harvested from the plates and vacuum-dried directly. Field materials were in the desiccated state at the time of collection.

Sample preparation involved grinding the dried cells (0.5 mg) with a mortar and pestle and then extraction with organic solvents (250 μ L). The matrix solution was

prepared by dissolving DHB (4 mg) in a 9:1 (v/v) mixture of acetonitrile and water (250 μ L). An aliquot (1 μ L) of the extract was combined with matrix solution (1 μ L) on the sample probe and allowed to dry. The sample spot was then dissolved in methanol (0.5 μ L) and quickly evaporated under a stream of nitrogen to generate a thin, microcrystalline layer. As mentioned in Section 3.2.2, this results in better shot-to-shot reproducibility due to improved sample homogeneity.

Initial experiments on *Nostoc commune* CHEN were performed on the Comstock RTOF/210 reflectron time-of-flight mass spectrometer. Ion source potentials are given in Section 1.3.1. Aliquots of matrix and extract were spotted onto the aluminum probe extension, as discussed in Section 3.2.3. All other instrument conditions are identical to those described in Section 3.2.3.

Extracts from *N. commune* DRH-1, *N. punctiforme*, *Chroococcidiopsis* sp 029, and field material from Storr's Lake were analyzed using the Kratos Kompact SEQ (see Section 1.3.2). Delayed extraction was set to optimize the scytonemin signal at 547 Da. Typically data from 50 to 75 laser shots were collected to generate an averaged spectrum. All spectra collected on this instrument were calibrated using the factory calibration.

4.2.2 Protein Analysis

All solvents were HPLC-grade with the exception of water, which was doubly distilled and deionized. Sinapinic acid and α -cyano-4-hydroxycinnamic acid were prepared as saturated solutions in 50% acetonitrile:0.1% trifluoroacetic acid and were prepared fresh daily. BSA was purchased from Aldrich and was prepared as a 0.66 mg/mL solution in water. The in-gel digestion protocol, including MALDI sample preparation and materials used are found in Appendix B.

All spectra were recorded using the Kratos Kompact SEQ as described in Section 1.3.2. Mass spectra are typically shown as an average of 50 shots. Details regarding mass calibration can be found in the discussion section.

Database searches and theoretical peptide mass calculations were performed using the ExPASy Molecular Biology Server.¹²⁰ The Swiss-Prot database was used to identify the unknown proteins from *E. coli* and to confirm the results of BSA peptide

mass fingerprinting. Typical search parameters include species of origin, molecular weight range ($\pm 10\%$), 0.5 Da mass tolerance, a minimum of four peptides required for a match, monoisotopic masses for $[M+H]^+$, and trypsin as the enzyme allowing for one missed cleavage. A peak intensity cutoff of greater than 5 mV was incorporated when identifying peaks from the peptide mass fingerprint.

Growth of the cultures as well as production, isolation, and purification of Wsp was performed by another member of the research team.¹²¹ He also conducted SDS-PAGE analysis of protein mixtures, Western blot studies, and Bradford's tests. After about 24 hours of growth, the supernatant from recombinant *E. coli* cultures was collected, which should contain Wsp. The supernatant was then desalted and concentrated using ultrafiltration. The concentrated supernatant was then subjected to ion-exchange chromatography and fractions were collected every two minutes. Fractions containing Wsp were then subjected to a dye-affinity column for further purification.

4.3 Results and Discussion

4.3.1 Scytonemin Screening

Initial experiments were conducted using *N. commune* CHEN, a dehydrated specimen collected in the Hunan Province of China.⁹¹ The results of the MALDI-TOFMS analysis of a solvent extraction, using 1:1 methanol:acetonitrile, of *N. commune* CHEN are shown in Figure 4.3. The intensity of the signal at 547 Da is comparable to the most intense matrix peaks. Comparison with the mass spectrum of DHB clearly shows that the peaks at 547, 570, and 585 Da are compounds present in the extraction. At the time it was unclear what was being extracted from the dried culture. Knowing that the UV pigments are contained in the EPS, we assumed these compounds would be the most likely to be extracted. The MAAs have much lower molecular weights (about 350 Da), but the mass did not match the biologically active oxidized form of scytonemin (see Figure 4.1).

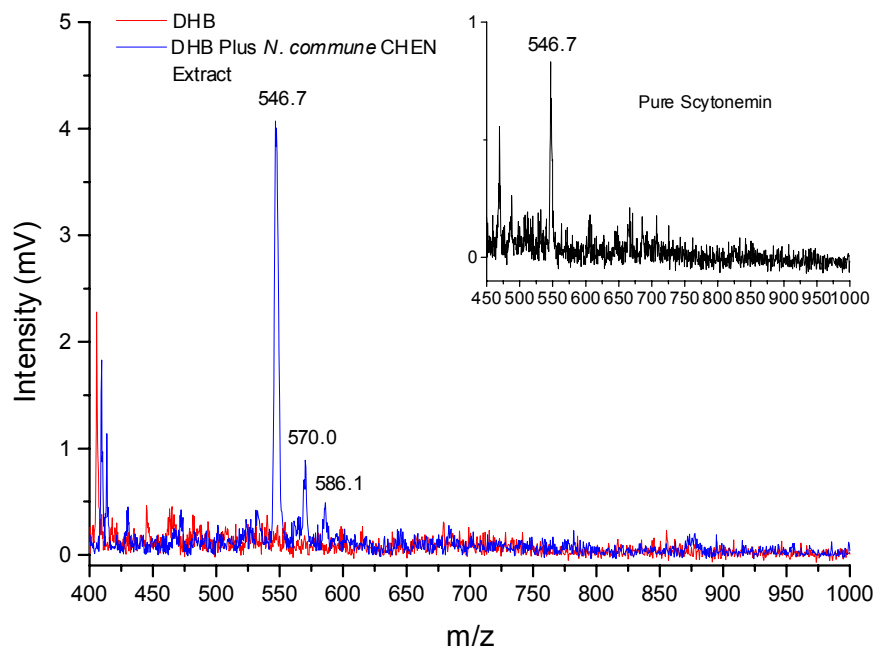


Figure 4.3 MALDI mass spectrum of a solvent extract of dried *N. commune* CHEN. DHB was used as the matrix. Comparison with the blank and analysis of pure scytonemin (inset) clearly indicates the presence of the reduced form of scytonemin. The sodium and potassium adducts (570 and 586 Da, respectively) are also seen.

Proteau and coworkers were the first to determine the chemical structure of scytonemin.¹⁰⁷ Structural elucidation included FAB MS analysis. Analysis of pure samples of both the reduced and oxidized form of scytonemin always resulted in the detection of the reduced form, at 546.6 Da. MALDI-TOFMS analysis of the solvent extract showed the same ion signal. Scytonemin is thought to be reduced during ionization in the gas phase. The evidence to support this is that no color change was observed during preparation of MALDI samples (similar to the discussion in Section 3.3.3). The oxidized form has a pale yellow-green color while the reduced form is bright red. Analysis of a pure sample of scytonemin (provided by W. Gerwick, Oregon State University) confirmed the peak at 547 Da was indeed the reduced form of scytonemin.

Further confirmation for the identity of the peak at 547 Da was obtained by the PSD analysis shown in Figure 4.4. Little fragmentation is observed because of the structural robustness of this highly conjugated molecule. The peaks at 519.7 and 491.6

Da are due to the consecutive loss of the carbonyl groups attached to the indolyl moiety. A low intensity peak at 273.8 Da is also observed for one half of the symmetric structure.

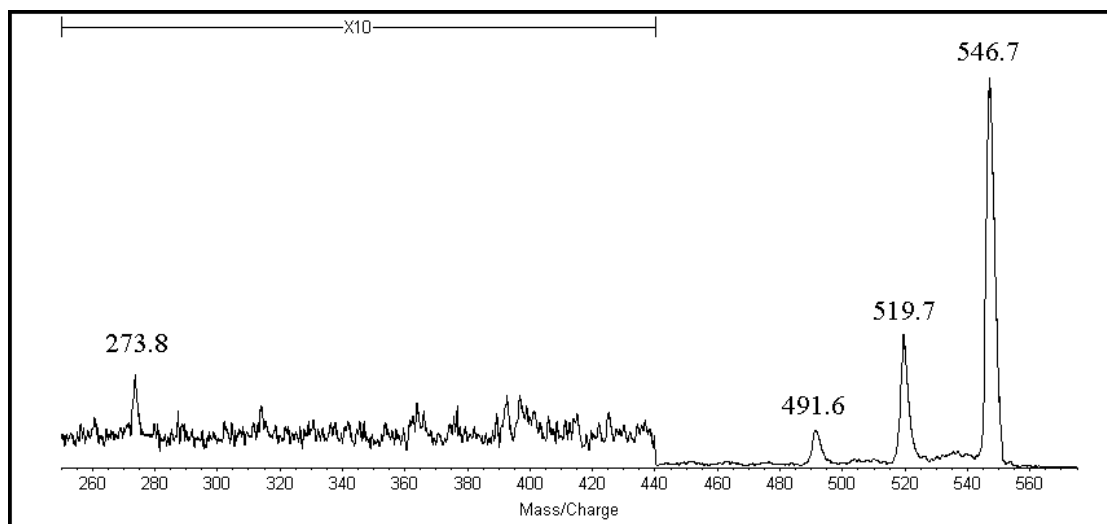


Figure 4.4 PSD mass spectrum of scytonemin. The peaks at 519.7 and 491.6 Da are most likely due to consecutive loss of carbonyl groups. The peak at 273.8 represents the monomer subunit. The region between 250 and 440 Da has been expanded ten-fold in intensity.

Several different solvent systems were investigated for the extraction of scytonemin. Extraction with methanol, acetonitrile, ethyl acetate, toluene, dichloromethane, or tetrahydrofuran did not result in an appreciable scytonemin level for *N. commune* CHEN. Different binary solvent systems were also evaluated, with 1:1 (v/v) mixture of methanol:ethyl acetate giving the best results.

A series of experiments were designed in order to test the UV induction of scytonemin using the extraction method. Scytonemin is only produced when the organism is under UV stress because it cannot afford to waste the energy to produce scytonemin when there is no stress.¹²² An approximate threshold fluence of $33 \mu\text{mol photon}\cdot\text{m}^{-2}\cdot\text{s}^{-1}$ is required in order to induce the biosynthesis of scytonemin. Higher photon fluence leads to increased amounts of scytonemin. Lab cultures of several species of cyanobacteria were grown under different light-exposure conditions. One culture was grown under ambient laboratory conditions and another was grown under UV-A/B irradiation. After a week of growth cultures were harvested and dried. Each sample was extracted using a 1:1 (v/v) mixture of methanol and ethyl acetate.

The results for *N. punctiforme* are shown in Figure 4.5. *N. punctiforme* is a plant and fungal symbiont whose complete genome sequence is currently being analyzed.¹²³ Comparison of the spectra for the different growth conditions clearly shows that UV radiation induces the biosynthesis of scytonemin in this strain. The presence of scytonemin is shown by the peaks at 546.3 Da ($[M]^+$), 547.3 Da ($[M+H]^+$), and 569.3 Da ($[M+Na]^+$).

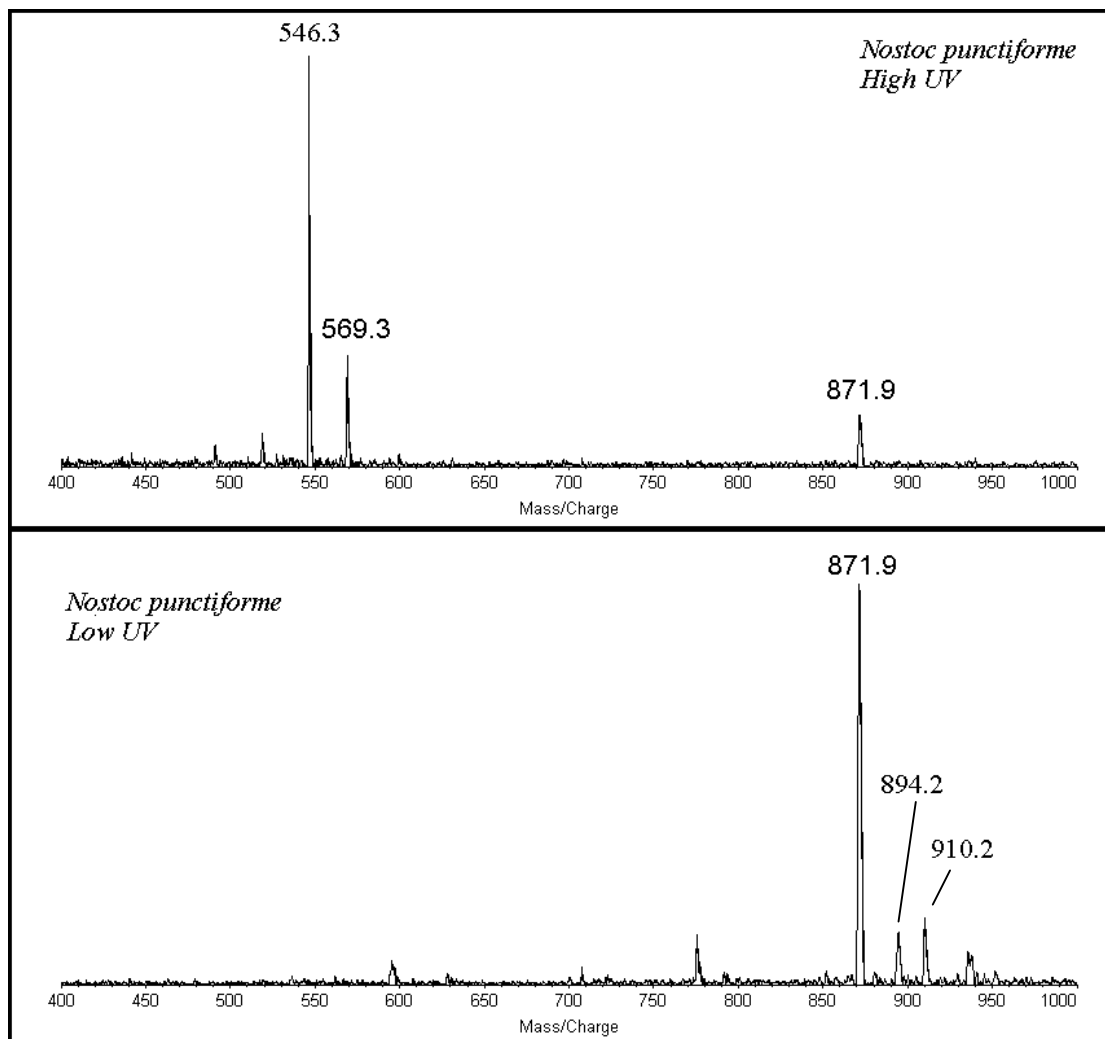


Figure 4.5 MALDI mass spectra of *N. punctiforme* cultures grown under different lighting conditions. The sample grown under UV-light shows the presence of scytonemin. The peak at 871.9 Da is pheophytin a, a derivative of chlorophyll a. Peaks at 569.3 and 894.2 are sodium adducts of scytonemin and pheophytin a, respectively, while the peak at 910.2 is the potassium adduct of pheophytin a.

The peak at 871.9 Da corresponds to pheophytin a, a result of the extraction of chlorophyll a from the dried cultures.¹²⁴ Pheophytin a has the same chemical structure as chlorophyll a except for the coordination of the magnesium ion to the porphyrin ring. The average molecular weight of pheophytin a is 871.2 g/mol. The peak in the spectrum at 871.9 Da is therefore the protonated ion of pheophytin a ($[M+H]^+$). The sodium ($[M+Na]^+$ at 894.2 Da) and potassium ($[M+K]^+$ at 910.2 Da) adducts of pheophytin a are also seen in the spectrum of *N. punctiforme* grown under ambient conditions. The identity of the peak at 871.9 Da was confirmed using PSD analysis. The chemical structure of pheophytin a and its PSD spectrum are shown in Figure 4.6. The peak at 593.5 Da is a result of the loss of the phytol side chain of pheophytin a and the peak at 533.9 Da shows the further loss of $HCOOCH_3$. The same fragmentation pattern has been observed using ESI with an ion-trap mass spectrometer.¹²⁵

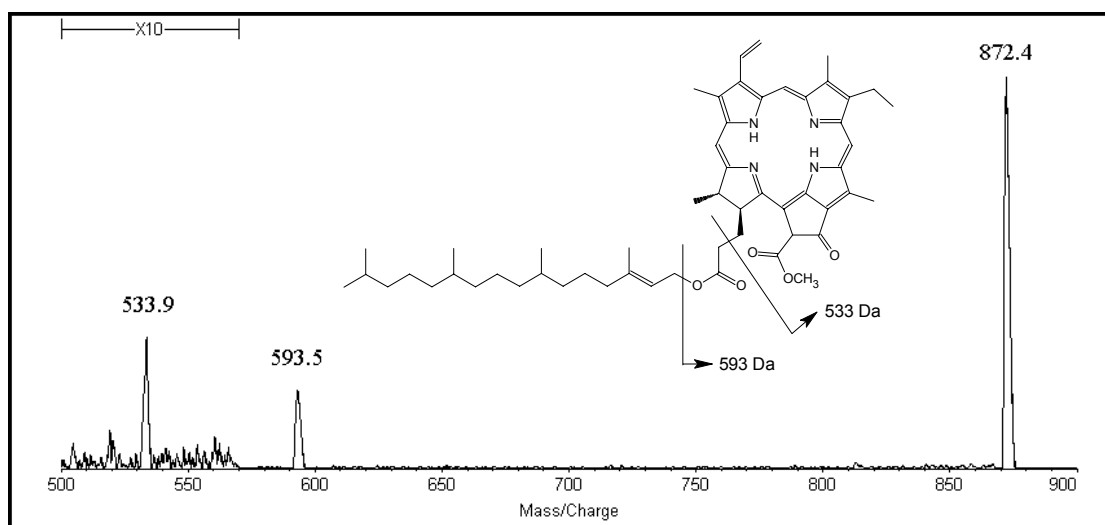


Figure 4.6 PSD spectrum of pheophytin a. The two main fragments, shown by arrows, are a result of the loss of the phytol side chain and subsequent loss of $HCOOCH_3$. The region around the peak at 533.9 Da was expanded by a factor of 10.

Lab cultures of *Nostoc commune* DRH-1 and *Chroococcidiopsis* were also grown with and without exposure to UV-A/B light. *N. commune* DRH-1 is the laboratory strain of the field material *N. commune* CHEN. The results, seen in Figure 4.7, show that this strain does produce scytonemin when grown under UV stress. There are many matrix peaks in these spectra, suggesting that the concentration of scytonemin is low. The only peaks that correspond to signals from the extract are 546.5 (scytonemin), 871.8, and 894.5 Da (pheophytin a and its sodium adduct), all others are a result of

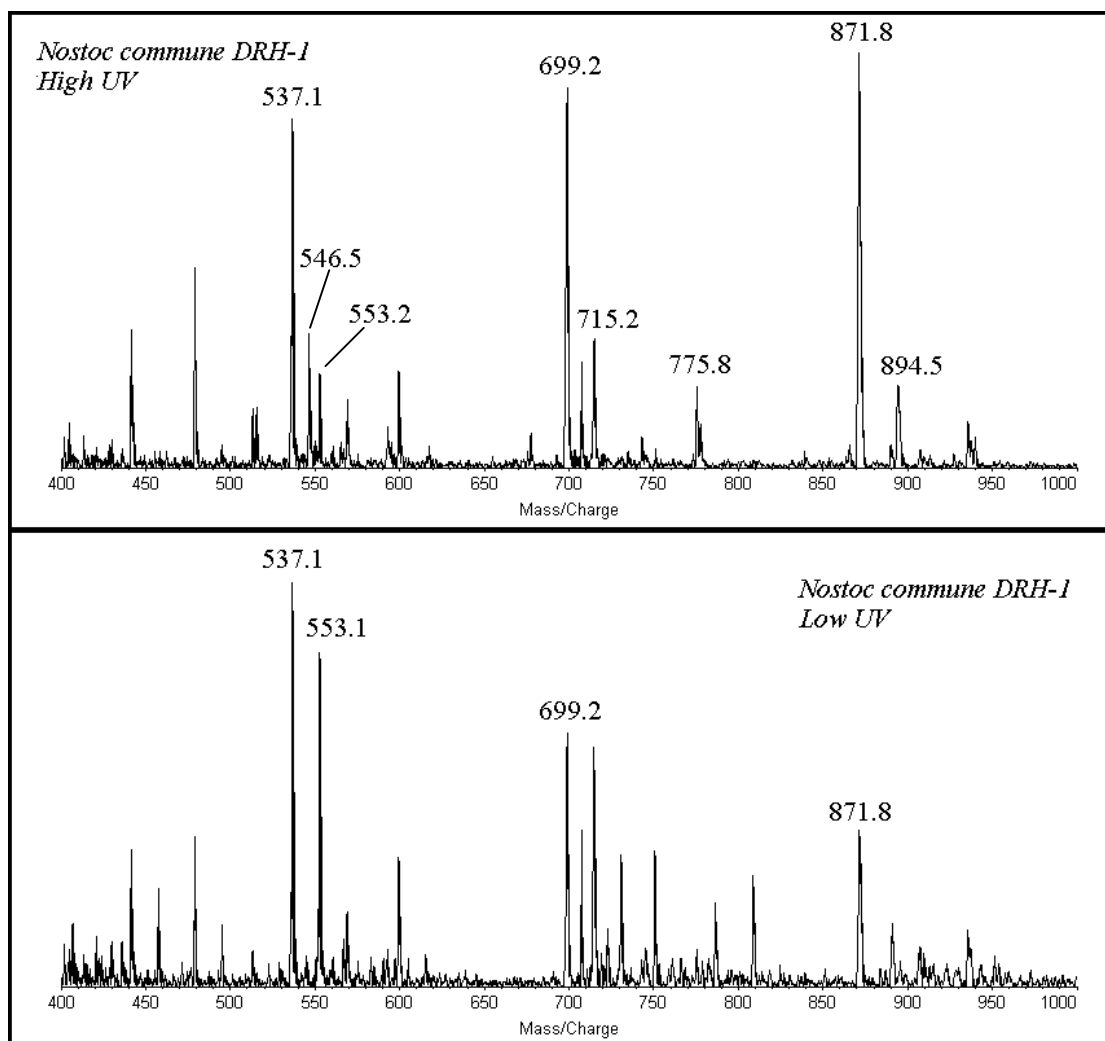


Figure 4.7 MALDI mass Spectra showing the biosynthesis of scytonemin when the culture is grown under UV light. All peaks except 546.5, 871.8, and 894.5 Da are matrix peaks.

matrix aggregates. The strain of *Chroococidiopsis* studied is chasmoendolithic and is not expected to produce scytonemin. Analysis of this culture was used as a control experiment to test the validity of the extraction method. Figure 4.8 shows that scytonemin was not produced in either the high- or low-UV culture, as expected. The absence of a peak at 546.6 Da in the control experiment ensures that no other species are extracted that have the same mass as scytonemin.

The screening technique was applied to the study of field samples taken from brown- to black-colored desiccated crusts (dried cyanobacterial mats). The crusts were collected at Storr's Lake, a hypersaline lake in the Bahamas. The absolute salt content

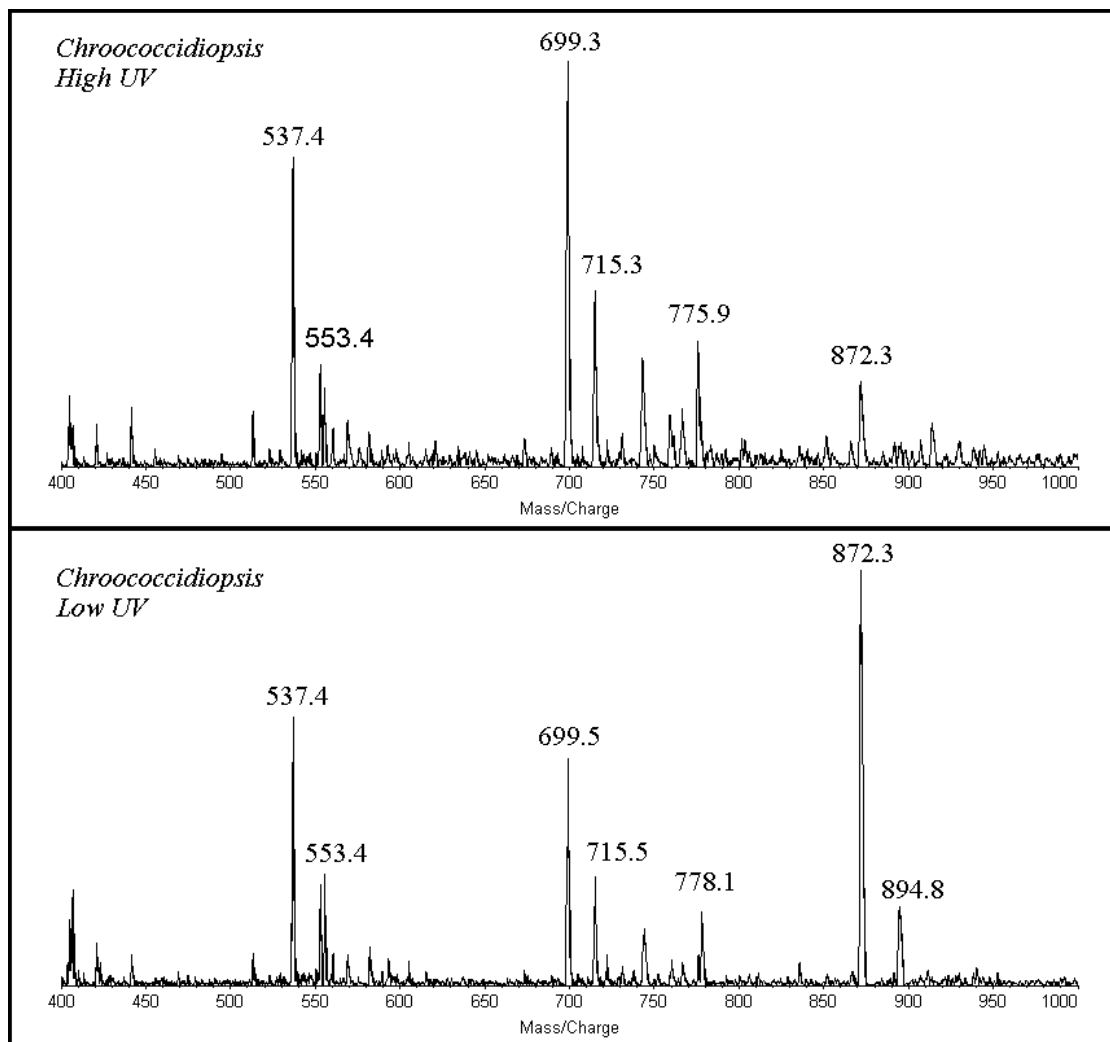


Figure 4.8 MALDI mass spectra of *Chroococidiopsis* grown under high and low UV light. This species is not expected to produce scytonemin because it is endolithic.

of the crusts is not known, but is assumed to be relatively high as the salt concentration in the lake is four to five times higher than the salt content of sea water. The results of extraction of two samples are shown in Figure 4.9. The predominant organism in each mat is indicated in the figure. The presence of scytonemin was confirmed in both samples.

Quantification of scytonemin is difficult because it is hard to generate calibration curves for MALDI-TOFMS analyses. The amount of analyte that is volatilized by the laser plume depends on the matrix-to-analyte ratio and the degree of heterogeneity in the distribution of the analyte in the matrix (which cannot be controlled). Furthermore, other compounds in the extract may affect ionization of scytonemin. It is well

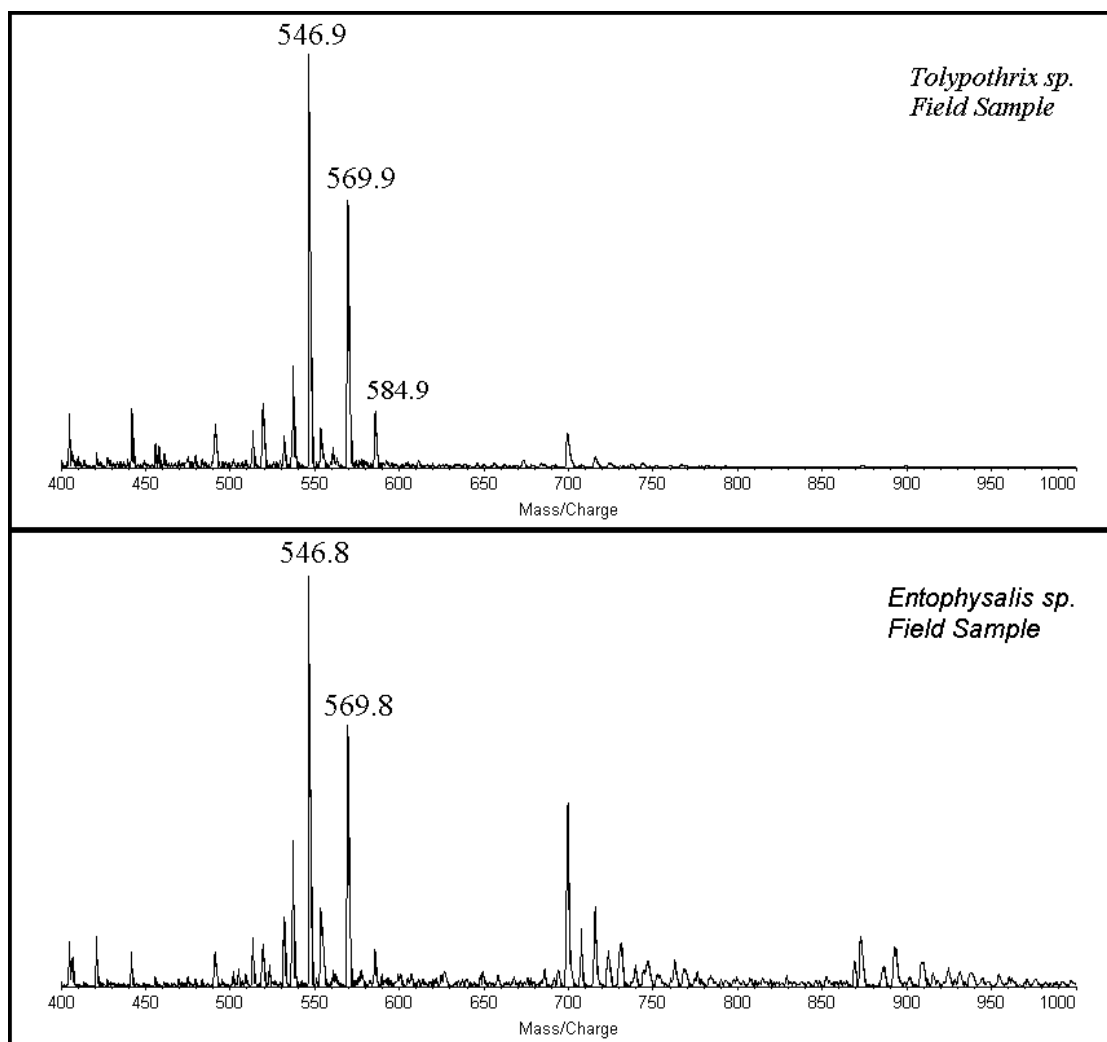


Figure 4.9 MALDI mass spectra resulting from the extraction of two cyanobacterial mats. The predominant organism in each mat is indicated. Peaks at 546.8, 569.8, and 584.9 Da represent scytonemin and the sodium and potassium adducts of scytonemin, respectively.

documented that ion-suppression occurs when multiple analytes are present.^{126,127}

Using pure scytonemin and keeping the matrix-to-analyte ratio constant, an appropriate, non-competitive internal standard could be added for peak ratio comparison. In this way it would be possible to generate a calibration curve. However, with field materials and lab cultures, there are too many unknown metabolites in addition to scytonemin. It would be possible to obtain a peak area or height for these samples, but since both the scytonemin-to-matrix ratio and the effect of other extracted compounds are not known, one cannot confidently relate the values to the calibration curve. Using serial dilutions of

pure scytonemin, the limit of detection was found to be in the picomole range (total amount applied to the MALDI plate), which corresponds to micromolar concentrations in the extract.

4.3.2 Whole Protein Analysis

The water stress protein of *N. commune* is believed to play an important role in desiccation tolerance. The amino acid sequence of Wsp has been determined, however its specific function is unknown.⁹⁸ Production and isolation of Wsp will lead to a better understanding of its role in desiccation tolerance. Because of the relatively slow growth rate of *N. commune*, Wsp is grown recombinantly in *E. coli*. The portion of DNA responsible for the production of Wsp in cyanobacteria is inserted into the plasmid of *E. coli* which then encodes for the production of the protein. The protein is excreted by *E. coli* and harvested from solution. During initial cloning experiments, an eight-amino-acid tag was added to Wsp as a flag sequence to facilitate identification of the protein.¹²⁸ Subsequently, experiments were developed that did not require the amino acid tag which led to the direct production of Wsp. Once the protein is produced and excreted by *E. coli* the supernatant is collected, concentrated, and Wsp is purified using ion-exchange liquid chromatography.

MALDI-TOFMS was used to identify purified Wsp with and without the amino acid tag. Studies were also conducted to assess the best matrix and the most accurate calibration method. The two matrices used for the MALDI analysis were SA and HCCA. Figure 4.10 shows the results for the analysis of Wsp with the amino acid tag using each matrix. HCCA gives multiply charged ions with the $[M+2H]^{2+}$ ion being the most intense, while SA produces an intense molecular ion with an occasional peak for $[M+2H]^{2+}$. Others have observed this trend for a variety of proteins.²⁶ SA was used as the matrix for subsequent studies because the singly charged molecular ion provides straightforward interpretation of mass spectra.

A sample was prepared with Wsp and BSA (about 1 pmol of each deposited on the sample probe) to obtain accurate mass measurements for Wsp, using BSA as an internal standard for calibration. Three spectra were collected from three different sample preparations. Each spectrum was calibrated using the known mass values for

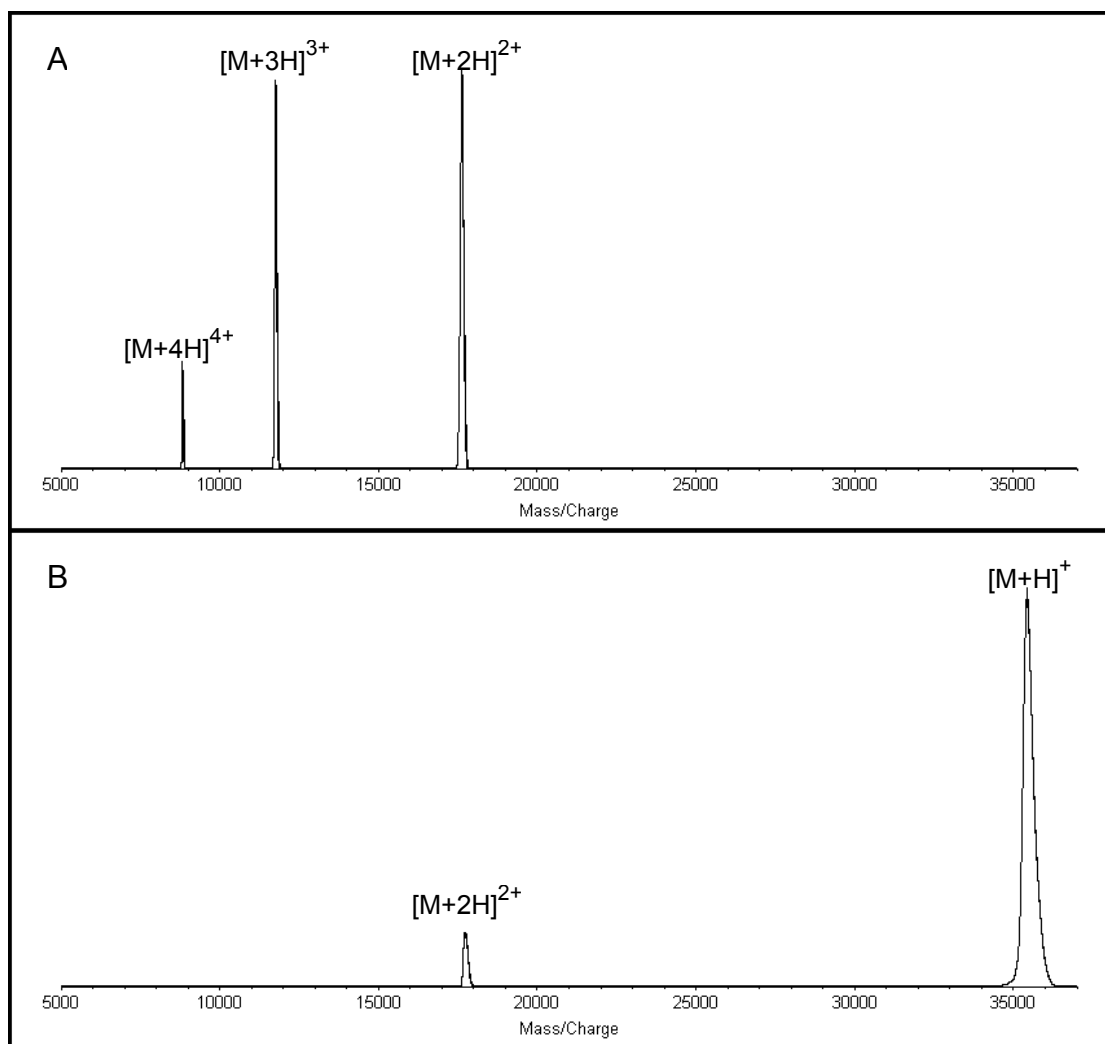


Figure 4.10 MALDI TOF mass spectra of Wsp using α -cyano-4-hydroxycinnamic acid (A) and sinapinic acid (B). Each matrix leads to a different series of charge states.

potassium and BSA (internal calibration). One of these internal calibrations was used to calibrate other mass spectra collected without BSA in the sample (external calibration). Mass spectra were also calibrated using the factory calibration for comparison with the other two methods. The mass accuracy results from the three different calibration methods are summarized in Table 4.1.

The mass accuracy for Wsp with the amino acid tag, even using internal calibration, is poor, especially considering the mass accuracy obtained for the other two samples using the factory calibration. The sample used for this analysis was purified using ion-exchange chromatography and the identity of the protein in this fraction was

Table 4.1 Illustration of the mass accuracy resulting from various calibration methods.

Analyte	Calibration Method	Observed Mass (Da)	Standard Deviation	Actual Mass (Da)	% Mass Accuracy
Wsp + AA Tag	Factory	35,683	46 (n = 8)	34,639	3.02
Wsp + AA Tag	External	35,451	29 (n = 5)	34,639	2.35
Wsp + AA Tag	Internal	35,512	34 (n = 3)	34,639	2.52
Wsp	Factory	33805	13 (n = 6)	33,644	0.48
Wsp	External	33607	13 (n = 6)	33,644	0.11
BSA	Factory	66818	20 (n = 3)	66,420	0.60
BSA	Internal	66430	0.26 (n = 3)	66,420	0.016

confirmed using SDS-PAGE only. The poor mass accuracy, along with the results from in-gel digestions (see Section 4.3.5), suggests that this protein is not Wsp. The observed mass is much closer to that of a protein produced by *E. coli*, glyceraldehyde-3-phosphate dehydrogenase A (GAPDH-A, 35,401 Da). In-gel digestion studies have shown that this protein is present in the supernatant (see below). It is possible the wrong fraction was collected after ion-exchange chromatography.

Wsp without the amino acid tag was desalted but not purified, therefore there is no possibility of collecting the wrong fraction. The factory calibration gives a mass accuracy of about 0.4% for BSA and Wsp, thus further confirming that the protein observed at 35,500 Da is not Wsp with the tag. The mass accuracy for Wsp is improved by a factor of 4 when calibrated externally. It is difficult to assess the improvement in mass accuracy using internal calibration because of the unknown identity of the protein at 35.5 kDa.

4.3.3 Peptide Mass Fingerprinting

Bovine serum albumin was used as a model protein to test the reliability of the in-gel digestion protocol and of the mass spectrometric results. BSA is commonly used as a standard to judge instrument and method performance because the amino acid sequence is known and it is commercially available. Because trypsin undergoes autolysis, it is also necessary to digest a gel piece that does not contain protein (a blank). The control experiment will identify peaks in the mass spectrum that result from

the autolysis of trypsin. Peaks that are seen in the blank spectrum are marked with an asterisk. The most useful mass range for peptide mass fingerprint analysis is from 800 to 3000 Da. Matrix peaks are commonly observed below 800 Da and peptides above 3000 Da are rarely observed in MALDI-TOFMS.

The MALDI-TOFMS results of an in-gel trypsin digest of BSA are shown in Figure 4.11. The spectra in Figure 4.11A and B were collected using sinapinic acid and α -cyano-4-hydroxycinnamic acid as the matrix (respectively). Sinapinic acid shows a tendency to ionize larger peptides. The mass list in each spectrum, with the exception of the peaks resulting from trypsin, was used to search for a protein match using a web-based search engine.¹¹⁵ The search was restricted to bovine proteins with a molecular weight of $66,000 \pm 10\%$, a mass accuracy of ± 0.5 Da, peptide fragments with up to one missed cleavage with trypsin as the protease, and a minimum of four peptide matches for protein identification. These types of restrictions are also reasonable for the identification of unknown proteins since the species is known and an approximate molecular weight is obtained from SDS-PAGE. Both searches returned BSA as the only protein match, with the SA spectrum matching 5 peptides and the HCCA spectrum matching 9 peptides. The peptide mass fingerprint using HCCA covers 18.7% of the amino acid sequence of BSA, compared to 12.7% sequence coverage using SA as the matrix. HCCA provides more peptide masses that represent BSA and is therefore a better matrix for peptide analysis. Current literature also concludes that HCCA is a better matrix for peptide analysis.²⁶

Table 4.2 shows the difference between the observed mass, using the factory calibration, and the true (monoisotopic) mass for the matching peptides in the HCCA spectrum. Inspection of the mass differences reveals that all of the matches were slightly lower than the actual masses. This observation suggests that the calibration curve should be shifted upward. There were also several peaks that were just outside the ± 0.5 Da search restriction (1163.63 and 1567.15 Da). Also shown in Table 4.2 are the mass accuracy values for the peptide matches using the factory calibration. The average mass difference was used to adjust the mass values (corrected calibration). The results of the corrected calibration show two peaks at 1163 and 1567 Da within the

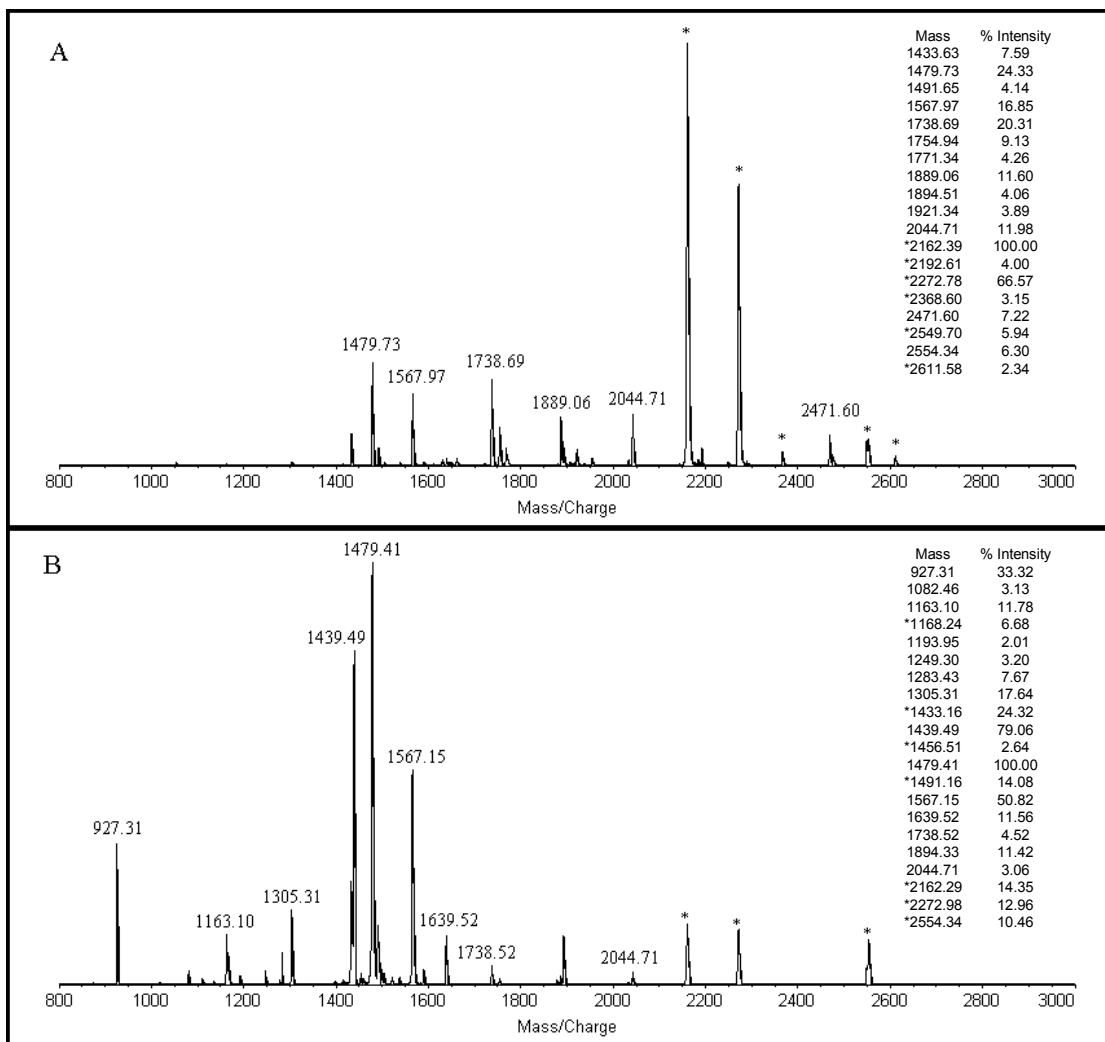


Figure 4.11 Peptide mass fingerprint of BSA using sinapinic acid (A) and α -cyano-4-hydroxycinnamic acid (B) as the matrix. Asterisks indicate peaks due to peptides resulting from the autolysis of trypsin. Labeled peaks show peptides of BSA.

± 0.5 Da mass accuracy range and a four-fold increase in the overall mass accuracy.

The identification of two additional peptides increases the sequence coverage to 22.6%.

Another database search was conducted using the 11 peptides identified from BSA with no species or molecular weight restrictions. BSA was listed first out of 107 proteins and all other matches showed a maximum of 5 peptide matches. These search results show the reliability of protein identification when the number of peptide matches is high (greater than 6).

Table 4.2 Observed peptide masses for BSA using the factory calibration and the associated mass accuracy. Corrected masses were obtained by adding the average mass difference to the factory calibrated mass value. The mass accuracy is improved by a factor of 4.

Factory Calibration	True Mass	Mass Difference	Mass Accuracy (ppm)	Corrected Calibration	Mass Difference	Mass Accuracy (ppm)
927.31	927.49	0.18	194	927.68	-0.19	203
1163.10	1163.63	0.53	455	1163.47	0.16	139
1249.30	1249.62	0.32	256	1249.67	-0.05	39
1283.43	1283.71	0.28	218	1283.80	-0.09	69
1305.31	1305.72	0.41	314	1305.68	0.04	32
1439.49	1439.81	0.32	222	1439.86	-0.05	33
1479.41	1479.80	0.39	264	1479.78	0.02	15
1567.15	1567.74	0.59	376	1567.52	0.22	142
1639.52	1639.94	0.42	256	1639.89	0.05	32
1738.52	1738.81	0.29	167	1738.89	-0.08	45
2044.71	2045.03	0.32	156	2045.08	-0.05	24
	Average =	0.37	262	Average =	0.00	70

After establishing that the in-gel digestion protocol is effective and that HCCA is the best matrix, in-gel digestion experiments were conducted to investigate Wsp. SDS-PAGE gels were run using the fractions collected after ion-exchange chromatography. Preliminary identification of Wsp is accomplished using molecular weight markers in one lane of the SDS-PAGE gel. Further confirmation is achieved by a Western blot, where Wsp has specific reactions with a series of antibodies. Prior to using peptide mass fingerprinting, SDS-PAGE and a Western blot were considered a positive identification of Wsp. Fractions containing Wsp were then pooled and biochemical assays were conducted to assess the function of the protein.¹²¹

In-gel trypsin digestion with subsequent MALDI-TOFMS analysis was used to further confirm the presence of Wsp in the ion-exchange fractions. The top two images in Figure 4.12 show the SDS-PAGE gel with all 14 fractions from the ion-exchange column, one fraction collected every two minutes, and the starting material (supernatant) prior to separation. The bottom images are the Western blot membranes, derived from the SDS-PAGE gels, showing the positive reaction with a series of antibodies at the molecular weight of Wsp. A fraction was chosen from the gel that appeared to be Wsp, similar to the band in fraction 7, and subjected to further

purification using a dye-affinity column. The fractions from this column were analyzed by SDS-PAGE and the band at 35 kDa was subjected to an in-gel digestion.

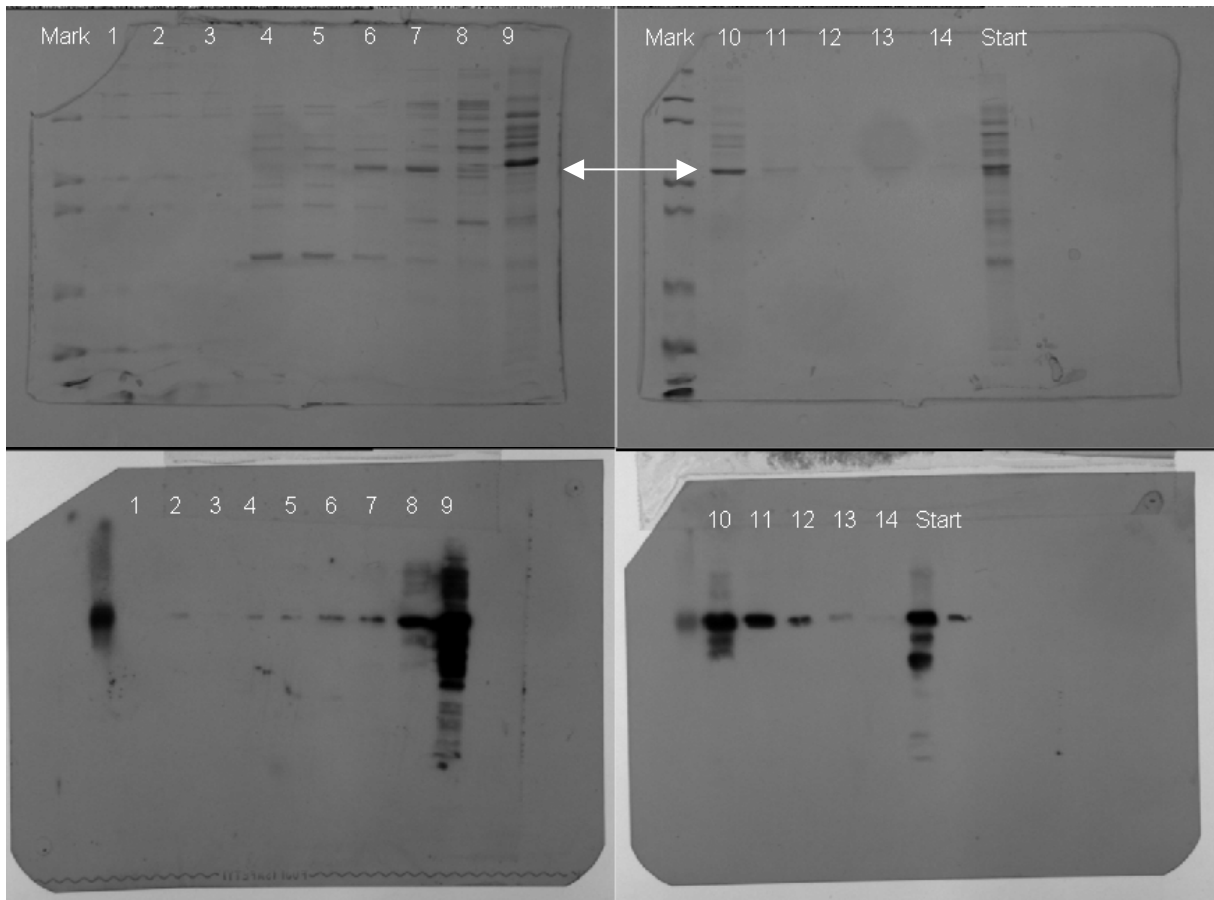


Figure 4.12 Top two images show SDS-PAGE gels of 14 fractions collected from ion-exchange chromatography of the supernatant. The first lane of each gel contains molecular weight markers and the last lane in the upper right hand image shows the supernatant. The lower images are Western blots of the two gels showing immunoreponse for proteins believed to be Wsp.

The resulting peptide mass fingerprint did not match the fingerprint expected for Wsp. The mass peaks from this spectrum, excluding those due to autolysis of trypsin, were used to search for a match in the Swiss-Prot database. The search was limited to *E. coli* proteins with a molecular weight of 35 kDa \pm 10%. The search returned only one result with 13 peptide matches covering 54% of the amino acid sequence (see Figure 4.13). The protein was identified as outer membrane protein F (OmpF), with a molecular weight of 37 kDa. It is evident that this protein cross-reacts with the antibodies used in the Western blot analysis, thus giving a false-positive identification of Wsp. From this example it is clear that SDS-PAGE and Western blot analysis cannot unequivocally

identify a protein in all instances. It was assumed that the wrong fraction was collected from the ion-exchange column for further purification.

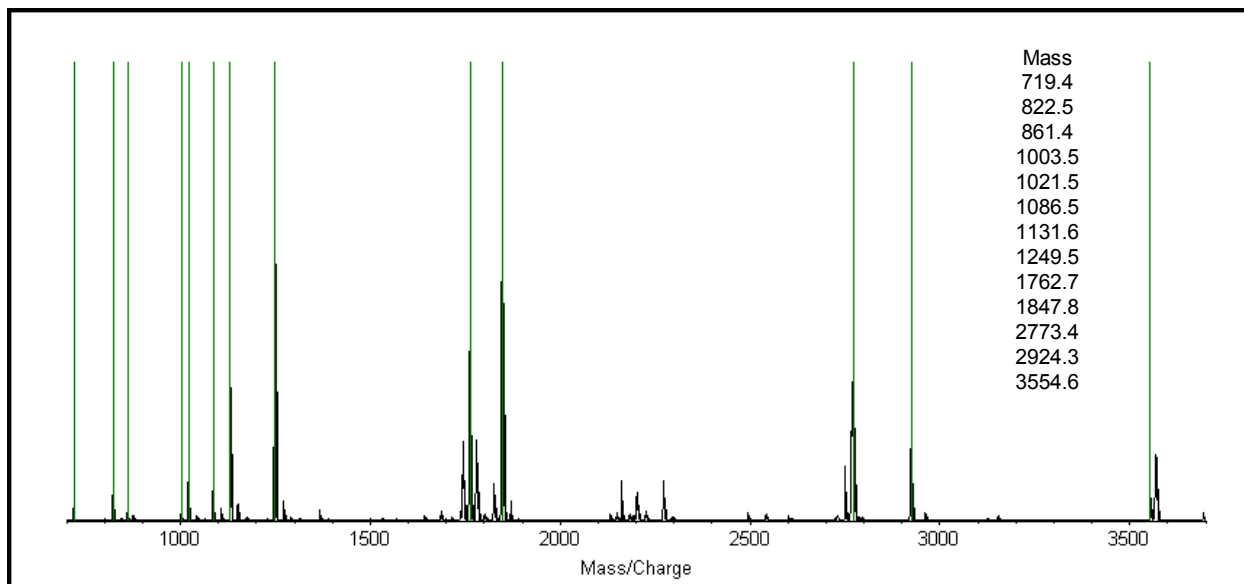


Figure 4.13 Peptide mass fingerprint of OmpF resulting in 54% of the amino acid sequence detected. The peak markers and the mass list represent peptides belonging to OmpF.

Gel bands from other fractions eluted from the ion-exchange column were investigated by peptide mass fingerprinting to locate Wsp. Two more *E. coli* proteins with molecular weights in the 35-kDa range were identified Figure 4.14 shows two SDS-PAGE gel images of fractions collected every two minutes from the ion-exchange column. The two gels result from two separations with different elution gradients. The first 35-kDa protein shows up in the fifth fraction and since the peptide mass fingerprint for this band did not match Wsp the mass values were used to search the Swiss-Prot database for *E. coli* proteins. Ten of the masses matched peptides that make up GAPDH-A, which corresponds to 44% of the amino acid sequence (see Figure 4.15). Low intensity peaks that correspond to Wsp peptides can sometimes be seen in this fraction (Figure 4.14A). Fraction six showed the presence of the third *E. coli* protein, which was identified as cysteine synthase A (CSASE-A, 34 kDa) with 18% amino acid coverage (see Figure 4.16). This was the only *E. coli* protein match returned from the Swiss-Prot search even though only four peptides were detected. CSASE-A was not always detected and it seems that the elution gradient has an effect of the presence of this protein, as indicated in Figure 4.14A. Gel bands from fractions 7-9 show the

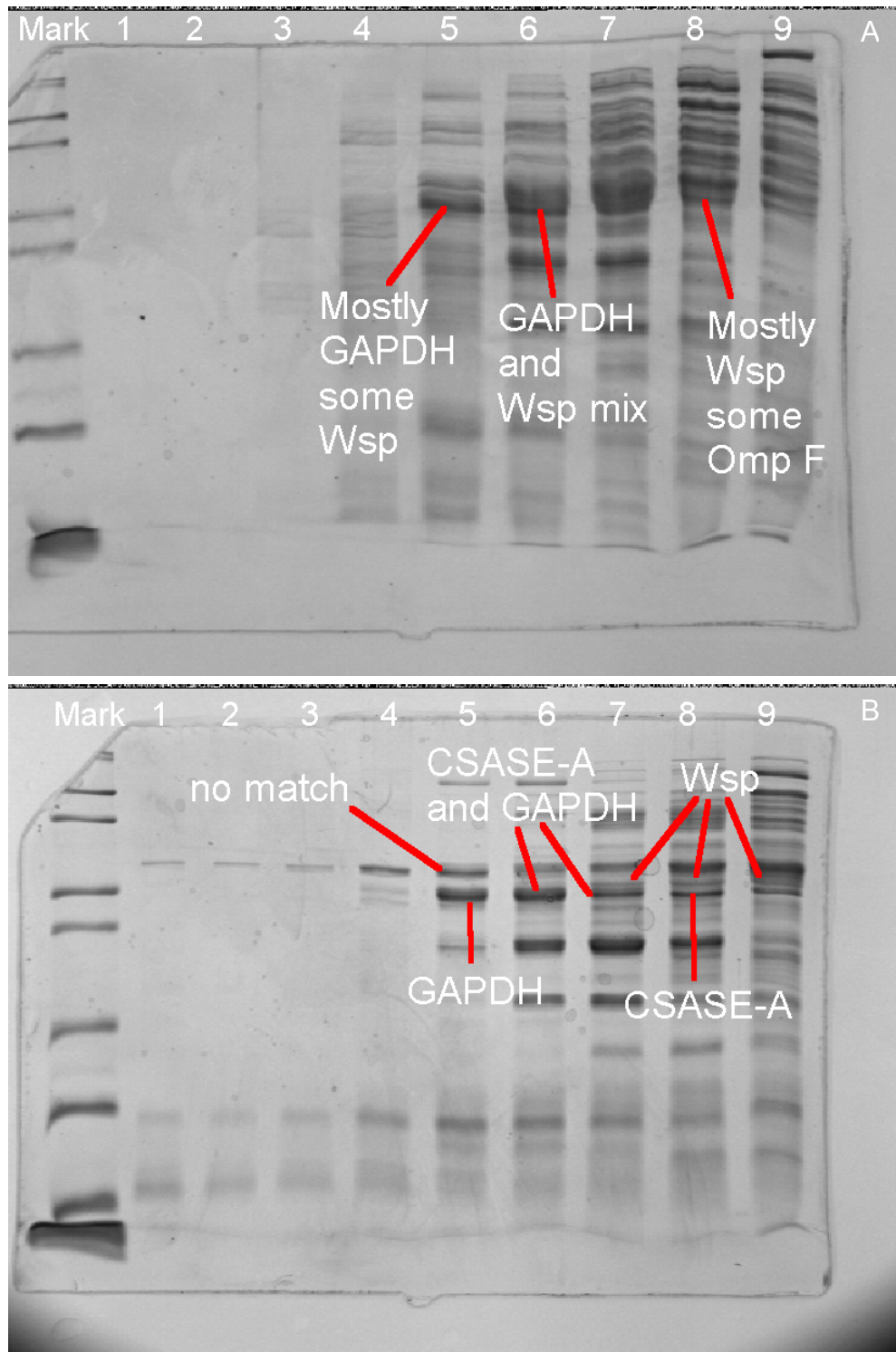


Figure 4.14 Gel images showing fractions from two different ion-exchange separations using TRIS as the buffer. Three *E.coli* proteins were identified in the same molecular weight range as Wsp. The fractions are numbered in order of elution.

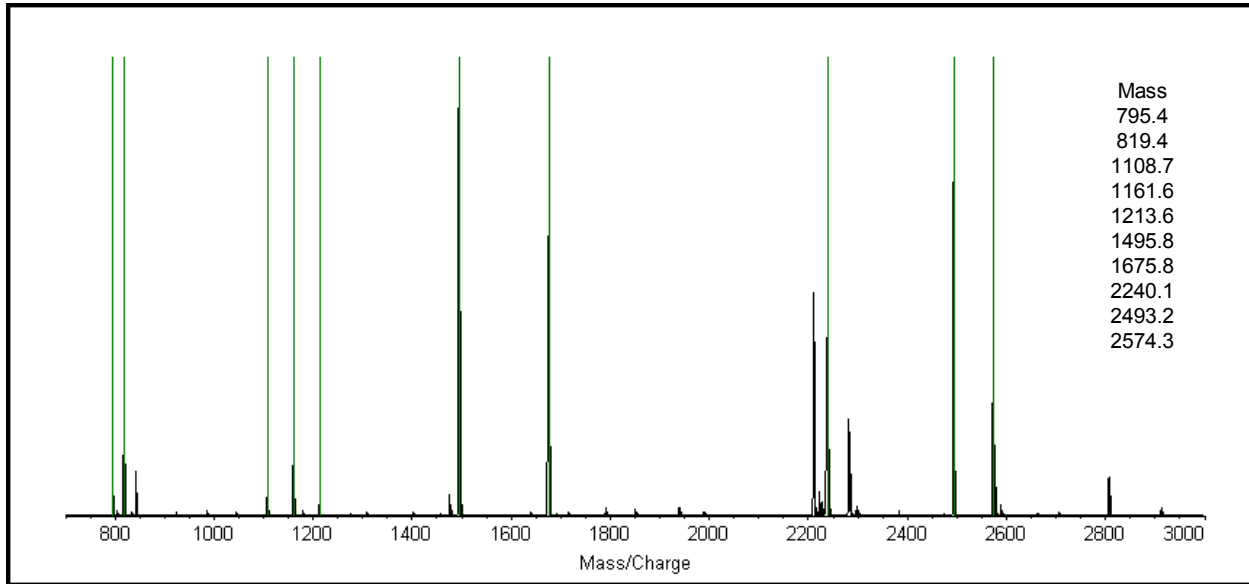


Figure 4.15 Peptide mass fingerprint of GAPDH-A representing 44% amino acid coverage. The peak markers and mass list pertain to GAPDH-A peptides.

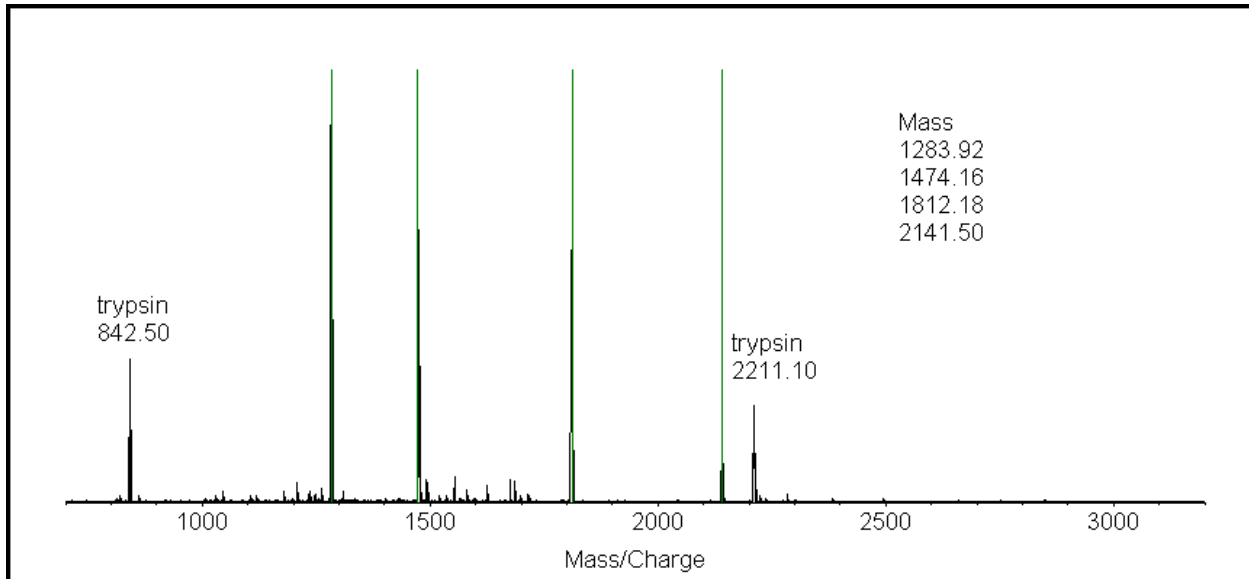


Figure 4.16 Peptide mass fingerprint of CSASE-A representing 19% amino acid coverage. The peak markers and mass list pertain to CSASE-A peptides. Trypsin peptide peaks were used for internal calibration.

presence of Wsp. Figure 4.17 shows a typical peptide mass fingerprint observed for Wsp, which gives 25% sequence coverage. Eight of the commonly observed peptide masses for Wsp were used to search the Swiss-Prot database for a match with *E. coli*

proteins and no matches were found. This search further confirms that the peptide mass fingerprint belongs to Wsp. Fraction 9 also shows the presence of OmpF as indicated in Figure 4.14A. Therefore, the elution order when TRIS is used as a buffer is GAPDH-A, Wsp, OmpF.

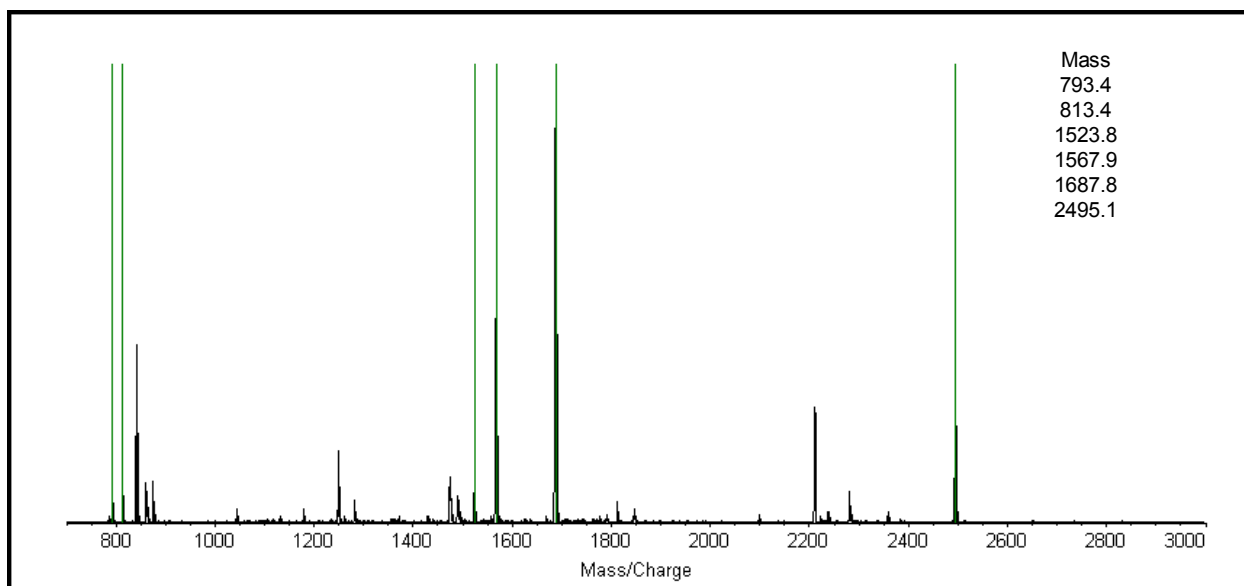


Figure 4.17 Peptide mass fingerprint of Wsp representing 26% amino acid coverage. The mass values were searched against *E. coli* proteins and no results were returned. The peak markers and mass list pertain to Wsp peptides.

A culture of *E. coli* was grown that did not have the plasmid that is responsible for Wsp production. The supernatant from this control culture was studied in order to confirm that the peptide mass fingerprint thought to belong to Wsp is not the result of an *E. coli* protein. A culture that was encoded for the production of Wsp was also grown. Aliquots of the supernatant from each culture were subjected to SDS-PAGE after being concentrated using a rotary evaporator. The band at 35 kDa was excised and subjected to an in-gel digestion. The resulting peptide mass fingerprints shown in Figure 4.18 do show differences. The peptide mass fingerprint of the control culture shows the presence of OmpF only, while the Wsp clone shows the presence of OmpF and Wsp.

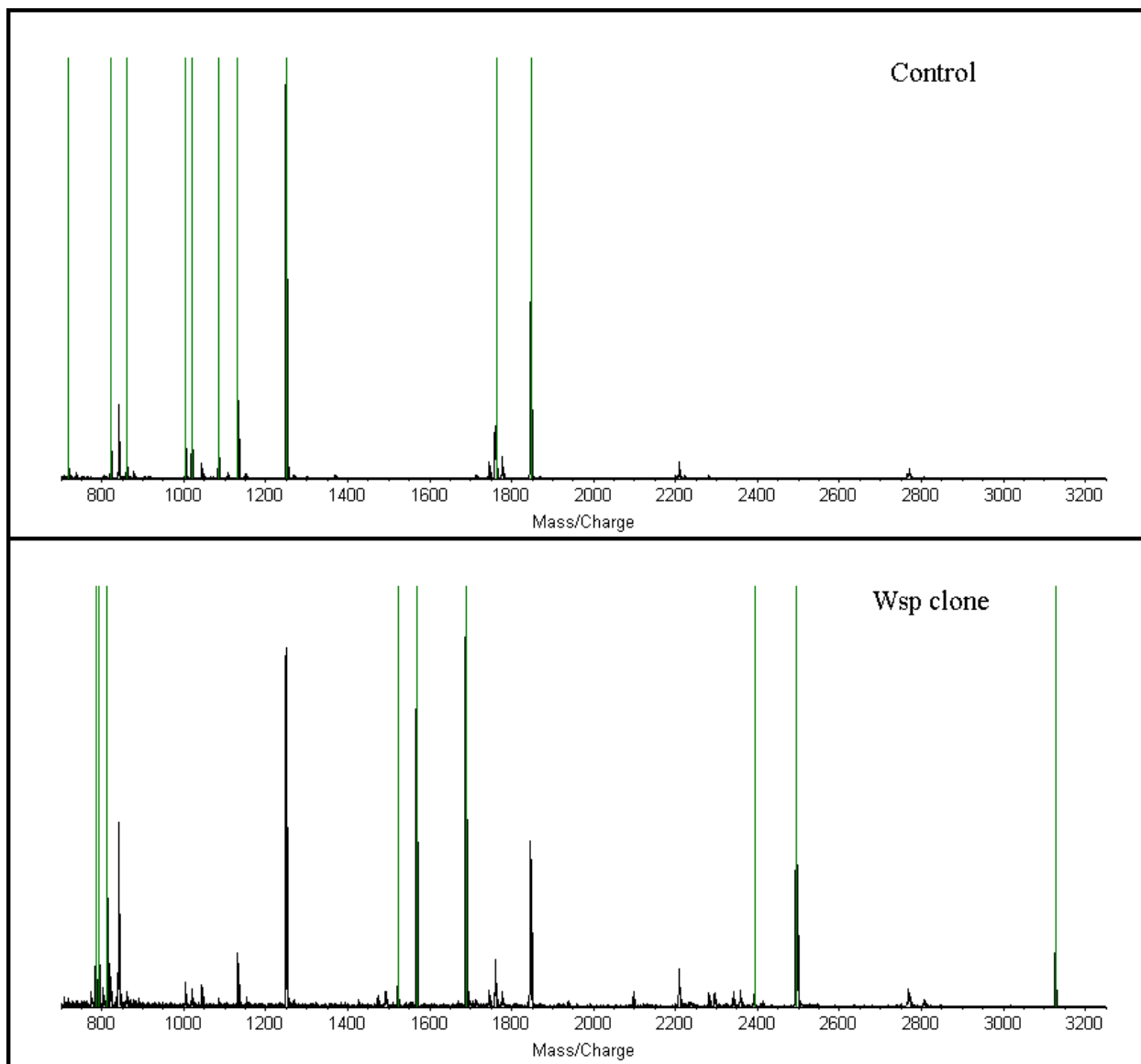


Figure 4.18 Peptide mass fingerprints of the supernatant from an *E. coli* culture (control) and an *E. coli* culture encoded to produce Wsp (Wsp clone). Peak markers show the presence of OmpF (control) and Wsp (Wsp clone).

Several more experiments were conducted with the supernatant prior to ion-exchange chromatography. The goal was to perform a time-course study of Wsp expression versus *E. coli* protein expression in a culture encoded to produce Wsp. Protein expression was initially measured using a Bradford's test, which uses UV absorbance as a measure of total protein concentration. In this manner the maximum protein expression was measured after a period of about 24 hours.¹²¹ Aliquots of the supernatant were taken at 0, 6, 19, 24, 29 and 48 hours which were then subjected to

SDS-PAGE (see Figure 4.19). Glucose was added to one of the cultures after 24 hours as a source of nutrition for *E. coli*. We made several noteworthy observations. First, there are no proteins excreted at time zero, as expected. Second, the total protein production and expression increases up to 24 hours as evidenced by the darkness of the bands. Finally, addition of glucose increases the total protein production and expression.

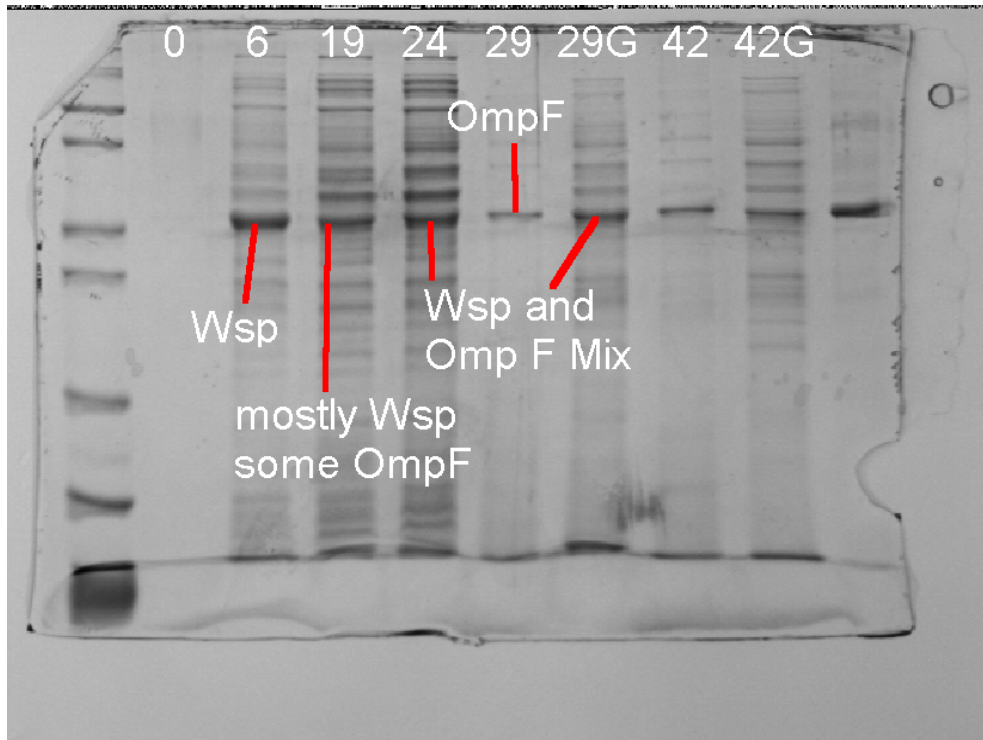


Figure 4.19 SDS-PAGE gel image of aliquots of the supernatant collected at the times indicated (in hours). Glucose (G) was added to one of the cultures after 24 hours and seems to facilitate protein production. OmpF excretion increases with time.

Peptide mass fingerprinting reveals several other trends, as seen in Figure 4.20. After six hours the majority of the protein expression is Wsp as evidenced by the mass spectrum. The three peaks that match peptides from OmpF (O) are low in intensity, relative to those of Wsp (W). At nineteen hours there is more OmpF present in the supernatant, as evidenced by the relative increase in intensity for OmpF peptide peaks, and after 24 hours there is even more OmpF present. After 29 hours, when no glucose is present, the peptide mass fingerprint shows no peaks corresponding to peptides of Wsp. When glucose is added the peptide mass fingerprint is similar to that observed

after 24 hours. The addition of glucose seems to provide a source of energy so that *E. coli* can continue to produce Wsp.

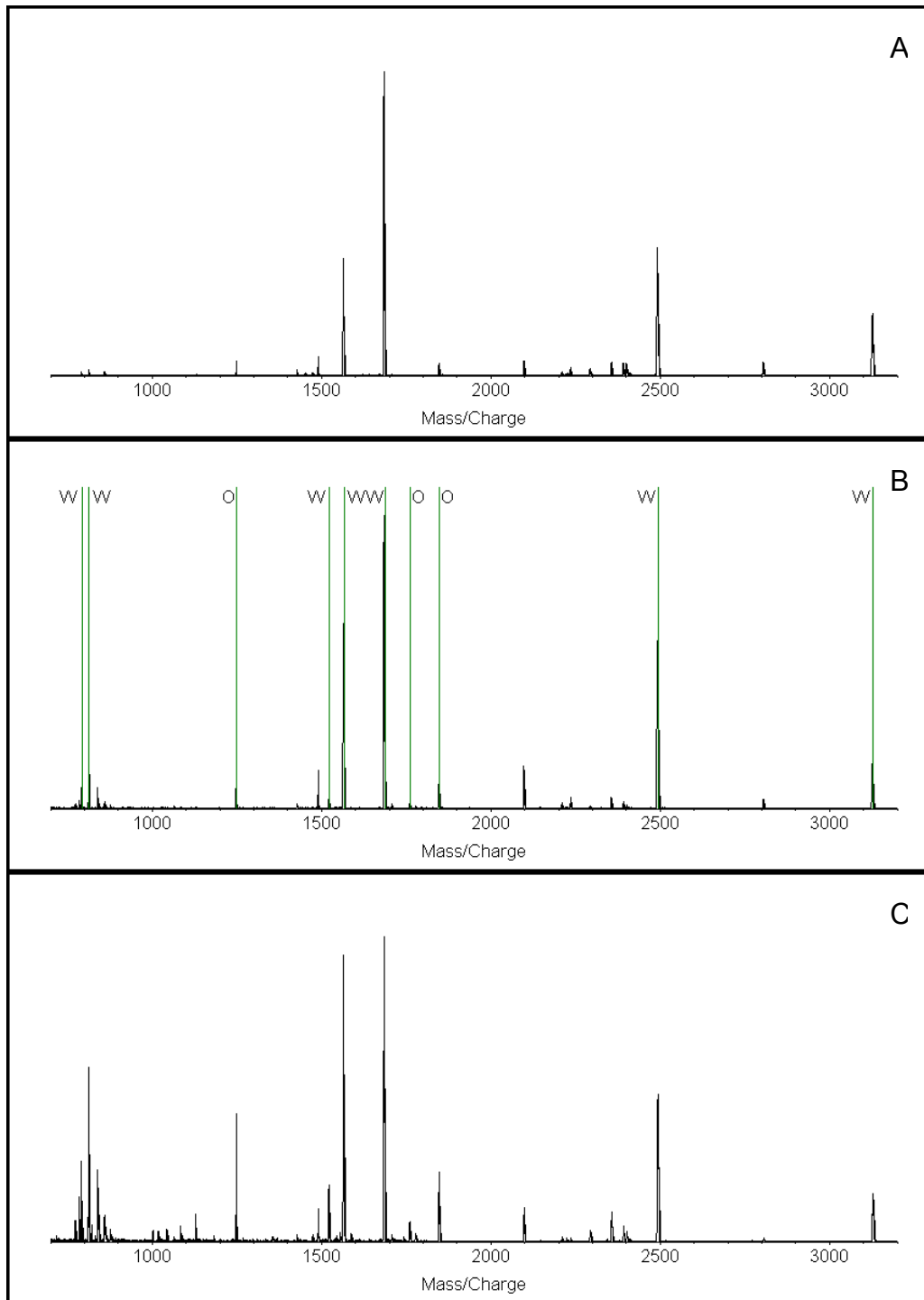


Figure 4.20 Peptide mass fingerprints from gel bands of material collected at 6 (A), 19 (B), and 24 (C) hours. Peak markers in spectrum B indicate OmpF (O) and Wsp (W) peptides. The production of OmpF increases with time as seen by the relative increase in peak intensity for OmpF peptides.

Another set of experiments was used to study the long-term stability of the *E. coli* clone. An SDS-PAGE gel was run on the supernatant prior to purification after every new batch of Wsp was produced over the course of about six months. The supernatant from the initial experiment was collected after 24-hour growth period.¹²¹ The band from the SDS-PAGE gel corresponding to the molecular weight of Wsp was excised and digested. The resulting peptide mass fingerprint is shown in Figure 4.21. The spectrum consists mostly of Wsp peptides, with two low intensity peaks for OmpF (1249 and 1848 Da). The spectrum shown in Figure 4.20C is a result of Wsp that was produced six months after the development of the clone. Comparison of Figure 4.21 and Figure 4.20C shows that the expression of OmpF has increased over a six-month period and suggests that the clone may be evolving.

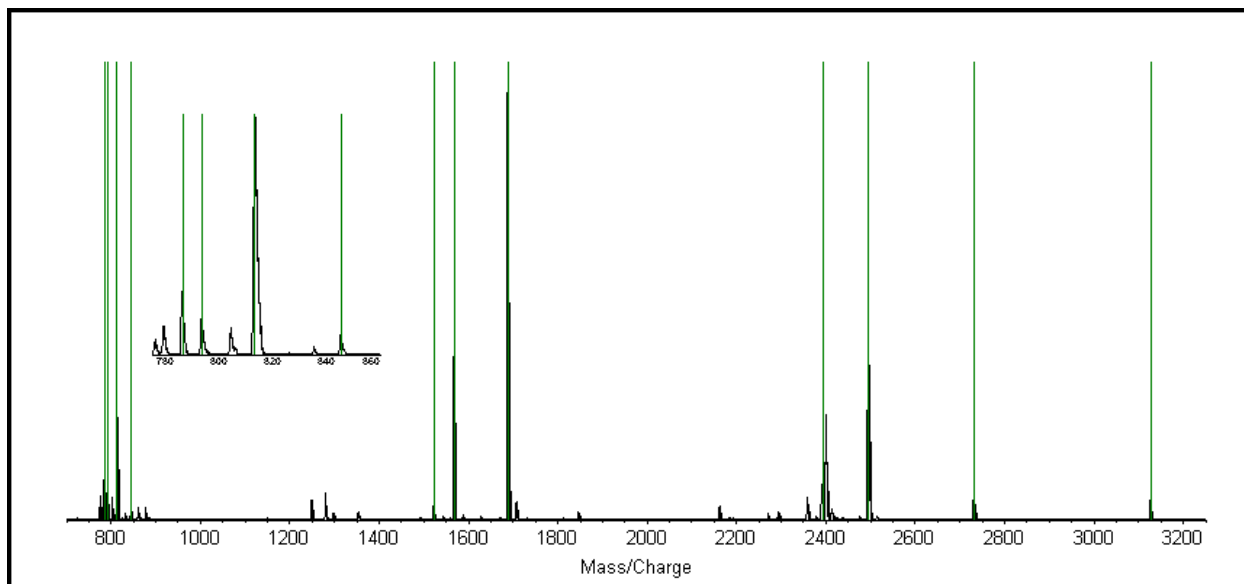


Figure 4.21 Peptide mass fingerprint of supernatant right after clone was developed. Peak markers show peptides from Wsp. The inset is an expansion of the 760 to 860 Da mass range.

4.4 Conclusions

4.4.1 Scytonemin Screening

Typical methods for scytonemin analysis are based upon UV absorbance,^{108,109} HPLC,¹⁰⁵ and more recently Raman spectroscopy.¹²⁹ While spectrophotometric methods are rapid, they do not provide unambiguous evidence for the presence of

scytonemin. The HPLC method can provide reliable quantitative data but is a relatively lengthy procedure (several days), especially if one is mostly interested only in the presence or absence of the molecule.

The MALDI-TOFMS screening method is a quick and semiquantitative way to assess the presence or absence of scytonemin in both field- and laboratory-grown cultures of cyanobacteria. It is demonstrated that a simple solvent extraction and subsequent MALDI-TOFMS analysis can be used as a screening method for the presence of scytonemin. Because the time required for extraction and analysis are minimal (less than thirty minutes), this method is useful for the assessment of UV radiation stress and molecular ecology studies of cyanobacteria.

Future experiments will use the screening method to facilitate proteomics studies of cyanobacteria. Cultures will be grown under different amounts of UV exposure and tested for the production of scytonemin. The biosynthesis of scytonemin indicates the organism is under UV-induced stress. Two dimensional gel electrophoresis and peptide mass fingerprinting to identify the proteins expressed in higher amounts due to the UV stress can then assess differences between the cultures. These studies will lead to a better understanding of the function of specific proteins in the UV stress response.

4.4.2 Protein Analysis and Peptide Mass Fingerprinting

MALDI-TOFMS is a valuable tool for the analysis and identification of proteins. Whole protein analysis using MALDI leads to a more accurate molecular weight determination than SDS-PAGE and better resolution of protein mixtures. However, MALDI is not meant to replace SDS-PAGE, but rather to complement it. In fact, SDS-PAGE helps reduce salt and buffer contamination when analyzing the supernatant and therefore facilitates successful MALDI results.

Peptide mass fingerprinting revealed that SDS-PAGE and Western blot techniques are not always sufficient for protein identification. Three *E. coli* proteins in the 35-kDa range were identified using peptide mass fingerprinting and database searches. These proteins were shown to co-elute with Wsp during ion-exchange chromatography. These results show that peptide mass fingerprinting is required to monitor the purification of Wsp.

Time course studies of protein production in recombinant *E. coli* using peptide mass fingerprinting revealed that it is best to harvest Wsp between six and ten hours after induction. The results are not quantitative, so it is difficult to say how much Wsp is being produced as a function of time. However, it is shown that OmpF contamination increases with growth time. Total protein production increases for periods up to 24 hours, but at the cost of Wsp purity. The addition of glucose to cultures facilitates the production of Wsp. Cultures without glucose stopped producing Wsp after 29 hours, while those with glucose continued to produce Wsp. Presumably, glucose provides *E. coli* with the energy needed to maintain protein production. The addition of glucose to the culture during growth may also provide increased levels of Wsp and lower levels of OmpF.

Mass spectral analysis of supernatant collected when the clone was developed versus supernatant collected six months later suggests that the clone may be modified. In each case the supernatant was collected after a 24-hour period, however the six-month-old clone shows a more dominant presence of OmpF. It is possible that the clone is evolving to reject the DNA inserted into its plasmid and therefore showing reduced amounts of Wsp.

4.4.3 Future Experiments

Our results show the utility of MALDI-TOFMS for the study of cyanobacteria. However, there are many more possibilities yet to be explored. Several of the future experiments are discussed here.

Glycosyl transferases are enzymes produced by cyanobacteria that are believed to play an important role in the synthesis of the EPS. The absolute function of glycosyl transferases is unknown but they are believed to add specific mono- and disaccharides to the growing polysaccharide.¹²⁸ Experiments have been designed to test the function of glycosyl transferases in a controlled system. The goal of the project is to identify the operon (gene cluster) for polysaccharide biosynthesis by determining function and amino acid sequence of glycosyl transferases and then working back to the genetic information.¹²⁸ Once the operon has been determined it can be placed in another organism, such as *E. coli*, in order to study desiccation tolerance in recombinant

organisms. The experimental approach is summarized in Figure 4.22. A fluorescent tag (FCHASE) is attached to the “acceptor” sugar to facilitate detection of the products. The donor and acceptor sugars are then placed in a reaction vial in the presence of a glycosyl transferase which should lead to the covalent attachment of the donor and acceptor. The reaction product(s) can be separated by capillary electrophoresis with laser-induced fluorescence detection or by thin layer chromatography. The separated products can then be subjected to MALDI-TOFMS for confirmation of the structure. If multiple donor sugars are used, MALDI will determine which sugars are being added to the acceptor. In this way MALDI will help determine the function of glycosyl transferases.

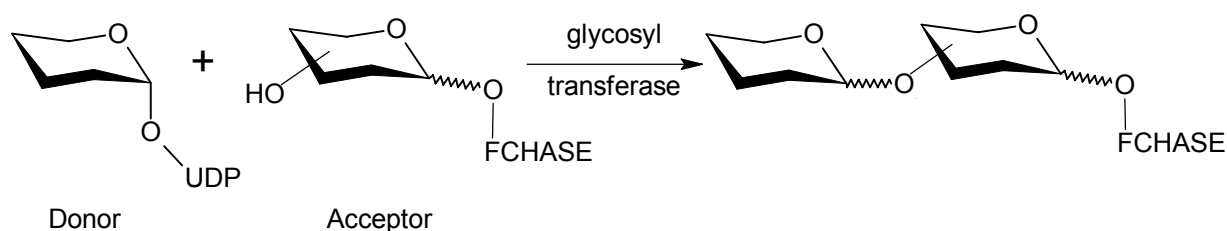


Figure 4.22 Reaction scheme to determine the activity of glycosyl transferases.

The component sugars of the EPS of *N. commune* have been determined by performing an acid hydrolysis with subsequent carbohydrate analysis.⁹¹ The EPS consists of glucose, galactose, glucosamine, galactosamine, mannose, and N-acetyl galactosamine. However, these studies were not able to determine the chemical composition of the polymeric chain. MALDI-TOFMS, with subsequent PSD analysis, could be used to further characterize the exact composition of the EPS by analysis of hydrolysis products. Thus, MALDI could help identify the exact polymeric structure of the EPS of cyanobacteria.

Chapter 5 – Summary

The research presented here demonstrates the utility of MALDI-TOFMS in the study of different classes of compounds over a broad range of molecular weights. Mass spectrometric data provides information for the identification and characterization of compounds that is not attainable with other analytical techniques. The role of mass spectrometry has evolved beyond being a traditional analytical chemist's tool and mass spectrometers are now commonly found in biochemical and biological laboratories. The popularity of mass spectrometry is largely due to the discovery of soft ionization techniques, such as MALDI and ESI, and the availability of commercial instruments that are designed for automated, high-throughput analysis.

MALDI-TOFMS analysis of inorganic coordination complexes, as presented in chapter 3, allows for the structural characterization of polymetallic compounds. As is typical with most MALDI experiments, the choice of matrix and matrix-to-analyte ratio are important to the success of the method. To my knowledge there are no reports in the literature that investigate the sample preparation conditions for successful analysis of inorganic coordination compounds.

The interpretation of the results presented in Tables 3.2 and 3.3 along with the future experiments suggested may lead to a better understanding of ionization mechanisms in MALDI and plume dynamics (reduction potential, thermodynamics, etc.). The proposed ionization mechanism is as follows. Various numbers of counter ions (PF_6) are lost during desorption, due to fragmentation. Collisions with matrix neutrals and or acquisition of free electrons then leads to reduction of the metal complex (based on the bridging ligands) and formation of singly charged pseudomolecular ions. The differences in the $[\text{M}-n(\text{PF}_6)]$ peaks observed are due to the differences in the redox chemistry of the complexes. So, in theory there is a "reduction potential" associated with the MALDI plume. For the matrices that produced the $[\text{M}-n(\text{PF}_6)]$ series the "reduction potential" would be the same, as the $[\text{M}-n(\text{PF}_6)]$ series for a given complex did not change for successful matrices. Future experiments will help determine the reduction potential by investigating a new series of polymetallic complexes with different redox chemistries. There is no information in the current literature in regards to the observations above.

The MALDI-TOFMS screening method allows for a rapid determination of the presence or absence of scytonemin. The biggest advantage of the MALDI screening method is that extraction and analysis can be done in about thirty minutes and multiple samples can be analyzed in parallel. This method will find use in molecular ecology studies of cyanobacteria. The presence of scytonemin is a biomarker that indicates the amount of UV light the organism has been subjected to and therefore acts as a measure of UV-induced stress. One can then assess the environment of field cultures and how that environment may be changing, for example if the organism grows in the shade or experiences an increase in UV-exposure due to ozone depletion.

MALDI-TOFMS also plays a vital role in the emerging field of proteomics. As demonstrated in chapter 4, MALDI offers the capability to analyze whole proteins and peptide fragments resulting from enzymatic digestion. Typical biochemical techniques, such as gel electrophoresis and Western blot analysis, were unable to detect the presence of contaminating *E. coli* proteins in fractions collected from an ion-exchange column. If the wrong fraction is collected from the ion-exchange column, further purification using a dye-affinity column will lead to the purification of the wrong protein. The presence of undetected *E. coli* proteins could lead to erroneous conclusions when performing biochemical assays to ascertain the role of Wsp in the desiccation tolerance of *N. commune*. Therefore, mass spectrometry proves to be an invaluable tool for monitoring the isolation and purification of the water stress protein and results suggest that purification methods need to be improved.

Long term studies of the clone by peptide mass fingerprinting also proved to be important. The results indicate that there is an increase in the amount of OmpF present in the supernatant six months after the clone was developed. It is not possible to ascertain whether the absolute concentration of Wsp has decreased, but relatively the excretion of OmpF has increased. The relative increase in the amount of OmpF in the supernatant suggests that the clone may have evolved of the six-month period. Results also suggest that cultures grown with glucose may increase the amount of Wsp produced by the recombinant organism.

Appendix A – Soil Digestion Protocol

(Modified from: EPA Method 200A)

Materials

2-3 grams of soil sample, air-dried and finely ground

Deionized water

6 M redistilled HCl

Concentrated HNO₃

100 mL round bottom flask

40 cm condenser

Heater with sand bath

Glass funnel

Acid-resistant cellulose filter paper (Whatman 541)

Procedure

1. Place approximately 3 g of air-dried, finely ground soil to a 100 mL round-bottom flask and add 2-3 mL of deionized water to form a slurry. Also, for each gram of soil, add 7.5 mL of 6 M redistilled HCl and 2.5 mL of concentrated HNO₃.

2. Gently reflux for 2 hours using a 40-cm condenser.

3. Allow the slurry to cool and rinse condenser with 20-30 mL of deionized water, collecting the water in the round bottom flask.

4. Filter the slurry through an acid-resistant cellulose filter. Repeat filtering until no particles are visible in solution. Collect the final filtrate in a 100 mL volumetric flask and fill to the mark with deionized water.

Appendix B – In-gel Digestion Protocol for MALDI-TOFMS Analysis of an SDS-PAGE Gel Separated, Coomassie-Stained Protein

(Adapted from: *Current Protocols in Protein Science*²⁷)

Materials

Stained polyacrylamide gel containing protein band of interest
25 mM ammonium bicarbonate (NH₄ HCO₃) /50% (v/v) acetonitrile
10 mM dithiothreitol (DTT) in 25 mM NH₄ HCO₃
55 mM iodoacetamide in 25 mM NH₄ HCO₃
25 mM NH₄ HCO₃ , pH 8
0.05 to 0.1 mg/mL trypsin (sequence grade; Promega, Pierce) in 25 mM NH₄ HCO₃ , pH 8
5% (v/v) trifluoroacetic acid (TFA)/50% (v/v) acetonitrile
0.5 mL tubes (e.g., VWR *SuperSlik*), silanized
Vacuum centrifuge
56°C water bath
Sonication bath

NOTE: To avoid or reduce contamination with human keratins, one should wear gloves and preferably work in a laminar flow hood.

Excise and wash gel fragments

1. Excise protein bands/spots of interest from a stained polyacrylamide gel. Cut each gel piece into small particles (~1 mm²) using a scalpel, and place into a 0.5 mL siliconized tube (VWR *SuperSlik* microcentrifuge tubes). Also cut out and dice a gel piece from a protein free region of the gel, for a parallel control digestion to identify trypsin autoproteolysis products.

The amount of protein loaded on the gel must be determined empirically as it depends on properties of the specific protein (for example, degree of hydrophobicity and size). In general, picomole levels are preferred to lower levels, although some reports claim that femtomole sensitivities are attainable with in-gel digestion and mass spectrometry. The small gel particle size facilitates the removal of SDS (and

Coomassie) during the washes, and improves enzyme access to the gel. For Coomassie stained proteins, one gel particle per tube is probably sufficient protein.

2. Add ~100 μ L of 25 mM NH_4HCO_3 /50% acetonitrile (or enough to immerse the gel particles) and vortex for 10 min. Use gel loading pipette tips to remove the solution (pale blue in the case of Coomassie staining) and discard. Repeat this wash/dehydration step up to ~3 times.

At this point, the gel slices shrink and can become white. This visual criterion should be used to determine whether or not additional washes should be performed.

3. Seal tubes and poke several holes in the caps with the aid of a sharp, pointed tool. Dry gel particles for ~30 min in a vacuum centrifuge.

Perform reduction and alkylation (optional)

4. Add enough 10 mM DTT solution to cover the gel pieces, and reduce for 1 hr at 56°C.

Steps 4 to 7 may be included when a maximum of protein coverage is required or when digesting a band from a one dimensional gel. Proteins separated by two dimensional gel electrophoresis are already reduced and alkylated, so these steps can be omitted

5. Cool to room temperature and replace the DTT solution with roughly the same volume of 55 mM iodoacetamide solution. Incubate for 45 min at room temperature in the dark with occasional vortexing.

6. Wash gel pieces (rehydrate) with ~100 μ L of 25 mM NH_4HCO_3 pH 8, for 10 min while vortexing, and dehydrate with ~100 μ L of 25 mM NH_4HCO_3 /50% acetonitrile. Repeat rehydration and dehydration.

7. Remove the liquid phase and dry the gel pieces in a vacuum centrifuge.

Digest protein sample

8. Rehydrate gel particles in 1 vol. of 0.05 to 0.1 mg/mL trypsin solution by vortexing for 5 min. Do not add more solution than can be absorbed by the gel particles.

The volume needed can be estimated by calculating the total gel volume excised (e.g., 2 mm x 8 mm x 1 mm = 16 mm³ = 16 μ L). The enzyme substrate ratio employed

for *in-gel* digestions (>1:10) is greater than for *in-solution* digestions due to hindered enzyme access to the protein substrate in the gel. Moreover, the relatively low salt concentration (25 mM) is needed to reduce the possibility of subsequent salt interference with ionization in the mass spectrometer.

9. If necessary, overlay the rehydrated gel particles with a minimum amount of 25 mM NH₄ HCO₃ to keep them immersed throughout digestion.

10. Incubate 12 to 16 hrs at 37°C.

Recover peptides

11. Add 2 vol. water, vortex for 5 min, and then sonicate for 5 min. Use a gel-loading tip to remove the peptide solution and transfer it to a silanized tube.

If yields are low, one can extract instead with 2 vol. saturated (~20 mg/mL) α -cyano-4-hydroxycinnamic acid. Shake gel pieces in this for 1-2 h, then remove liquid and let it air dry in a siliconized tube to ~5-10 μ L, then spot onto MALDI plate.

12. Perform two additional extractions using 2 vol. of 5% TFA/50% acetonitrile.

The silanized microcentrifuge tubes and the high TFA concentration are used to minimize adsorptive sample loss. Formic acid (5%) may be used as an alternative to TFA.

13. Concentrate recovered peptides by reducing the final volume of the extracts to ~10 μ L in a vacuum centrifuge. Bring to 25 μ L with 5% TFA/50% acetonitrile. Store the recovered peptides at -20°C until MALDI MS is performed.

Sample Preparation for MALDI Analysis

14. Prepare the matrix solution. The most successful matrix for peptide analysis is α -cyano-4-hydroxycinnamic acid (HCCA). For whole protein analysis *trans*-3,5-dimethoxy-4-hydroxycinnamic acid (sinapinic acid) is best. In either case, a saturated solution is prepared in 50% acetonitrile:0.1% TFA. Add a small amount of solid matrix (about the size of a BB) to an 0.6 mL Eppendorf tube. **Do not use siliconized tubes (i.e. the VWR SuperSlik tubes).** Add 30-50 μ L of 50% acetonitrile:0.1% TFA, vortex for 5 minutes, centrifuge for 1 minute.

15. Obtain a stainless steel sample plate and make sure it is clean. Plates can be cleaned with organic solvent (acetonitrile, methanol, etc..) and a Kimwipe. Repeat several times.

16. Using a gel loading tip, place 0.5 μL of the peptide/protein sample in one of the sample wells. Using a new tip, place 0.5 μL of matrix solution on top of peptide/protein solution. Mix by aspirating pipette several times. The sample will spread past the capacity of the sample well, just make sure that two consecutive preparations don't mix. Repeat for each sample.

17. Dry the droplets using a gentle stream of nitrogen. I usually prepare three droplets, then dry. Repeat for additional samples.

References

- ¹ Wiley, W. C.; McLaren, I. H. *Rev. Sci. Instrum.* **1955**, *26*, 1150-1157.
- ² Macfarlane, R. D.; Torgerson, D. F. *Int. J. Mass Spectrom.* **1976**, *21*, 81-86.
- ³ Brown, R. S.; Gilfrich, N.L. *Rapid Commun. Mass Spectrom.* **1992**, *6*, 697-701.
- ⁴ Brown, R. S., Utah State University, personal communication, **2000**.
- ⁵ Guilhaus, M. *J. Mass Spectrom.* **1995**, *30*, 1519-1532.
- ⁶ Beavis, R. C.; Chait, B. T. *Rapid Commun. Mass Spectrom.* **1989**, *3*, 233-239.
- ⁷ Schriemer, D. C.; Li, L. *Anal. Chem.* **1996**, *68*, 2721-2725.
- ⁸ Cotter, R.J. *Biomed. Environ. Mass Spectrom.* **1989**, *18*, 513-532.
- ⁹ Brown, R. S.; Lennon, J. J. *Anal. Chem.* **1995**, *67*, 1998-2003.
- ¹⁰ Mamyrin, B. A.; Karatajev, V. J.; Shmikk, D. V.; Zagulin, V. A. *Sov. Phys. JETP* **1973**, *37*, 45-52.
- ¹¹ Mamyrin, B. A. *Int. J. Mass Spectrom. Ion Proc.* **1994**, *131*, 1-19.
- ¹² Bergmann, T.; Martin, T. P.; Schaber, H. *Rev. Sci. Instrum.* **1989**, *60*, 347-349.
- ¹³ Tang, X.; Beavis, R.; Ens, W.; Lafortune, F.; Schueler, B.; Standing, K. G. *Int. J. Mass Spectrom. Ion Proc.* **1988**, *85*, 43-67.
- ¹⁴ Kaufmann, R.; Spengler, B.; Lutzenkirchen, F. *Rapid Commun. Mass Spectrom.* **1993**, *7*, 902-910.
- ¹⁵ Spengler, B. *J. Mass Spectrom.* **1997**, *32*, 1019-1036.
- ¹⁶ Cornish, T. J.; Cotter, R. J. *Rapid Commun. Mass Spectrom.* **1993**, *7*, 1037-1040.
- ¹⁷ Cornish, T. J.; Cotter, R. J. *Rapid Commun. Mass Spectrom.* **1994**, *8*, 781-785.
- ¹⁸ Clauser, K. R.; Baker, P.; Burlingame, A. L. *Anal. Chem.* **1999**, *71*, 2871-2882.
- ¹⁹ Colby, S. M.; King, T. B.; Reilly, J. P. *Rapid Commun. Mass Spectrom.* **1994**, *8*, 865-868.
- ²⁰ Dlott, D. D.; Hambir, S.; Franken, J. *J. Phys. Chem. B* **1998**, *102*, 2121-2130.
- ²¹ Poretzky, A. A.; Geohegan, D. B. *Chem. Phys. Lett.* **1998**, *286*, 425-432.
- ²² Yates, J. R. *J. Mass Spectrom.* **1998**, *33*, 1-19.
- ²³ Watson, C. R. M.S. Thesis, Virginia Polytechnic Institute and State University, **1997**.
- ²⁴ Karas, M.; Hillenkamp, F. *Anal. Chem.* **1988**, *60*, 2299-2301.

- ²⁵ Westman, A.; Huthfehre, T.; Demirev, P.; Bielawski, J.; Medina, N.; Sundqvist, B. U. R. *Rapid Commun. Mass Spectrom.* **1994**, *8*, 388-393.
- ²⁶ Beavis, R. C.; Chait, B. T. *Method Enzymol.* **1996**, *270*, 519-551.
- ²⁷ *Current Protocols in Protein Science*; Coligan, J. E., Ed.; Wiley: New York, **2000**.
- ²⁸ Goborn, J.; Schuerenberg, M.; Mueller, M. Theiss, D.; Lehrach, H.; Nordhoff, E. *Anal. Chem.* **2001**, *73*, 434-438.
- ²⁹ Kampmeier, J.; Dreisewerd, K.; Schurenberg, M.; Strupat, K. *Int. J. Mass Spectrom. Ion Proc.* **1997**, *169/170*, 31-41.
- ³⁰ Zenobi, R.; Knochenmuss, R. *Mass Spectrom. Rev.* **1998**, *17*, 337-366.
- ³¹ Horneffer, V.; Dreisewerd, K.; Ludemann, H. C.; Hillenkamp, F.; Lage, M.; Strupat, K. *Int. J. Mass Spectrom.* **1999**, *185-187*, 859-870.
- ³² Karbach, V.; Knochenmuss, R. *Rapid Commun. Mass Spectrom.* **1998**, *12*, 968-974.
- ³³ Dreisewerd, K.; Schurenberg, M.; Karas, M.; Hillenkamp, F. *Int. J. Mass Spectrom. Ion Proc.* **1996**, *154*, 177-178.
- ³⁴ Allwood, D. A.; Dyer, P. E.; Dreyfus, R. W. *Rapid Commun. Mass Spectrom.* **1997**, *11*, 499-503.
- ³⁵ Ehring, H.; Sundqvist, B. U. R. *J. Mass Spectrom.* **1995**, *30*, 1303-1310.
- ³⁶ Knochenmuss, R.; Dubois, F.; Dale, M. J.; Zenobi, R. *Rapid Commun. Mass Spectrom.* **1996**, *10*, 871-877.
- ³⁷ Karas, M.; Bachmann, D.; Bahr, U.; Hillenkamp, F. *Int. J. Mass Spectrom. Ion Proc.* **1987**, *78*, 53-68.
- ³⁸ Ireland, J. F.; Wyatt, P. A. H. *Adv. Phys. Org. Chem.* **1976**, *12*, 131-137.
- ³⁹ Huang, Y.; Russell, D. H. *Int. J. Mass Spectrom. Ion Proc.* **1998**, *175*, 187-204.
- ⁴⁰ Brueker, K.; Knochenmuss, R.; Zenobi, R. *Int. J. Mass Spectrom. Ion Proc.* **1999**, *184*, 25-38.
- ⁴¹ Lehmann, E.; Knochenmuss, R.; Zenobi, R. *Rapid Commun. Mass Spectrom.* **1997**, *11*, 1483-1492.
- ⁴² Liao, P. C.; Allison, J. *J. Mass Spectrom.* **1995**, *30*, 408-423.
- ⁴³ Bokelmann, V.; Spengler, B.; Kaufmann, R. *Eur. Mass Spectrom.* **1995**, *1*, 81-93.

- ⁴⁴ Jorgensen, T. J. D.; Bojesen, G.; Rahbeck-Nielsen, H. *Eur. Mass Spectrom.* **1998**, *4*, 39-45.
- ⁴⁵ Gibson, J. K. *J. Vac. Sci. Technol. A* **1995**, *13*, 1945-1958.
- ⁴⁶ Claisse, F. *Norelco Reporter* **1957**, *4*, 3-7.
- ⁴⁷ Tertian, R.; Claisse, F. *Principles of Quantitative X-Ray Fluorescence Analysis*; Heyden and Sons: London, **1982**; pp 323-333.
- ⁴⁸ Bennett, H.; Oliver, G. J. *Analyst* **1976**, *101*, 803-809.
- ⁴⁹ Analytical Methods for Atomic Absorption Spectrometry, Perkin-Elmer, **1994**.
- ⁵⁰ *Periodic Table of the Elements*,
<http://www.zeuscat.com/andrew/javascript/periodic.html>, last accessed April, 2001.
- ⁵¹ NIST SRM 2709 certificate of analysis, **1993**.
- ⁵² Perkins, W. T.; Fuge, R.; Pearce, N. J. G. *J. Anal. Atom. Spectrom.* **1991**, *6*, 445-449.
- ⁵³ Perkins, W. T.; Pearce, N. J. G.; Jefferies, T. E. *Geochim. Cosmochim. Acta* **1993**, *57*, 475-482.
- ⁵⁴ Kanicky, V.; Mermet, J. M. *Appl. Spectrosc.* **1997**, *51*, 332-336.
- ⁵⁵ Brewer, K. *New Scientist* **1997**, *155*, 36-39.
- ⁵⁶ Arakawa, R.; Matsuo, R.; Ohno, T. *Inorg. Chem.* **1995**, *34*, 2464-2467.
- ⁵⁷ Didier, P.; Jacquet, L.; Kirsch-DeMesmaeker, A.; Huever, R.; van Dorsselaer, A. *Inorg. Chem.* **1992**, *31*, 4803-4809.
- ⁵⁸ Rasmussen, S. C.; Richter, M. M.; Yi, E.; Place, H.; Brewer, K. J. *Inorg. Chem.* **1990**, *29*, 3926-3932.
- ⁵⁹ Balzani, V.; Moggi, L.; Scandola, F. In *Supramolecular Photochemistry*; NATO ASI Series 214; Balzani, V., Ed.; Reidel: Dordrecht, **1987**; p 1.
- ⁶⁰ Balzani, V.; Juris, A.; Venturi, M.; Campagna, S.; Serroni, S. *Chem. Rev.* **1996**, *96*, 759-833.
- ⁶¹ Cerny, R. L.; Sullivan, B. P.; Bursey, M. M.; Meyer, T. J. *Anal. Chem.* **1983**, *55*, 1954-1958.
- ⁶² Callahan, J. H.; Hool, K.; Reynolds, J. D.; Cook, K. D. *Anal. Chem.* **1988**, *60*, 714-719.

- ⁶³ Miller, J.M. *Mass Spectrom. Rev.* **1989**, *9*, 319-347.
- ⁶⁴ Argazzi, R.; Bignozzi, C.A.; Bortolini, O.; Traldi, P. *Inorg. Chem.* **1993**, *32*, 1222-1225.
- ⁶⁵ Colton, R.; Traeger, J. *Inorg. Chim. Acta* **1992**, *201*, 153-155.
- ⁶⁶ Viswanatham, K; Chowdhury, S. K.; Chait, B. T. *J. Am. Chem. Soc.* **1990**, *112*, 5348-5349.
- ⁶⁷ Hopfgartner, G.; Piguet, C.; Henion, J. D.; Williams, A. F. *Helv. Chim. Acta* **1993**, *76*, 1759-1766.
- ⁶⁸ Colton, R. C.; D'Agostino, A.; Traeger, J. C. *Mass Spectrom. Rev.* **1995**, *14*, 79-106.
- ⁶⁹ Moucheron, C.; Mesmaeker, A. K.; Dupont-Gervais, A.; Leize, E.; Van Dorsselaer, A. *J. Am. Chem. Soc.* **1996**, *118*, 12834-12835.
- ⁷⁰ Ishow, E.; Gourdon, A.; Launay, J.; Choirboli, C.; Scandola, F. *Inorg. Chem.* **1999**, *38*, 1504-1510.
- ⁷¹ Bruce, M.; Liddel, M. *Inorg. Chim. Acta* **1992**, *198-200*, 407-413.
- ⁷² Arakawa, R.; Jian, L.; Yoshimura, A.; Nozaki, K.; Ohno, T; Doe, H.; Matsuo, T. *Inorg. Chem.* **1995**, *34*, 3874-3878.
- ⁷³ Verkerk, K.; de Kostor, C.; Markies, B.; Boersma, J.; van Koten, G.; Heerma, W.; Haverkamp, J. *Organometallics* **1995**, *14*, 2081-2090.
- ⁷⁴ Favaro, S.; Pandolfo, L.; Traldi, P. *Rapid Commun. Mass Spectrom.* **1997**, *11*, 1859-1866.
- ⁷⁵ Schubert, U.S.; Eschbaumer, C. *J. Incl. Phenom. Macro.* **1999**, *35*, 101-109.
- ⁷⁶ Bodige, S.; Torres, A. S.; Maloney, D. J.; Tate, T.; Kinsel, G. R.; Walker, A. K.; MacDonnell, F. M. *J. Am. Chem. Soc.* **1997**, *119*, 10364-10369.
- ⁷⁷ Cardona, C. M.; Kaifer, A. E. *J. Am. Chem. Soc.* **1998**, *120*, 4023-4024.
- ⁷⁸ Schalley, C. A. *Int. J. Mass Spectrom.* **2000**, *194*, 11-39.
- ⁷⁹ Dopke, N. C.; Treichel, P. M.; Vestling, M. M. *Inorg. Chem.* **1998**, *37*, 1272-1277.
- ⁸⁰ Jolliffe, K. A.; Calama, M. C.; Fokkens, R.; Nibbering, N. M. M.; Timmerman, P.; Reinhoudt, D. N. *Angew. Chem. Int. Ed.* **1998**, *37*, 1247-1251.
- ⁸¹ Brauns, E.; Jones, S.W.; Clark, J.A.; Molnar, S.M.; Kawanishi, Y.; Brewer, K.J. *Inorg. Chem.* **1997**, *36*, 2861-2867.

- ⁸² Bridgewater, J. S.; Vogler, L. M.; Molnar, S. M.; Brewer, K. J. *Inorg. Chim. Acta* **1993**, *208*, 179-188.
- ⁸³ Lee, J.; Vrana, L. M.; Bullock, E. R.; Brewer, K. J. *Inorg. Chem.* **1998**, *37*, 3575-3580.
- ⁸⁴ <http://www.sisweb.com/cgi-bin/mass10.pl>, last accessed March, 2001.
- ⁸⁵ Newkome, G. N.; Guthrie, R.; Moorefield, C. N.; Cardullo, F.; Echegoyen, L.; Perez-Cordero, E.; Luftmann, H. *Angew. Chem. Int. Ed. Engl.* **1995**, *34*, 2023-2026.
- ⁸⁶ *Laser Chemistry of Organometallics*; Chaiken, J., Ed.; ACS Symposium Series 530; American Chemical Society: Washington, DC, **1993**.
- ⁸⁷ Reid, G. E.; O'Hair, R. A. J.; Styles, M. L.; McFayden, W. D.; Simpson, R. J. *Rapid Commun. Mass Spectrom.* **1998**, *12*, 1701-1708.
- ⁸⁸ van Baar, B. L. M. *FEMS Microbiol. Rev.* **2000**, *24*, 193-219.
- ⁸⁹ *The Ecology of Cyanobacteria: Their Diversity in Time and Space*; Whitton, B. A.; Potts, M., Ed.; Kluwer Academic: Dordrecht, **2000**.
- ⁹⁰ Hunsucker, S. W.; Tissue, B. M.; Potts, M.; Helm, R. F. *Anal. Biochem.* **2001**, *288*, 227-230.
- ⁹¹ Hill, D. R.; Peat, A.; Potts, M. *Protoplasma* **1994**, *182*, 126-148.
- ⁹² Schopf, J. W.; Hayes, J. M.; Walter, M. R. *Earth's Earliest Biosphere*; Schopf, J. W., Ed.; Princeton University: Princeton, **1983**; pp 361-384.
- ⁹³ Margulis, L.; Walker, J. C. G.; Rambler, M. *Nature* **1976**, *264*, 620-624.
- ⁹⁴ Schopf, J. W. *Science* **1993**, *260*, 640-646.
- ⁹⁵ Dodds, W. K.; Gudder, D. A.; Mollenhauer, D. J. *J. Phycol.* **1995**, *31*, 2-18.
- ⁹⁶ Sinha, R. P.; Hader, D. P. *Photochem. Photobiol.* **1996**, *64*, 887-896.
- ⁹⁷ Cameron, R. E. *Trans. Am. Microsc. Soc.* **1962**, *81*, 379-384.
- ⁹⁸ Hill, D. R.; Hladun, S. L.; Scherer, S.; Potts, M. *J. Biol. Chem.* **1994**, *269*, 7726-7734.
- ⁹⁹ Hill, D. R.; Keenan, T. W.; Helm, R. F.; Potts, M.; Crowe, L. M.; Crowe, J. H. *J. Appl. Phycol.* **1997**, *9*, 237-248.
- ¹⁰⁰ Cockell, C. S.; Knowland, J. *Biol. Rev.* **1999**, *74*, 311-345.
- ¹⁰¹ Potts, M., Virginia Polytechnic Institute and State University, personal communication **2000**.

- ¹⁰² Reynolds, C. S.; Oliver, R. L.; Walsby, A. E. *Mar. Freshwater Res.* **1987**, *21*, 379-390.
- ¹⁰³ Bedout, B. M.; Garcia-Pichel, F. *Appl. Environ. Microbiol.* **1995**, *61*, 4215-4222.
- ¹⁰⁴ Lehninger, A. L.; Nelson, D. L.; Cox, M. M. *Principles of Biochemistry*, 2nd Ed.; Worth: New York, **1993**.
- ¹⁰⁵ Sinha, R. P.; Klisch, M.; Groniger, A.; Hader, D. P. *J. Photochem. Photobiol. B Biol.* **1998**, *47*, 83-94.
- ¹⁰⁶ Ehling-Schulz, M.; Scherer, S. *Eur. J. Phycol.* **1999**, *34*, 329-338.
- ¹⁰⁷ Proteau, P. J.; Gerwick, W. H.; Garcia-Pichel, F.; Castenholz, R. *Experimentia* **1993**, *49*, 825-829.
- ¹⁰⁸ Dillon, J. G.; Castenholz, R. W. *J. Phycol.* **1999**, *35*, 673-681.
- ¹⁰⁹ Garcia-Pichel, F.; Castenholz, R. W. *J. Phycol.* **1991**, *27*, 395-409.
- ¹¹⁰ Gygi, S. P.; Aebersold, R. *Curr. Opin. Chem. Biol.* **2000**, *4*, 489-494.
- ¹¹¹ Yates, J. R. D.; Aepicher, S.; Griffin, P. R.; Hunkapiller, T. *Anal. Biochem.* **1993**, *214*, 397-408.
- ¹¹² Mann, M.; Hojrup, P.; Roepstorff, P. *Biol. Mass Spectrom.* **1993**, *22*, 338-345.
- ¹¹³ *Swiss-Prot + TrEMBL Home Page*, <http://www.ebi.ac.uk/swissprot/>, last accessed April, 2001.
- ¹¹⁴ Kinter, M.; Sherman, N. E. *Protein Sequencing and Identification Using Tandem Mass Spectrometry*; Wiley: New York, **2000**; pp 207-237.
- ¹¹⁵ *PeptIdent*, <http://expasy.cbr.nrc.ca/tools/peptident.html>, last accessed April, 2001.
- ¹¹⁶ *ProteinProspector v. 3.4.1*, <http://prospector.ucsf.edu/>, last accessed April, 2001.
- ¹¹⁷ Peltier, J. B.; Friso, G.; Kalume, D. E.; Roepstorff, P.; Nilsson, F.; Adamska, I.; van Wijk, K. J. *Plant Cell* **2000**, *12*, 319-341.
- ¹¹⁸ Kinter, M.; Sherman, N. E. *Protein Sequencing and Identification Using Tandem Mass Spectrometry*; Wiley: New York, **2000**; pp 64-115.
- ¹¹⁹ Eng, J. K.; McCormack, A. L.; Yates, J. R. *J. Am. Soc. Mass Spectrom.*, **1994**, *5*, 976-989.
- ¹²⁰ *ExPASy Molecular Biology Server*, <http://expasy.ch>, last accessed April, 2001.

- ¹²¹ Huneke, F., Virginia Polytechnic Institute and State University, unpublished results.
- ¹²² Garcia-Pichel, F. Castenholz, R. W. *J. Phycol.* **1991**, *27*, 395-409.
- ¹²³ *Nostoc Punctiforme*, http://spider.jgi-psf.org/JGI_microbial/html/nostoc_homepage.html, last accessed April, 2000.
- ¹²⁴ Belenky, M.; Wang, B.; Belenky, A.; Herzfeld, J. *Anal. Biochem.* **2000**, *280*, 182-185.
- ¹²⁵ Chillier, X. F. D.; Van Berkel, G. J.; Gulacar, F. O.; Buchs, A. *Org. Mass Spectrom.* **1994**, *29*, 672-678.
- ¹²⁶ Perkins, J. R.; Smith, B.; Gallagher, R. T.; Jones, D. S.; Davis, S. C.; Hoffman, A. D.; Tomer, K. B. *J. Am. Soc. Mass Spectrom.* **1993**, *4*, 670-684.
- ¹²⁷ Amado, F. M. L.; Domingues, P. Santana-Marques, M. G.; Ferrer-Correia, A. J.; Tomer, K. B. *Rapid Commun. Mass Spectrom.* **1997**, *11*, 1347-1352.
- ¹²⁸ Helm, R. F., Virginia Polytechnic Institute and State University, personal communication **2000**.
- ¹²⁹ Edwards, H. G. M.; Garcia-Pichel, F.; Newton, E. M.; Wynn-Williams, D. D. *Spectrochim. Acta A Mol. Biomol. Spectrom.* **2000**, *56*, 193-200.

Vita

Stephen Warren Hunsucker was born on November 25, 1971 to Phillip and Beverly Hunsucker in Highpoint, North Carolina. He attended North Allegheny High School in Pittsburgh, Pennsylvania and graduated in the spring of 1990.

After high school Steve enrolled at Fort Lewis College in Durango, Colorado in order to study chemistry. He met his future wife Julie Jensen while living in Durango. After taking a year off to clear his head and make some money he received a B.S. in Chemistry in May of 1996. Steve and Julie were married on July 13, 1996.

Steve was accepted to graduate school at Virginia Polytechnic Institute and State University and began his study in January of 1997. During graduate school he received an award for outstanding graduate research from the Chemistry Department at Virginia Tech. In April of 2001 he and his wife discovered she was pregnant and were to have a new baby in December of that same year. He received his Ph.D. in Chemistry in May of 2001. He accepted a postdoctoral position in the Biochemistry Department at Virginia Tech and will work with Dr. Rich Helm.